Anne Geese

Earth's Magnetic Field:
Observation and Modelling
From Global to Regional Scales

Scientific Technical Report STR11/03

Anne Geese

Earth's Magnetic Field: Observation and Modelling From Global to Regional Scales

Scientific Technical Report STR11/03

Earth's Magnetic Field: Observation and Modelling From Global to Regional Scales

Von der Fakultät für Elektrotechnik, Informationstechnik, Physik
der Technischen Universität Carolo-Wilhelmina
zu Braunschweig
zur Erlangung des Grades einer
Doktorin der Naturwissenschaften
(Dr. rer. nat.)
genehmigte Dissertation

von Anne Geese, geborene Hemshorn
aus Hamm in Westfalen

1   2

Prof. Dr. Karl-Heinz Glaßmeier   Prof. Dr. Mioara Mandea
Institut für Geophysik   Institut de Physique du Globe de Paris
und extraterrestrische Physik   Géophysique spatiale et planétaire
Technische Universität Carolo-Wilhelmina   Université Paris Diderot
zu Braunschweig

eingereicht am: 09. September 2010

mïndliche Prüfung am: 19. November 2010

Vorabveröffentlichung der Dissertation

Teilergebnisse aus dieser Arbeit wurden mit Genehmigung der Fakultät für Elektrotechnik, Informationstechnik, Physik, vertreten durch den Mentor der Arbeit, in folgenden Beiträgen vorab veröffentlicht:

Publikationen:

Geese, A., Mandea, M., Lesur, V., and Hayn, M. (2010). Regional modelling of the southern african geomagnetic field using harmonic splines. *Geophysical Journal International*, 181(3):1329–1342.

Korte, M., Mandea, M., Linthe, H.-J., Hemshorn, A., Kotzé, P., Ricaldi, E. (2009): New geomagnetic field observations in the South Atlantic Anomaly region, *Annals of Geophysics*, 52: 65-81.

Hemshorn, A., Auster, H.U.,Fredow. M. (2009). TECHNICAL DESIGN NOTE: DI-Flux measurement of the geomagnetic field using a three-axial fluxgate sensor.*Measurement Science and Technology*, 20(2), 027004-027007

Hemshorn, A., Pulz, E., Mandea, M. (2009): GAUSS: Improvements to the Geomagnetic AUtomated SyStem, *Proceedings of the XIIIth IAGA Workshop on Geomagnetic Observatory Instruments, Data Acquisition, and Processing*, Open-File Report 2009-1226, 100-103

Hemshorn, A., Auster, U., Fredow, M. (2009): DI3: Improving DI-Flux measurements with the Three-Component Sensor, *Proceedings of the XIIIth IAGA Workshop on Geomagnetic Observatory Instruments, Data Acquisition, and Processing*, Open-File Report 2009-1226, 104-107

Auster, H. U., Mandea, M., Hemshorn, A., Pulz, E., Korte, M. (2007): Automation of absolute measurements of the geomagnetic field, *Earth, Planets and Space*, 59, 9, 1007-1014.

Tagungsbeiträge:

Geese, A., Mandea, M., Lesur, V. (2010). SAMS - the South African Magnetic model made of Splines, 28th IUGG Conference on Mathematical Geophysics - CMG 2010, June 7-11 2010, Pisa, Italy

Geese, A., Lesur, V., Wardinski, I., Mandea, M. (2010). SV estimates from monthly means visa predictions from global field models, European Geophysical Union, General Assembly, May 4-9, 2010, Vienna, Austria

Geese, A., Mandea, M., Lesur, V. (2009). Regional Modeling of the Southern African Secular Variation, 11th IAGA Scientific Assembly, August 23-30, 2009, Sopron, Hungary

Hemshorn, A., Pulz, E., Mandea, M., Korte, M., Auster, U. (2008). GAUSS - Improvements to the Geomagnetic AUtomated SyStem, XIIIth IAGA Geomagnetic Observatory Workshop, June 9-18, 2008, Boulder and Golden, CO, USA

Hemshorn, A., Auster, U., Fredow, M. (2008). DI3 - First tests of DI-Flux measurements with a three-axial fluxgate sensor, XIIIth IAGA Geomagnetic Observatory Workshop, June 9-18, 2008, Boulder and Golden, CO, USA

Contents

Summary

The magnetic field of the Earth varies in space and time. Geomagnetism as research area that aims to describe and understand the sources of these variations is supported by two pillars: first, regular high-precision measurements in the global network of magnetic observatories and repeat stations are necessary to register the field and its variations at all. Second, mathematical methods are required in order to extract magnetic field models from this large data set. Methods applied to data offer insights in the mechanisms generating the magnetic field.

This thesis covers both subjects. In a first part, following the description of the state of the art in observatory instrumentation, I explain in detail two instruments that have the potential to streamline the classical procedures: The *Geomagnetic AUtomated SyStem* GAUSS paves the way to automated absolute measurements, up to now only possible manually. The newly developed *DI3* technique improves and simplifies the standard manual measurements significantly and thus reduces the requirements placed on observers.

The second part deals with the mathematical tools available for geomagnetic field modelling. I focus on harmonic splines that can be derived from the classical approach of spherical harmonics. These base functions are interpolatory and have a localised shape while satisfying Laplaces equation. Hence, they are applicable to fit data regionally or globally.

The harmonic splines are used with a data set made of repeat station and observatory measurements from Southern Africa. This region is of special interest because the field intensity is very low and and both spatial and temporal field gradients exist. Subdivided into an analysis of ancient (years 1961-2001) and recent (2005-2009) data, two continuous regional field models *SAMS* and *X-SAMS* are derived. From the analysis of the field models, a better understanding of the field behaviour is gained.

Finally, the harmonic splines are used in a case study on globally distributed secular variation data. Rotating the data set in a system of coordinates aligned with the dipole axis and modelling it with the harmonic splines reveals the external origin of observed fast variations.

Zusammenfassung

Das Magnetfeld der Erde ändert sich in Raum und Zeit. Die Ursachen dieser Änderungen zu beschreiben und zu verstehen ist das Ziel der geomagnetischen Forschung. Sie ruht auf zwei Säulen: Erstens werden regelmäßig hochpräzise Messungen in einem Netz von Observatorien und Säkularpunkten durchgeführt, um das Feld mit seinen Variationen überhaupt aufzuzeichnen. Zweitens sind mathematische Methoden notwendig, um aus dieser Fülle von Daten magnetische Feldmodelle abzuleiten. Werden die Methoden auf die Daten angewandt, kann man Erkenntnisse gewinnen, wie die Felder erzeugt und Variationen hervorgerufen werden.

In dieser Arbeit werden beide Herangehensweisen beschrieben. Im ersten Teil stelle ich zwei Instrumente vor, mit deren Hilfe die klassischen Messprozeduren in geomagnetischen Observatorien überholt werden können. Das *Geomagnetic AUtomated SyStem* GAUSS ebnet den Weg für automatisierte Absolutmessungen, die bisher nur händisch möglich sind. Die neu entwickelte *DI3* Technologie verbessert und vereinfacht die manuelle Standardmethode und setzt somit die Anforderungen, die an Observatoren gestellt werden, herab.

Der zweite Teil behandelt die mathematischen Methoden, die für geomagnetische Modellierung zur Verfügung stehen. Insbesondere hebe ich harmonische Splinefunktionen hervor, die sich aus dem klassischen Ansatz der spärisch-harmonischen Analyse ableiten lassen. Diese Basisfunktion haben interpolierenden Charakter und eine lokalisierte Form, wobei sie gleichzeitig die Laplacebedingung erfüllen. Sie können sowohl für regionale als auch für globale Modellierungen eingesetzt werden.

Im Anschluss werden die harmonischen Splines auf einen Datensatz angewendet, der aus Messungen in Observatorien und an Säkularpunkten im südlichen Afrika besteht. Diese Region ist geomagnetisch besonders interessant, da die Feldstärke hier verhältnismäßg klein ist und starke räumliche und zeitliche Änderungen beobachtet werden. Die Analyse wird unterteilt in eine Untersuchung älterer und neuerer Daten, aus denen ich die beiden kontinuierlichen Feldmodelle *SAMS* und *X-SAMS* ableite. Aus der näheren Untersuchung der Modelle gewinne ich ein besseres Verständnis des geomagnetischen Verhaltens dieser Region.

Zum Schluss werden die harmonischen Splines in einem Fallbeispiel benutzt, um Schwankungen in global verteilten Säkularvariationsdaten genauer zu beschreiben. Die Drehung in ein geomagnetisches Koordinatensystem und die Modellierung mit Splinefunktionen deckt auf, dass beobachtete schnelle Variationen durch externe Einflüsse her-

vorgerufen werden.

Chapter 1

Introduction

1.1   A short review of the history of geomagnetism

The geomagnetic field of the Earth is one of the oldest subjects of scientific research. Although it is under discussion at what exact time and on which continent compasses were used first, it can be assumed that Asian, European and Arabic mariners benefited from the magnetic influence on magnetised needles orienting themselves always more or less in a north-south direction. These compasses can be considered as the earliest magnetic field instruments.

The first extant scientific report describing the Earth's magnetic field goes back to Peter Peregrinus of Maricourt, who studied the behaviour of magnetised rocks in the thirteenth century. Even though he incorrectly attributed the Earth's magnetism to the action of *celestial* poles, he could already distinguish the two different poles of a magnetic needle. His *Epistola de magnete* dated by the year 1269 comprises the description of observed phenomena of attraction and repulsion and the sketches of different compasses. This letter is accepted to be the very first scientific publication on Geomagnetism. Three centuries later, William Gilbert, physicist and royal personal physician of Queen Elizabeth I., experimented with a magnetised sphere which he called *terrella*, little Earth. From his systematic experiments he concluded properly that the Earth itself generates the forces that orient compasses. Gilbert published his results in 1600 in his book *De Magnete, Magneticisque Corporibus, et de Magno Magnete Tellure*, a book with great success in Europe as reflected by the big number of copies compiled in the following years.

Almost two centuries later, on April 30, 1777, Carl Friedrich Gauß was born in Braunschweig. His merits for Geomagnetism can hardly be overestimated. Thanks to his developments in instrumentation, it was possible for the first time to measure the field absolute intensity (Gauss, 1833). Together with Alexander von Humboldt, he established the first globally synchronised measurements and founded the *Göttinger Magnetischer Verein* (Göttingen magnetic club) devoted to coordinate the efforts of the existing observatories. But besides his practical achievements, Gauss moreover worked out the mathematical theory for separating the inner and outer sources of Earth's magnetic field by the use of
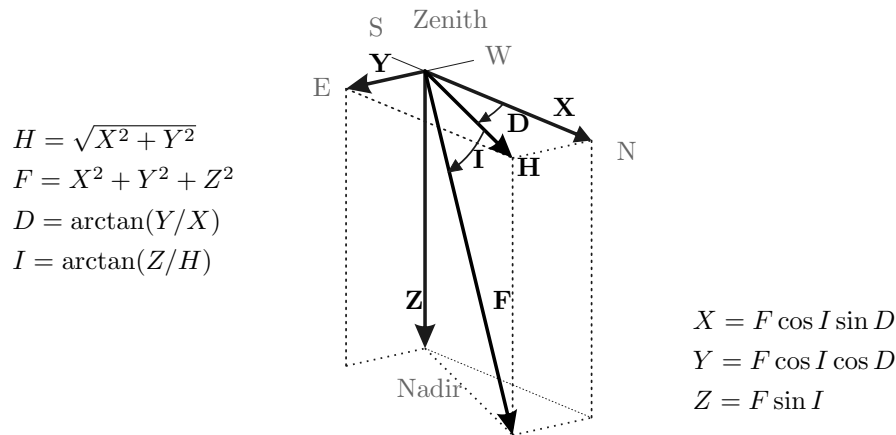
1

$$H = \sqrt{X^2 + Y^2}$$
$$F = X^2 + Y^2 + Z^2$$
$$D = \arctan(Y/X)$$
$$I = \arctan(Z/H)$$

$$X = F \cos I \sin D$$
$$Y = F \cos I \cos D$$
$$Z = F \sin I$$

Figure 1.1: The magnetic field elements and their relation between each other.

spherical harmonic expansion (Gauss, 1839). This method has been the standard tool for analysing the geomagnetic field until today.

A few years later, the basic equations of electromagnetism were compiled by James Clerk Maxwell allowing for a comprehensive study of the field. Until the midst of the 20th century, a correct description of the Earth's magnetic field had mostly been limited by the sparse data distribution. The International Geophysical Year (IGY) spanning the period July 1957 to December 1958 and even more the subsequent World Magnetic Survey (WMS, Heppner, 1963) initiated the installation of new observatories, urged the launch of satellites for magnetic prospection and hence gave fresh impetus to field modelling and interpretation.

At this time, the improved field description was due to the refinements in instrumentation both on Earth and in space. The invention of the vectorial fluxgate and the scalar Proton magnetometer allowed for easy-to-handle, accurate measurements. Enhanced computer capability permitted the processing of the constantly growing quantity of available data in the following years. The launch of the Ørstedt satellite in 1999 inaugurated the decade of the geopotential fields and provided an unprecedented amount of high-quality data, extended by the CHAMP mission until today. The derivation of the recent field models from those satellite data is nowadays only possible thanks to sophisticated digital data processing.

1.2   Geomagnetic elements

According to the correct scientific magnetic definition, the field intensity is abbreviated with **H** and **B** describes the magnetic flux density or magnetic field. In free space without any magnetisation, the two are related by

$$\mathbf{B} = \mu_0 \mathbf{H}$$

where $\mu_0 = 4 \cdot 10^{-7} \text{VsA}^{-1}\text{m}^{-1}$ is the vacuum permeability. As it is common in Geophysics, we will only deal with and analyse the magnetic field **B**. This also prevents confusion
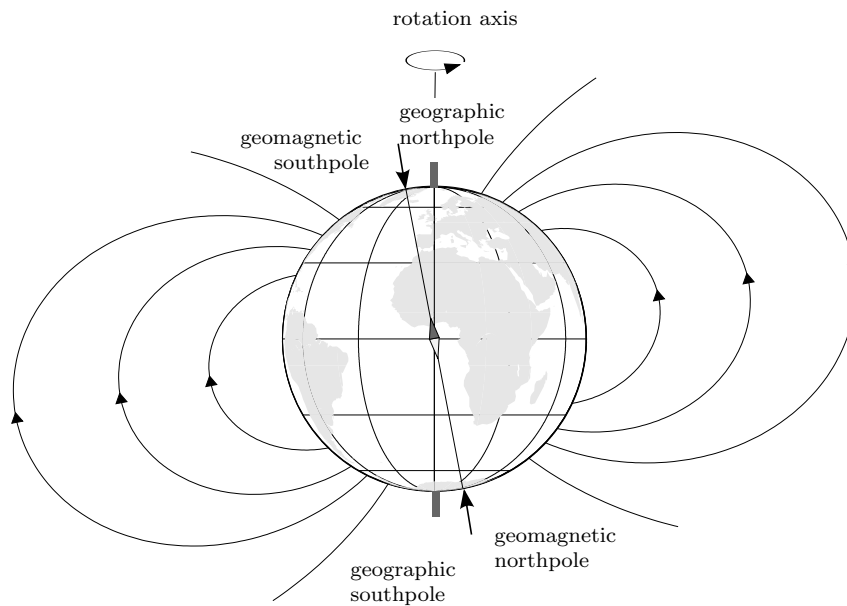
Figure 1.2: The field lines of a geocentric dipole. The dipole axis is tilted about 11° with respect to the rotation axis.

with the horizontal field intensity H.

The elements of the geomagnetic field can be described differently. In a spherical coordinate system where r is the radial distance, ϑ the colatitude and φ the longitude, the three components of the magnetic field are $(B_r, B_\vartheta, B_\varphi)$. From the historical point of view, the field declination and inclination were mapped first. The declination D is the angle between geographic (or "true") North and the horizontal component (H) of the magnetic field, the inclination I describes the angle between the horizontal plane and a vector pointing along the total intensity F. X and Y are defined as geographic North and East component. The triples DIF and DHZ are close to the standard measurement procedure, while XYZ forms an easy to handle Cartesian trihedron and differs only by sign from the tuple $(B_r, B_\vartheta, B_\varphi)$. All bases can be converted using simple geometry (cf. Fig. 1.1).

The SI unit of magnetic fields is T (Tesla) which finds its accordance in the CGS unit Gs (Gauss) that is still widely used in astrophysical context. In Geomagnetism, field intensities are usually given in nT identical with the historical unit γ.

$$1\text{nT} = 10^{-9}\text{T} = 10^{-5}\text{Gs} = 1\gamma = 10^{-9}\text{kgA}^{-1}\text{s}^{-2}$$

In Germany, the current values are roughly about $X = 20.000\,\text{nT}$ and $Z = 45.000\,\text{nT}$. The Y component amounts to only some few hundreds of nT yielding a declination between zero and three degrees.

Figure 1.3: The total field intensity at the Earth's surface as predicted by the IGRF-11 model for 2009.0. The reduced intensity over the South Atlantic (SAA) is the most remarkable non-dipolar feature.

1.3   Geomagnetic field sources and variations

The core field

The largest contribution of the geomagnetic field is called the *Main Field* (MF) or *Core Field*. It is driven by a dynamo process inside the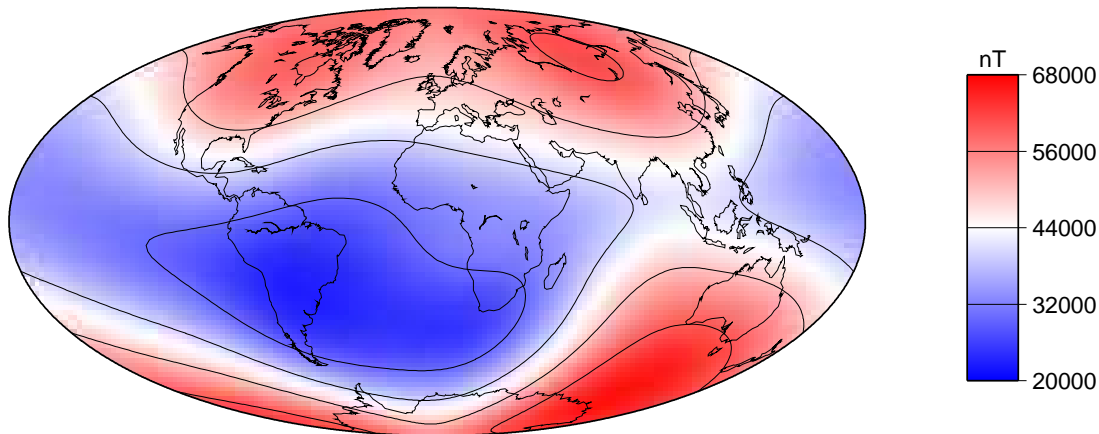 Earth's molten outer core. The conducting iron convects from the inner core up to the *Core Mantle Boundary* (CMB) and is deviated due to the Earth's rotation by Coriolis forces.

The main field features a dominant dipolar structure tilted by about 11° from the Earth's rotation axis as shown in Fig. 1.2. Hence, the horizontal component points mainly in north-south direction and allows compasses to orient. At the poles, the field intensity amounts presently to 60000 nT at the poles and decreases to its half at the equator. This dipole field can be attributed to a dipole moment of $7.746 \cdot 10^{24}$ nTm^3 which has been, however, decreasing since the last centuries. In fact, a multipole expansion is necessary to describe the details of the main field. In Fig. 1.3 the non-dipolar structure becomes clear e.g. by the diminished field intensity over the Southern Atlantic, a feature known as the *South Atlantic Anomaly* (SAA). The anomaly provokes problems for satellites crossing this area: the diminished intensity shields incoming solar radiation less effectively and this induces instrument failures. But that is only a side effect of the prominent field diminishment. Studies of combined inversion of the magnetic flux have shown that the area features an inverse flux patch at the core mantle boundary (see e.g. Wardinski and Holme, 2006).

Long-term changes of the geomagnetic field originating in the core are called *secular variation* (SV) as a first time derivative. During the last years, much attention has been drawn to abrupt changes detectable in the SV. Especially the last centuries time series of the second derivative of the East component shows jumps. Those *geomagnetic jerks* as they are usually called (see e.g. Courtillot and Le Mouël, 1984) happen to appear globally. Since Alexandrescu et al. (1995) detected jerks by wavelet analysis, several of
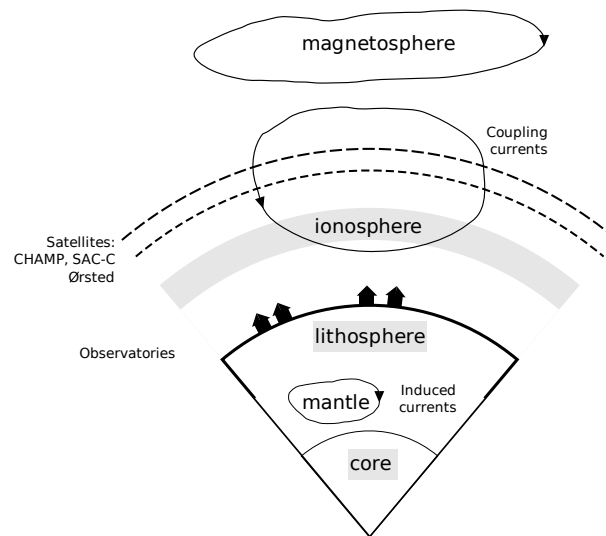
Figure 1.4: The main sources of the geomagnetic field (magnetosphere, ionosphere, lithosphere and core) and the platforms (satellites and observatories) to observe them, following Sabaka et al. (2004).

these events are broadly accepted. Prominent examples are the jerks in 1969 and 1978 (see e.g. Courtillot and Le Mouël, 1988, Lühr et al., 2009, for more details).

The crust

The outer core is surrounded by the Earth's solid mantle, where temperatures range between several 100°C at the upper boundary and about 3500°C at the CMB which is above the Curie temperature of the mantle material. Hence, no remanent magnetism can persist in these depths. The outer layer of the Earth, the *crust*, is rather cool. It has a thickness of $5 - 10\,$km below the oceans and $30 - 50\,$km underneath the continents and temperatures allowing magnetic field to remain in the material. The crustal field has mostly small spatial wavelengths but can reach anomalies of several thousand nT. Prominent examples are the Bangui anomaly in central Africa, the Beattie anomaly in South Africa or the Kursk anomaly in Russia where the enhancement is due to a large iron ore. A very detailed view of the crustal magnetic field is given by Korhonen et al. (2007) who compiled the *World Digital Magnetic Anomaly Map* from different aeromagnetic, marine and satellite data sets. It is specified as a global 3-arc-minute resolution grid of the anomaly of the magnetic intensity at an altitude of 5 km above mean sea level.

The external contributions

Flowing above the Earth's surface, electric currents generate variations on shorter time scales. The uppermost part of the Earth's atmosphere is called the ionosphere. Stretching

Variation		Period	Amplitude	Source
Solar cycle dependent		≈ 11 years	20 nT	Variations of the ERC caused by solar activity
Annual variations		1 year	5 nT	Ionospheric sources
Semiannual variations		6 months	5 nT	Variations of the ERC with the rotation of the Earth around the sun
Magnetic storm	D_{ST}	2-27 days	100 nT	Enhancement of ERC caused by enhanced solar particle flux
Solar quiet	S_q	1 day	30-100 nT	Ionospheric current systems on the day-side of the Earth
Storm commencement	ssc	2-5 min	10 - 100 nT	solar particle flux penetrating the magnetosphere
Regular Pulsations	pc	0.2-600 s	0.1-100 nT	Magnetohydrodynamic waves
Irregular Pulsations	pi	1-100 s	1 nT	in the magnetosphere

Figure 1.5: Variations of the Earth's magnetic field from external origin, listed with associated abbreviation or index, period, and mean intensity (following Schmucker, 1985).

from 80 km to about 1000 km, this shell features a high density of charged particles, both ions and electrons. Hence, it is an electric conductor that interacts with the geomagnetic field. Driven by solar irradiation, the ion density changes dependent on the local time and ionospheric currents are generated. A prominent example is the equatorial electrojet (EEJ) effecting a daily magnetic field variation, the so-called S_q (solar quiet) variation. In a greater distance from the Earth, magnetospheric currents are driven by the interaction between the solar wind carrying charged particles and its own magnetic field with the geomagnetic field. The equatorial electrojet flowing at the day-side and magnetospheric tail currents on the night side generate the main contributions. Dependent on the distinct - quiet or disturbed - solar wind conditions, the magnetosphere can be affected remarkably and may cause magnetic storms or substorms. On the surface of the Earth, this external signal is also seen in induction effects.

The influences of external sources to the geomagnetic field measured on the surface of the Earth are manifold. Periods range from subseconds to years and produce perturbations between fractions of a nT to several hundreds of nT. Table 1.5 gives an overview of some of the most important variations. For more details, the reader is referred to the very extensive *Encyclopedia of Geomagnetism and Paleomagnetism* edited by Gubbins and Herrero-Bervera (2007), more information especially about field variations can be found e.g. in Courtillot and Le Mouël (1988), Jankowski and Sucksdorf (1996) or Glaßmeier et al. (2009)
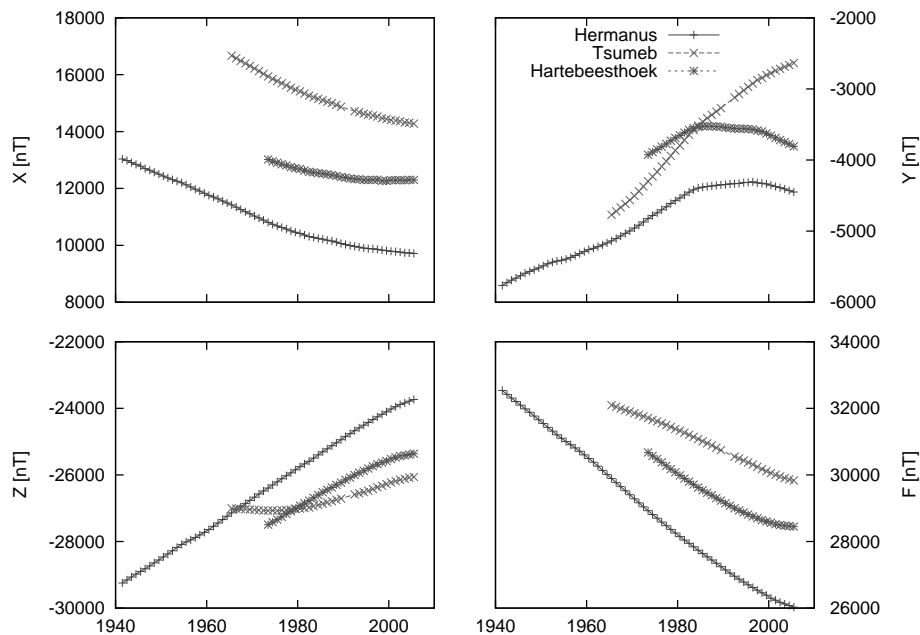
Figure 1.6: Annual mean values of the three observatories Hermanus, Tsumeb and Hartebeesthoek accounted in this study.

1.4   Open issues

Not only the example of Gauss shows that geomagnetic insights can only be gained through both instrumental developments and mathematical approaches. In both fields, the geomagnetism still demands improvements. Therefore, this thesis leans on two pillars: instrumentation and modelling. Nowadays, measurements at satellite altitude cover the Earth globally. At the Earth's surface, magnetic observatories are responsible to provide highly accurate measurements, but they lack in remote regions where no regular, reliable manpower is available. In chapter 2 of this thesis, I show two ways how the situation can be improved. First, I present GAUSS, an instrument that carries out observatory tasks automatically. Additionally, I introduce the DI3 technique that helps to enhance the data quality in manned remote geomagnetic observatories.

As to the data analysis, the spherical harmonic expansion was the state of the art in global modelling for the last 170 years and will presumably prevail it in the future. For regional modelling, no standard technique has become generally accepted and used. In chapter 3, I resume the harmonic spline approach which can be derived from spherical harmonics. The main features of these functions are their interpolatory and localized characteristics. Hence, they are perfectly suitable for a regional modelling approach. The method is applied to an area where geomagnetically interesting trends can be observed: The southern African region. Not only that the total field has decreased by more than 20% since the beginning of the last century, the field components show as well large spatial gradients (cf. Fig. 1.6). After an intensive study of the repeat station and observatory

data available in this region, I provide regional field models based on harmonic splines for the time period from 1960 to 2001 and from 2005 to 2010 in chapter 4. Those models are suitable to study the field behaviour in much more detail. Moreover, I make use of the special features of the harmonic splines by investigating the global behaviour of the secular variation in chapter 5. Recent global models seem to fail the fit to SV estimates globally. With the help of the spline functions I show that not the main field models struggle, but that monthly means are contaminated with external influences more than presumed.The sixth chapter summarises all results achieved and provides some prospects.

Chapter 2

From surface to space: magnetic field observation

Geomagnetic measurements are performed in many ways and at various platforms. *Geomagnetic observatories* provide highest quality data, however at a low and unequal spatial resolution. To increase the spatial density regionally, *repeat station* surveys are conducted in many nations. Finally, *satellites* offer a uniform, global coverage but face problems of attitude control and ambient current densities.

All these kind of magnetic measurements are subsequently used for modelling. This chapter gives an overview of their instrumentation, data output, data quality and their distribution. Additionally, I explain in detail how the instrument **GAUSS** paves the way to automated absolute measurements in geomagnetic observatories and how the standard manual measurements can be improved by the newly developed **DI3** technique.

2.1 Geomagnetic observatories

Geomagnetic observatories exist in many countries and provide the best quality data. Their distribution is very unequal: while Europe and most of the northern hemisphere show a very dense repartition, the southern hemisphere and the oceans feature a lot of gaps (cf. Fig. 2.1). Due to the coverage by vaste oceans, relatively little area remains on the southern globe for setting up ground based observatories. Furthermore, less funding organisations exist in the developing countries that could support the maintenance of geomagnetic observatories.

Nowadays, about 170 facilities are run world-wide whereof 111 join the *International Real-time Magnetic Observatory Network* INTERMAGNET. The INTERMAGNET programme exists to establish a global network of cooperating digital magnetic observatories. The program gives recommendations and defines standard specifications for measuring and recording equipment in order to facilitate data exchange and the preparation of geomagnetic products. This affects mainly the way how the geomagnetic field is observed. Intermagnet also collects and provides data sets and yearbooks of the par-
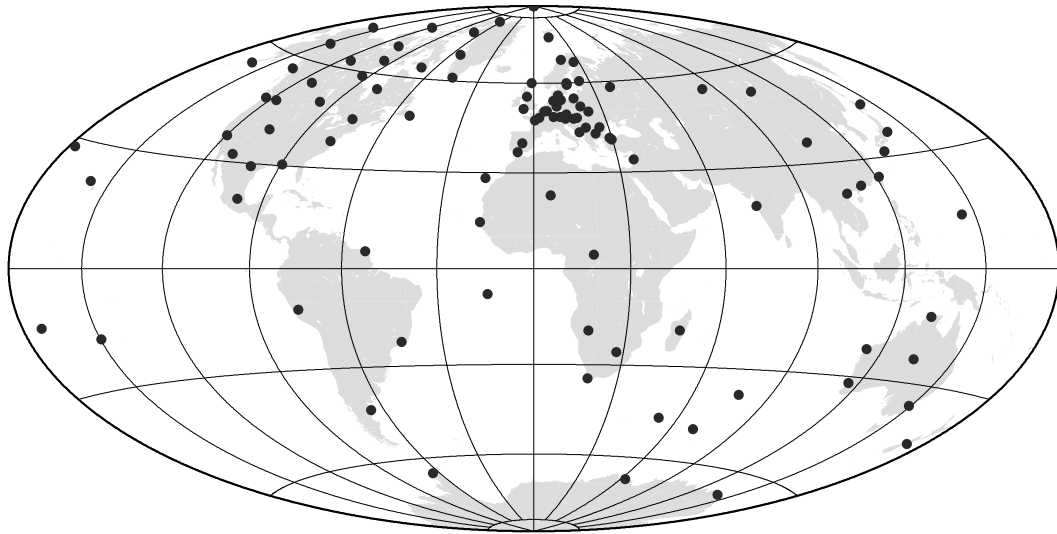
Figure 2.1: Global distribution of INTERMAGNET magnetic observatories.

ticipating observatories. As described in the previous chapter, the field can be separated into two contributions: a slowly changing, large part, the main field, and a rapidly vary-ing, small portion, the external field, which mostly amounts to 1%, seldom up to 10% of the main field. Hence, the instrumentation of geomagnetic observatories is also twofold: extensive effort is paid to determine correctly the *absolute measure* of the Earth's field whereas its changes are recorded with relative instruments, the so-called *variometers*. This subdivision is also reflected in the common layout of geomagnetic observatories that offers separate buildings or huts for variation recordings and absolute measurements.

Several geomagnetic instruments, whether absolute and relative ones, scalar and vectorial ones, automatic or manually operated ones, that were in use in the past or have provided measurements until today, are be summarised in the following sections.

2.1.1   Standard instruments

I start with an overview of different observatory instruments that are or have been broadly in use.

A Directional variometer: The Fluxgate Magnetometer

The fluxgate is nowadays the most common observatory instrument for directional vari-ation recordings. It was developed following the work of Aschenbrenner and Goubau (1936). Roughly spoken, the fluxgate is comparable to a simple transformer, where an easily saturable core made of highly permeable material is surrounded by both a primary (or exciting) and a secondary (or pick-up) coil. An alternating excitation current fed into the primary winding with frequency f ($\omega = 2\pi f$) drives the core into saturation. If there is an external field H_0 along the core axis, the signal in the pick-up coil does not only
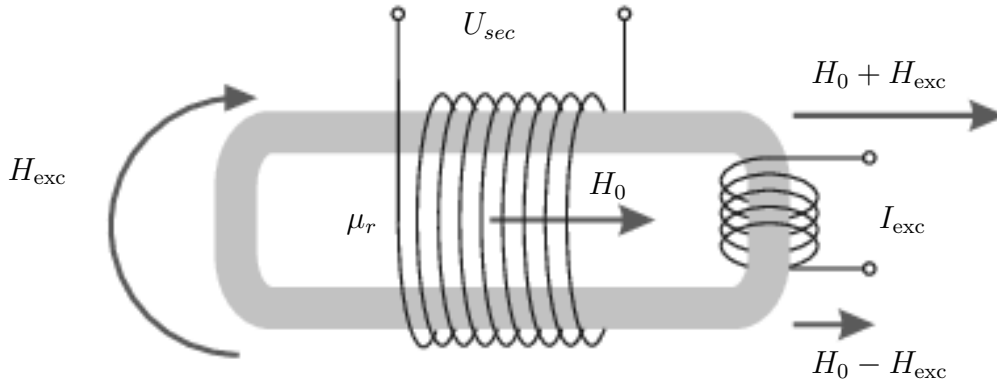
Figure 2.2: Schematic design of a fluxgate magnetometer. For explanation of H_0, H_{exc},I_{exc}, U_{sec} see text.

contain the exciting frequency f, but also higher harmonics, in which the second harmonic is particularly sensitive to H_0.

We follow Aschenbrenner and Goubau (1936) to show the main, very simplified relations. We consider a ring core as shown in Fig. 2.2 with a hysteresis curve that can be approximated by a third order polynomial

$$B = aH^3 + cH \tag{2.1}$$

If an harmonic excitation field of the form $H_{\text{exc}} = H_e \sin \omega t$ with amplitude H_e and frequency ω is applied, the above equation takes the form:

$$H = H_0 \pm H_e \sin \omega t \ ,$$

where the upper sign applies for the upper bar and the lower sign for the lower bar of the ring. Inserted into equation 2.1 and exploiting trigonometric identities, we obtain

$$
\begin{aligned}
B = \quad & a\left(H_0 \pm H_e \sin \omega t\right) - c(H_0 - H_e \sin \omega t)^3 \\
= \quad & aH_0 - cH_0^3 - \frac{3}{2}cH_e^2 H_0 \\
& \pm(aH_e - 3cH_e H_0^2 - \frac{3}{4}cH_e^2)\sin \omega t \\
& + \frac{3}{2}cH_e^2 H_0 \cos 2\omega t \pm \frac{1}{4}cH_e^3 \sin 3\omega t \ .
\end{aligned}
\tag{2.2}
$$

The magnetic flux Φ through the secondary coil is the sum of fluxes through both bars. With a cross section area A, the flux adds up to

$$
\begin{aligned}
\Phi &= 2AB \\
&= 2A\left[(aH_0 - cH_0^3 - \frac{3}{2}cH_e^2 H_0) + \frac{3}{2}cH_e \cos 2\omega t\right] \ .
\end{aligned}
\tag{2.3}
$$

Except for the second harmonic, all time dependent contributions cancel out and the amplitude of the remaining term $\cos \omega t$ is directly proportional to the external field H_0.

Of course, the situation is more complex in reality because Eq. (2.1) is oversimplified, but the measurement principle works well and fluxgate magnetometers are used in many different applications from geophysics and space science to biology and medical technology. More detailed descriptions can be found in Wiese et al. (1960), Primdahl (1979), Forbes (1987) or, more recently and considering mostly space fluxgate magnetometers, in Acuña (2002). The design of the first digital instrument is explained in Auster et al. (1995).

Using three orthogonal coil pairs, all components of a magnetic field can be measured with high accuracy. However, fluxgate magnetometers are subject to different error sources. Each of the three directions can show an offset. Additionally, deviations from the nominal scale value and from the orthogonality between the coils' directions can exist, so that altogether nine parameters are necessary to calibrate a three-component fluxgate magnetometer completely. Techniques of determining a fluxgate calibration parameters are given in detail by Auster (2000) and are explained in the next section.

The accuracy of a fluxgate magnetometer, limited by the noise of the core material, decreases with increasing frequency. The maximal temporal resolution is restricted by the necessary distance to the excitation frequency. Thus, excitation frequencies between $1\,\mathrm{kHz}$ to $128\,\mathrm{kHz}$ have a noise of $10\,\mathrm{pT}/\sqrt{\mathrm{Hz}}$ at a sample frequency of $1\,\mathrm{Hz}$; the highest sample rates are about $128\,\mathrm{Hz}$.

The main feature of a fluxgate magnetometer is its high sampling rate which was already the main motivation for the work of Aschenbrenner and Goubau and which makes them suitable as variometers until today. But, although a fluxgate can be set up towards a known geographic reference frame, it will not keep this position during the time span of a working observatory. The pillar where the variometer is placed can be subject to drifts, following for example the local temperature changes. Also the fluxgate calibration parameters can easily be influenced by such external conditions. Hence, an absolute reference as described below is vital.

A semi-absolute instrument: The Quartz Horizontal Magnetometer

The Quartz Horizontal Magnetometer (QHM) was the main **semi-absolute** instrument for determining the **horizontal component** until the early 1980's, and is still in use in some geomagnetic observatories.

A small horizontal magnet and a plane mirror perpendicular to its magnetic axis hang on a fixed quartz thread. The system is placed in a copper tube with two windows (cf. Fig. 2.3. Through one of them, the magnet and its blocking system can be observed, the other has a self-focussing glass which can detect rotations of the magnetic equipment. When the quartz thread is twisted by a complete number of half-turns, the magnet is removed from the magnetic meridian by a measurable angle α. The sine of this angle is inversely proportional to the horizontal component H of the Earth's magnetic field:

$$H \propto \frac{1}{\sin(\alpha)}$$

Figure 2.3: A Quartz Horizontal Magnetometer. The vertical tube houses the quartz fibre, the twisted magnet can be observed through the horizontal tubes. The foot screws allow for the levelling of the instrument. Courtesy: Geological Survey of Canada.

The QHM calibration parameters are the magnetic moment of the suspended magnet, the torsion constant of the Quartz fibre and an angle offset. Once calibrated in an observatory where the H component is known, the instrumental constants are extremely stable. For this reason and because the precision in the H value is up to $1\,\mathrm{nT}$ for a correctly calibrated instrument, QHMs are called *semi-absolute* instruments (cf. Jankowski and Sucksdorf, 1996) and have frequently been used for field surveys in the past. More details about the QHM, its calibration parameters and the measurement procedure can be found for example in Wiese et al. (1960).

Absolute instruments

For calibration purposes of the before-mentioned variometers, regular absolute measurements are necessary. The procedures are different for vectorial and scalar instruments measurements. The most popular instruments are presented in the following:

Proton Precession and Overhauser Magnetometer

A Proton Precession Magnetometer (PPM) is an absolute, scalar instrument taking advantage of the quantum mechanical magnetic properties of an atom nucleus. It consists of a bin containing a Proton-rich liquid like water or alcohol surrounded by a coil. A current flowing through the coil generates a field stronger than the Earth's magnetic field

and aligns the magnetic moments of all protons. After the switch-off of the exciting field, the protons start precessing about the Earth field with a frequency proportional to the geomagnetic field intensity.

The basic principle of this method is the proportionality between the Proton magnetic moment $\vec{\mu}$ and its nuclear spin $\vec{I}$:

$$\vec{\mu} = \gamma \cdot \vec{I}, \tag{2.4}$$

where γ is the gyromagnetic ratio ($\gamma = 2.675153362 \cdot 10^8 (\text{T}^{-1}\text{s}^{-1})$). In the background field $\vec{H}$ the moment $\vec{\mu}$ experiences the torsional moment

$$\vec{D} = \vec{\mu} \times \vec{H} \tag{2.5}$$

and starts precessing. The angular velocity of the precession is the ratio between angular moment and spin:

$$\omega_P = \frac{D}{I} = \gamma \cdot H \,, \tag{2.6}$$

so that we can write the precession frequency as

$$\nu_P = \frac{1}{2\,\pi}\,\gamma \cdot H \,. \tag{2.7}$$

Measuring the field intensity is thus only a question of measuring the precession frequency and can be done by the field generating coils itself. The measurement result only depends on the frequency and the gyromagnetic ratio and is thus insensitive to external influences such as temperature changes. One drawback of PPMs is that the polarisation and the frequency measurement have to be performed subsequently which defines an upper boundary for the sample frequency of about $1/3$ Hz. Due to the signal-to-noise ratio the accuracy of a PPM amounts to 0.1 nT

A further development of the PPM is the Overhauser magnetometer. In this instrument, the polarisation of the electrons is not generated by high supplementary fields, but by a nuclear polarising effect first described by Overhauser (1953). The liquid not only contains protons, but also unpaired electrons, so called free radicals, that can be excited by exposure to a radio frequency. Exploiting the Overhauser effect, their excitation is transferred to the protons that start precessing about the Earth's magnetic field as described above. As the radio frequency field is transparent for the measurement itself, excitation and measurement can be performed simultaneously and a continuous registration is possible. Another advantage over the PPM is the lesser power consumption due to the polarisation mechanism.

A PPM or Overhauser magnetometer can also be used for a vectorial measurement, if Serson's method (Serson, 1962) is applied. An additional coil is set up around the scalar sensor that generates additional fields along and contrary to the direction of interest, e.g. the horizontal intensity. Without supplementary field, the scalar intensity (F) is composed of the horizontal (H) and the vertical (Z) component:

$$F^2 = H^2 + Z^2 \,. \tag{2.8}$$

An additional field K in horizontal direction yields

$$F_+^2 = (H + K)^2 + Z^2 = F^2 + K^2 + 2KH \; . \tag{2.9}$$

If the current in the coil is reversed, the additional field is directed in the opposite direction and has to be subtracted:

$$F_-^2 = Z^2 + (H - K)^2 = F^2 + K^2 - 2KH \; , \tag{2.10}$$

accordingly, the sum and difference of these additional fields are

$$F_+^2 + F_-^2 = 2\left(F^2 + K^2\right) \qquad F_+^2 - F_-^2 = 4KH \; . \tag{2.11}$$

Then H can be expressed by these scalar fields only.

$$H = \frac{F_+^2 - F_-^2}{2\sqrt{2\left(F_+^2 - F_-^2 - 2F^2\right)}} \; . \tag{2.12}$$

The exact coil parameters do not have to be known, because Eq. (2.12) only considers the measured fields F_+ and F_-, not the value of the additional field K. Rotating the coil to various positions in the horizontal plane, the measured field changes like a sine function dependent on the angle of rotation. An harmonic fitting procedure returns the value of the horizontal component H and, if a reference is given, also the phase or declination.

DI-Flux measurements

Since the 1980s, the standard instrument for absolute measurements of the field components is the Declination-Inclination Fluxgate magnetometer (DI-Flux, cf. Kring Lauridsen, 1985). An iron-free theodolite is equipped with a single-axis magnetometer on-top its telescope. Finding all telescope positions where the magnetometer indicates zero field in the horizontal and in the meridional plane allows for the absolute determination of the field inclination and declination by a simple averaging.
The first, crucial step of the measurement procedure is the levelling of the theodolite, so that the theodolite vertical axis is exactly upright. The observer then sights an azimuth mark to which the geographical direction is exactly known. In practice, the azimuth can either be an existing land mark like a church tower or a mast, or a specially established mark like a cross painted on a distant building. In any case, the azimuth should be far enough away and sighted accurately, because the complete measurement depends on the preciseness of the orientation. We denote the horizontal circle reading of the azimuth mark C and the true geographical azimuth A_z. For the declination measurement, the telescope with the sensor on-top is brought into a horizontal position and the theodolite is turned about its vertical axis until the sensor measures zero field. In this position, the sensor is perpendicular to the horizontal magnetic field. Four different configurations of zero field in the horizontal plane are possible: with the sensor on-top ("*up*") or below ("*down*") the telescope and pointing to magnetic east or west. We tag the associated

circle readings A_E^up, A_W^up, $A_\mathrm{E}^\mathrm{down}$ and $A_\mathrm{W}^\mathrm{down}$ respectively. The reading A to magnetic north is then the mean of these four quantities:

$$A = \frac{A_\mathrm{E}^\mathrm{up} + A_\mathrm{W}^\mathrm{up} + A_\mathrm{E}^\mathrm{down} + A_\mathrm{W}^\mathrm{down}}{4} \tag{2.13}$$

and we obtain the magnetic declination from the differences

$$D = A - (C - A_z). \tag{2.14}$$

By this simple average, all collimation errors between the sensor and the telescope cancel out.

The measurement of the inclination is performed similarly. The horizontal circle is now moved to the before-calculated angle A, so that the telescope aligns with the magnetic meridian. It is then turned about the horizontal axis, until the sensor points perpendicular to the total field. This is the case in two opposite positions with vertical reading V_1 and V_2 and in two more positions (V_3, V_4) after the theodolite is flipped about his vertical axis by 180°. The mean inclination is the average of these four quantities, shifted by 90°:

$$I = \frac{V_1 + V_2 + V_3 + V_4}{4} + 90°. \tag{2.15}$$

Again, all collimation errors are eliminated due to the averaging.

The determination of the complete field vector still requires the knowledge of the total intensity. Ideally, this would be a measurement of F at exactly the same time and the same place. In practice, however, this is not feasible. Usually, the recordings of a continuously running, remote Overhauser or PPM (e.g. in the variation hut) are considered for this purpose. The difference in field intensity between the DI and the remote location (the *pillar difference*) has to be determined regularly to assure that it stays constant.

The accuracy of a DI-flux measurement strongly depends on the diligence and the experience of the observer. Major errors can arise if the theodolite is not levelled accurately, if the azimuth mark is not sighted correctly, or the angles are not read precisely. As the standard procedure requires 18 different positions and readings, one erroneous reading can make the complete measurement obsolete. The accuracy achieved by well-trained personal is in the order of 10arcsec for declination and 5arcsec for inclination measurements.

2.1.2   Data products

Before moving on to the newest instrument developments, I would like to describe the procedures necessary to turn the measurements into typical observatory data products.

After variation and absolute measurements are taken, several postprocessing steps have to be applied to obtain publishable data. First and maybe most important is the *baseline adoption*. During this process, the relative variation measurements are related to the
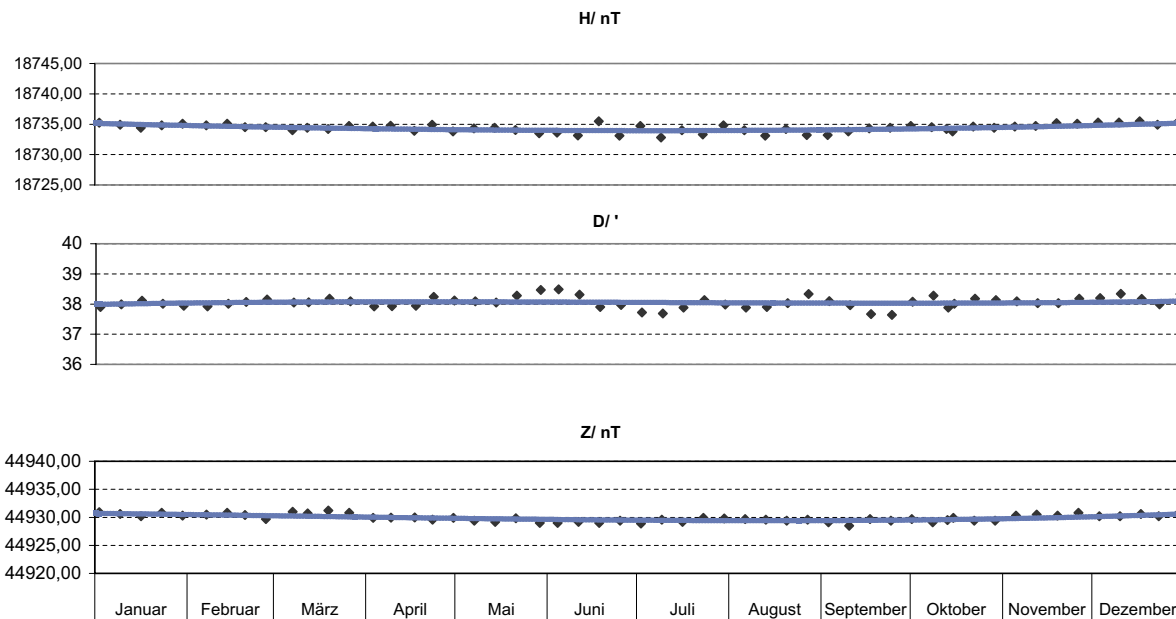
Figure 2.4: Example of a baseline from Niemegk observatory for 2008. Absolute measurements are performed weekly (black diamonds) and baseline adoption is done continuously (blue line). Courtesy of Adolf-Schmidt Observatory, Niemegk.

absolute values. The baseline adoption can be done piecewise or continuously: either the reference to the absolute measurements is applied statically for e.g. one month (see for example the Tsumeb baseline in Fig. 4.4) or splines are used for a continuous adoption (cf. Fig. 2.4). Piece-wise adoption is problematic because jumps from one month to the next are generated that have no natural origin. However, some few observatories use this mathematically much easier method. The advantage is that the resulting *definitive* data (after baseline adoption) are available soon, whereas data produced with continuous baseline adoption are only available with a year of delay.

The variometer sample frequency is normally 1s or 5s. This temporal resolution is higher than needed by the largest part of the data users. Therefore, *minute* and *hourly* mean values are also produced and the latter ones supplied to the *World Data Centre for Geomagnetism* in Edinburgh[1]. Prior to digital recording, hourly means were determined from analogue magnetograms by using a glass scale to estimate visually the mean value. Since the beginning of digital magnetometry, the calculation is a simple arithmetic average of one-minute values, starting at minute 0 and ending at minute 59 of the hour. Mandea (2002) first indicated that one has to be careful how many out of the 60 data points are actually used in the determination of hourly mean values and suggests an upper limit of 10% of missing minute data. This limit is also required to keep the INTERMAGNET goal of an accuracy of ± 5nT for definitive vector data. In addition to the definite hourly data reported to the data centre, observatories also publish yearbooks which contain *monthly*

---

[1]http://www.wdc.bgs.ac.uk

and *annual* mean values. Annual means are derived by averaging over all days in a year and which are widely accepted for calculation of the secular variation. Alexandrescu (1998) and more recently Chulliat and Telali (2007) attempt to compile a data base of observatory monthly mean values. Even though the physical meaning of an average over 28 up to 31 days respectively is arguable, they are mostly considered as only weakly contaminated by external signals. Hence, they offer a "first guess" for a measured secular variation that is calculated as the centred difference

$$\dot{E}(t) = \frac{E(t + 0.5\,\text{years}) - E(t - 0.5\,\text{years})}{1\,\text{year}} , \qquad (2.16)$$

where $\dot{E}$ denotes the first time derivative of the monthly mean value E of a field element, e.g. X, Y or Z. By taking this difference, annual and semi-annual variations cancel out and the variation are regarded as secular variation originating in the core.

The data output is normally given in geodetic coordinates that refer to the oblate ellipsoid approximating the surface of the Earth. For field modelling, the vector components as well as the observatory location have to be transferred to geocentric coordinates. The transformation is simple and depends only the Earth's eccentricity e and its flattening f (refer to Langel, 1987, for details). If the flattening of the Earth is ignored, errors can sum up to several nT.

From the observatory data geomagnetic indices are calculated, that are used as proxies for the geomagnetic conditions. The *Kp index* ("*p*lanetarische *K*ennziffer", planetary index), probably the most widely used geomagnetic activity index, was developed by Bartels (1957). It is a generalised mid-latitude index computed at 3-hour UT intervals. Derived from data from 13 subauroral INTERMAGNET observatories, Kp is designed to monitor solar particle radiation by its magnetic effects. Since 1997 the Kp and the related indices ap, Ap, Cp, and C9 are derived at the Adolf Schmidt Geomagnetic Observatory Niemegk [2]. They are widely used in ionospheric and magnetospheric studies and generally recognised as index measuring worldwide geomagnetic activity. The *Km index* is an "improved Kp" mid-latitude geomagnetic activity index computed at 3-hour UT intervals. The advantage over Kp comes from the greater number and better distribution of the 21 contributing observatories.

Also well-known and widely applied is the D_{ST} index (Disturbance Storm Time) as a measure of the equatorial ring current. It is computed at one-hour resolution from the deviation of the horizontal component at the four observatories Hermanus (South Africa), Kakioka (Japan), Honolulu (Hawaii), and San Juan (Puerto Rico), where the solar quiet variation is already subtracted. The observatories are located sufficiently distant from the auroral and equatorial electrojets with an even distribution in longitude. As a measure of the intensity of the auroral electrojet current system, the AE index is computed at one minute resolution.

A more detailed description of geomagnetic indices together with a large data bank of historical and recent indices is provided by the *International Service of Geomagnetic*

---

[2]`http://www-app3.gfz-potsdam.de/kp_index/index.html`

Indices [3] (ISGI) of the *International Association of Geophysics and Aeronomy* footnote`http://www.iugg.org/IAGA/`(IAGA).

2.2 Recent developments in instrumentation

The global coverage of geomagnetic observatories features many gaps. These facilities cannot be installed in the oceans and in remote, hostile regions of the continent. The before mentioned variometers can already be operated automatically, whereas the absolute measurements still require manual performance. Facing this fact, several teams in the world are engaged in the development of automated absolute instruments. Another approach is to improve the data quality in remote places where laypersons perform the absolutes by simplifying the standard measurement procedure. In the following sections, I start by first describing contemporaneous developments in other institutes and then explain in detail the two measurement methods I have been working on: GAUSS as a step towards automated observatories and the DI3 technology which relaxes the requirements placed on the observer.

2.2.1 Contemporaneous developments

Rasson et al. (2009) have been working on the automation of the traditional DI-Flux method. A custom-made non-magnetic theodolite is equipped with optical angular encoders determining the sensor position. The reference to the geographic system is realized by a laser-photocell set-up, that targets to a corner-cube reflector. Controlled by a microcontroller, the zero position is sought while the instrument is rotated by piezo motors. The classical measurement protocol, consisting in the azimuth reading and subsequent D and I reading is performed step by step. Results look promising, and the instrument is currently tested under semi-remote conditions in the Conrad observatory in Austria (Rasson, pers. communication).

The approach of Auster et al. (2008) consists in automating a *Vector Proton Magnetometer* (VPM). Serson's method described above is used, at which an additional coil rotating in the horizontal plane allows to resolve all three components. For the determination of the reference system, a commercially available webcam is mounted on-top of the coil. The driving system analyses the webcam images and searches for a predefined figure, e.g. a cross, that is located at a known azimuth mark.

---

[3]`http://isgi.cetp.ipsl.fr/`
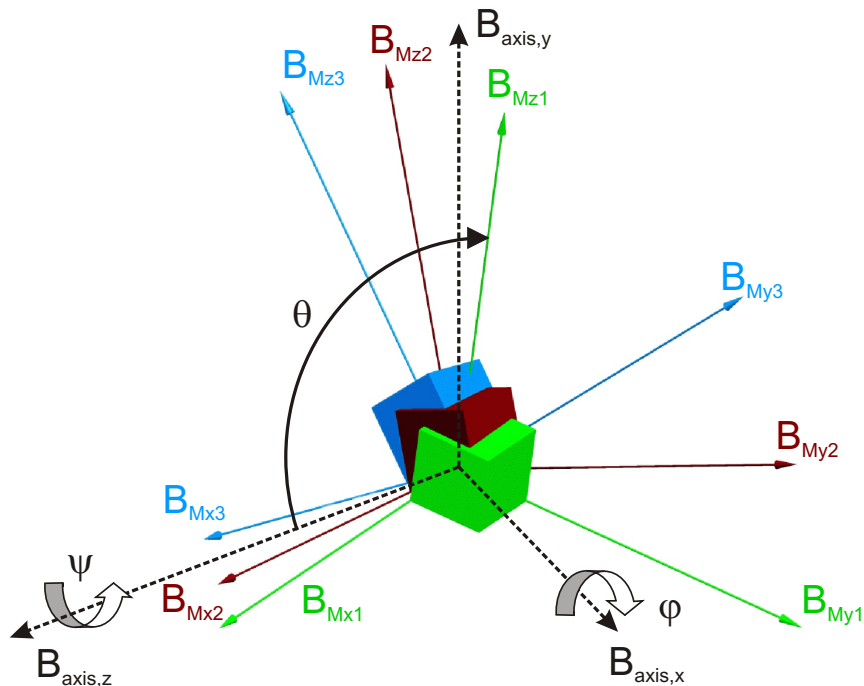
Figure 2.5: Two coordinate systems are considered, the magnetometer system B_M and the reference system B_{axis} which are related by Euler transformation about the angles (φ, ϑ, ψ) with the following set of rotations: first, the magnetometer is rotated about its $B_{Mz} - axis$ until B_{Mx} is parallel to the node line of the $B_{axis,x}$-$B_{axis,y}$ and B_{Mx}-B_{My} planes, next about this node line until B_{Mz} coincides with $B_{axis,z}$ and finally about $B_{axis,z}$ until the two coordinate systems overlap.

2.2.2 GAUSS

Instead of automating the DI-Flux method which was designed for observers familiar with the sophisticated operation of a theodolite or the bulky VPM, we show an alternative approach of absolute measurement of the geomagnetic field. GAUSS, the Geomagnetic AUtomated SyStem was developed in a cooperation of GFZ Potsdam and TU Braunschweig. Our instrument determines the field intensity in two horizontal directions by means of rotations of a three axial fluxgate magnetometer about well-defined axis and computes the third component with the additional information about the field intensity. I review the mathematics behind the measurement procedure and explain the different necessary components used in the set up in the Adolf-Schmidt observatory in Niemegk.

If a three component fluxgate magnetometer is turned about the Z-axis of a geographic reference system ($B_{axis,x}$, $B_{axis,y}$, $B_{axis,z}$), the magnetic field components in the magnetometer system (B_{Mx}, B_{My}, B_{Mz}) are related to the former system by an Euler transformation

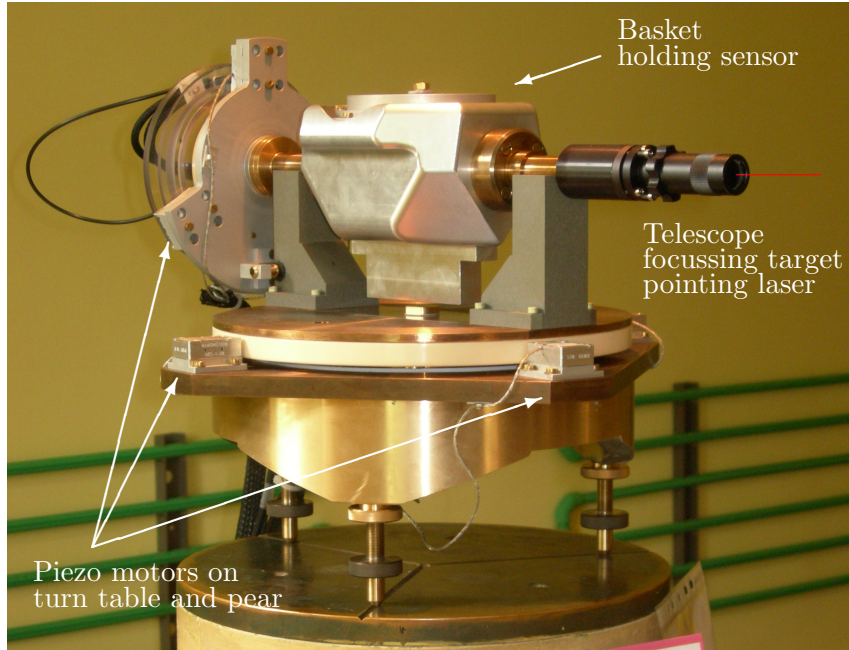**Figure 2.6:** The **G**eomagnetic **AU**tomated **S**y**S**tem in Adolf Schmidt Geomagnetic Observatory Niemegk. Set up on an observatory pillar and carried by three foot screws, the instrument main parts are the basket containing the fluxgate magnetometer (in the centre), the telescope focussing the laser light (right) and the pear performing the rotation about the horizontal axis.

about the angles $(\varphi, \vartheta, \psi$ (cf. Fig. 2.5):

$$
\begin{bmatrix}
\cos\varphi\cos\psi - \sin\varphi\sin\psi\cos\vartheta & \sin\varphi\cos\psi + \cos\varphi\sin\psi\cos\vartheta & \sin\psi\sin\vartheta \\
-\cos\varphi\sin\psi - \sin\varphi\cos\psi\cos\vartheta & -\sin\varphi\sin\psi + \cos\varphi\cos\psi\cos\vartheta & \cos\psi\sin\vartheta \\
\sin\varphi\sin\vartheta & -\cos\varphi\sin\vartheta & \cos\vartheta
\end{bmatrix}
$$
$$
\times \begin{pmatrix} B_{Mx} \\ B_{My} \\ B_{Mz} \end{pmatrix} = \begin{pmatrix} B_{\text{axis},x} \\ B_{\text{axis},y} \\ B_{\text{axis},z} \end{pmatrix} \quad (2.17)
$$

If $(B_{Mxi}, B_{Myi}, B_{Mzi})$ are recorded at three different positions ($i = 1, 2, 3$, $\varphi = \varphi_0 = \text{const}$, $\vartheta = \vartheta_0 = \text{const}$, $\psi = \psi_i$) during one rotation, the field strength along the rotation axis can be calculated using the following equation:

$$
B_{\text{axis},z} \begin{pmatrix} 1 \\ 1 \\ 1 \end{pmatrix} = \underbrace{\begin{bmatrix} B_{Mx1} & B_{My1} & B_{Mz1} \\ B_{Mx2} & B_{My2} & B_{Mz2} \\ B_{Mx3} & B_{My3} & B_{Mz3} \end{bmatrix}}_{\mathbf{B_m}} \underbrace{\begin{pmatrix} \sin\varphi\sin\vartheta \\ -\cos\varphi\sin\vartheta \\ \cos\vartheta \end{pmatrix}}_{\vec{n}(\varphi,\vartheta)}
$$
$$
= \qquad\qquad \mathbf{B_m} \qquad\qquad \cdot \qquad \vec{n}(\varphi,\vartheta) \qquad (2.18)
$$

Due to the fact that $\vec{n}(\vartheta, \varphi)$ is a unit vector, Eq. (2.18) can be resolved by inverting the matrix $\mathbf{B_m}$ and calculating the modulus. Thus, the field magnitude in direction of the

rotation axis becomes independent of the sensor orientation and can be expressed by:

$$|B_{\mathrm{axis},z}| = \left\| \mathbf{B_m^{-1}} \begin{pmatrix} 1 \\ 1 \\ 1 \end{pmatrix} \right\|^{-1}$$

$$
\begin{aligned}
= (\det \mathbf{B_m})^{-1} \times [&(B_{Mx1}(B_{My3}-B_{My2})+B_{Mx2}(B_{My1}-B_{My3}) \\
&+B_{Mx3}(B_{My2}-B_{My1}))^2 \\
&+(B_{Mx1}(B_{Mz3}-B_{Mz2})+B_{Mx2}(B_{Mz1}-B_{Mz3}) \\
&+B_{Mx3}(B_{Mz2}-B_{Mz1}))^2 \\
&+(B_{My1}(B_{Mz3}-B_{Mz2})+B_{My2}(B_{Mz1}-B_{Mz3}) \\
&+B_{My3}(B_{Mz2}-B_{Mz1}))^2]^{-\frac{1}{2}}
\end{aligned}
\tag{2.19}
$$

Although the angles don't play a role in calculating $B_{\mathrm{axis},z}$, it is still possible to determine approximate values for φ, ϑ and ψ in order to use them for a later variation reduction. If measurements are done for two orientations of the rotation axis and if additional scalar absolute intensity data are given, the field vector can be determined completely. Systematic errors have to be eliminated during the measurement to make the measurement absolute. A scalar calibration of the fluxgate magnetometer is obtained by comparison of proton magnetometer readings with the field magnitude derived from measurements of the fluxgate magnetometer at various orientations with respect to the Earth's magnetic field vector. To increase the diversity of sensor orientations with respect to the geomagnetic field for calibration purposes and to increase the redundancy of measurements, the procedure should be repeated after a 90° rotation of the sensor perpendicular to the measurement axis (later called sensor orientation I & II).

An automation of this method is promising since the precision requirements of mechanical operations are low compared to those of the DI-flux method. The rotation of the sensor can be done with arbitrary angles because the field determination along the rotation axes is independent of the sensor orientation. Only the directions of the two rotation axes need to be determined precisely in order to allow for an accurate transformation of the data into a geographical reference frame.

The main instrument as it was assembled in the Adolf Schmidt Geomagnetic Observatory in Niemegk is shown in Fig. 2.6. To accomplish automation, three main tasks have to be covered: magnetics, mechanics and optics. A digital fluxgate magnetometer was provided by Magson GmbH. Its sensor, designed at Technische Universität in Braunschweig, has a diameter of only $5 \times 5 \times 5 \mathrm{cm}^3$ so that it can easily fit in the so-called basket (cf. Fig. 2.6). The intensity and variometer data are obtained from the observatory measurements. To determine the orientation of the measurement direction, a laser beam is aligned with it. Piezo motors with optical encoders drive the upper part of the instrument roughly to a predefined measurement direction where the laser beam hits a *Position Sensitive Device* (PSD) which returns the exact orientation. As for all magnetometers, special diligence has to be paid to the magnetic cleanliness of all components.

On April 18, 2008, GAUSS was set up in the absolute house at the Niemegk observatory. Since then, the instrument has measured the magnetic field once per day at midnight.
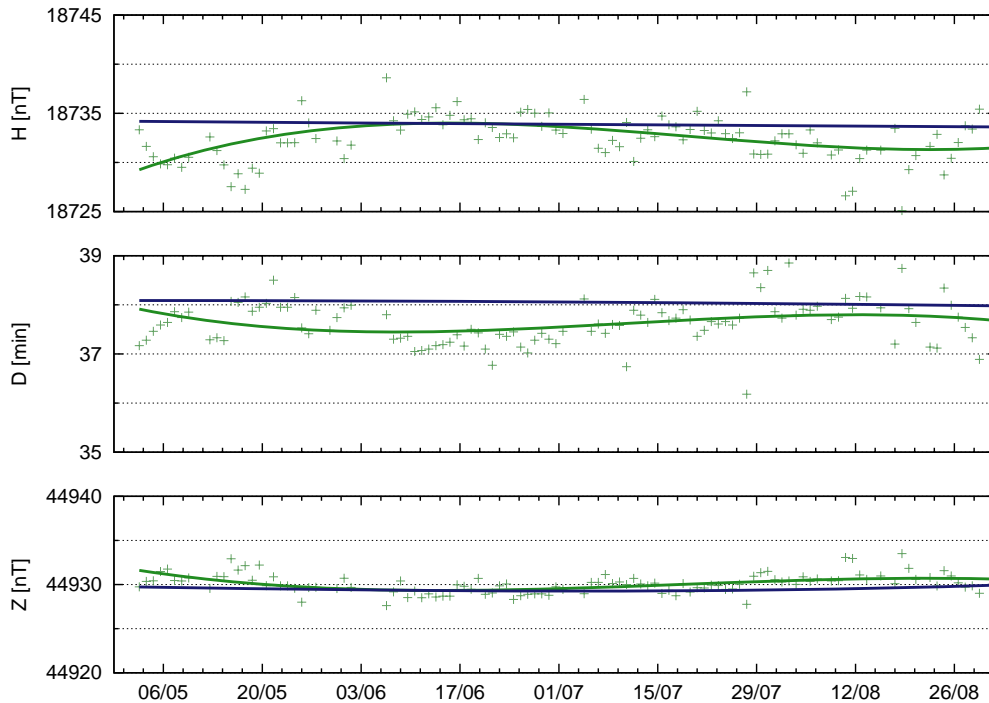
Figure 2.7: Baselines for H (top), D (centre), and Z (bottom) component derived from GAUSS's daily measurements (green) and compared to the official Niemegk baseline (blue). Lines show calculated baselines, crosses single measurements.

The magnetic conditions are most quiet at this time of the day, and no daylight disturbs the optical sensors. The daily measurement procedure starts with a recalibration of the table and the basket angle encoders. The basket then turns forward and backward by 360° using six steps of 60° for each direction. During these measurement steps the laser beam targets the first PSD mounted on a ceramic pillar outside the absolute house. The sensor inside the basket is then shifted to its second position and the turning of the basket is repeated. The table rotates the entire upper structure towards the second PSD, and the measurement of the magnetic field along the second axis is performed as described before.

Figure 2.7 shows the NGK baseline resulting from measurements performed with a DI-flux in comparison with the GAUSS ones. Although we have no definite explanation for the small drift of the D-component during a few weeks, we suppose that one of the pillars the PSDs are mounted on is tilting.

The first version of the instrument is described in Auster et al. (2007) and extensively in Hemshorn (2007). Improvements applied are summarised in Hemshorn et al. (2009b).

Figure 2.8: The DI3 instrument: A Zeiss theodolite equipped with a three component fluxgate sensor.

2.2.3   DI3

The standard DI-flux method uses a one component sensor to determine the directions of zero field. As heritage of space missions three component fluxgate sensors are nowadays able to measure the full range of the Earth's magnetic field. Those instruments feature a linearity better than 1nT in a 60000nT range. Replacing the single axis sensor on the telescope of a DI-instrument by such a three component sensor obviously provides additional information of the geomagnetic field. This additional information can be used for simplifying the measurement procedure and for obtaining a higher number of single absolute measurements. Considering the establishment of several observatories in remote regions where laypersons are in charge of the absolutes, the method presented here can improve measurement results by shifting a certain degree of accuracy from the on-site observer to the mathematical postprocessing. This is the aim of the *DI3* instrument, that was first described in Hemshorn et al. (2009a).

Set-up

A vector-compensated fluxgate sensor, supplied by Technische Universität Braunschweig is mounted on top of a Zeiss 020B theodolite (see Fig. 2.8). The set-up orientation of the sensor can be arbitrary, its alignment with respect to the reference system of the Zeiss theodolite can be derived from field values sampled during the measurement procedure. The magnetometer system is similar to the one used for GAUSS. The instrument system time is synchronised by a GPS receiver and data from a scalar magnetometer and a flux-
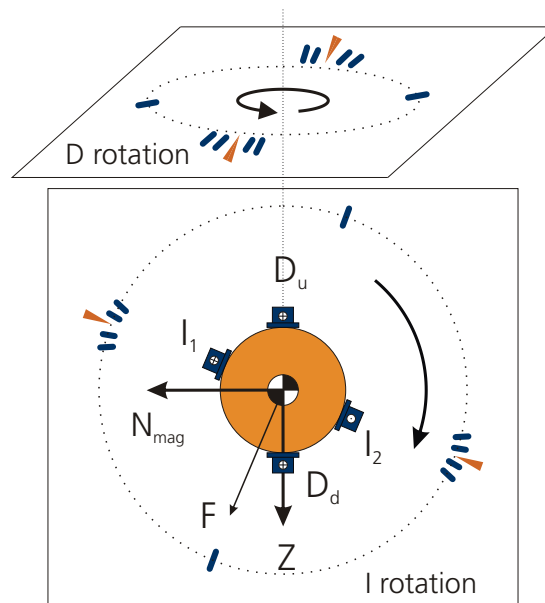
Figure 2.9: During a DI3 measurement, D- and I- rotations are performed in indicated planes. Blue ticks show the positions where samples are taken: four positions close to the standard ones (orange marks), one position in between. The blue sensor is drawn in positions where angle readings are taken in the classical procedure (normal to F), D_{up}, D_{down}, I_1 and I_2.

gate variometer can be received on request via radio link.

The measurement procedure is analogue to that of a DI flux. After levelling, the coordinates of the azimuth mark are read and rotations about the vertical axis (D-rotation) and the meridional axis (I-rotation) are performed. Pointing the azimuth and D rotations are carried out as well in upper as in lower sensor position (see Fig. 2.9). The I-rotation is done at two opposite horizontal angles. With the traditional method, these four rotations are carried out until the single axis magnetometer indicates zero and the theodolite angles are read. The horizontal angle for the I-rotation is derived from the D-rotation results.

Due to the fact that the magnetometer covers the full magnetic field vector, we do not rely on measurements perpendicular to the Earth field vector. Therefore, readings can be taken at predefined angle combinations. In a first case study we decided to take 10 magnetometer readings during each rotation at different angles. In principle, the number (≥ 3) and angular repartition of the samples per rotation can be adjusted in one's sole discretion. To be close to the traditional method, we agreed on an angular distribution according to Fig. 2.9. Samples are additionally taken at the azimuth adjustments before and after the D rotation, so that we have all together 44 magnetometer readings.

A program executed on a hand-held pc quotes the predefined angles that have to be placed on the theodolite. The position then only has to be confirmed and data from variometer and scalar magnetometer are sampled and stored in the raw file together with the belonging angle.

Calculation of Field Values

The computation of actual field values from the raw data take a number of processing steps:

In a first step, all fluxgate measurements can by reduced by the field variation. Assuming field variations below 100nT, a draft knowledge of the angular position within $\pm 0.5°$ of each measurement is sufficient for variation reduction

In a second step, the magnetometer can be fully calibrated, simply by means of rotation, without exploiting the angle readings. The field in direction of the rotation axes can be calculated, and the transformation matrix from sensor to theodolite coordinate system can be derived. For scalar calibration, (i.e. the determination of offsets, scale values and orthogonality by comparison of calculated field magnitude with the parallel absolute scalar measurement) the rotation about two independent axes is sufficient (Auster et al., 2002). The field along the direction of the rotation axis can be calculated by three field values sampled at different angular positions by the following equation (Auster and Auster, 2003):

$$|B_Z| = \left\| \mathbf{B_m}^{-1} \begin{pmatrix} 1 \\ 1 \\ 1 \end{pmatrix} \right\|^{-1} \tag{2.20}$$

where $\mathbf{B_m}$ is a matrix containing line by line vectors of three samples selected from the ten taken during one rotation.

The field values derived in this way are marked with blue squares in Fig. 2.10. Finally, if we know the field in the direction of the rotation axis we can determine the misalignment of the fluxgate coordinate with respect to the rotation axis. Two samples B_1 and B_2 are necessary to derive the angles according to

$$\sin \vartheta = \frac{-B_{y,2}(B_{z,1} - B_Z) + B_{y,2}(B_{z,2} - B_Z)}{B_{x,2}B_{y,1} - B_{x,1}B_{y,2}} \tag{2.21}$$

$$\sin \varphi = \frac{-B_{x,2}(B_{z,1} - B_Z) + B_{x,1}(B_{z,2} - B_Z)}{B_{x,2}B_{y,1} - B_{x,1}B_{y,2}} \tag{2.22}$$

Doing this calculation for both rotation axis, we get one angle of misalignment twice and can use this to check the error bar of the alignment matrix. With this matrix we can transform the magnetometer data from the sensor coordinate system into the theodolite system.

In a third, final step, we exploit the angle readings. Using these angles we can transform all magnetometer readings into the geographic reference system. These results are plotted in Fig. 2.10 by red diamonds.

Advantages

The use of a three-component magnetometer for a standard DI measurement has numerous advantages:
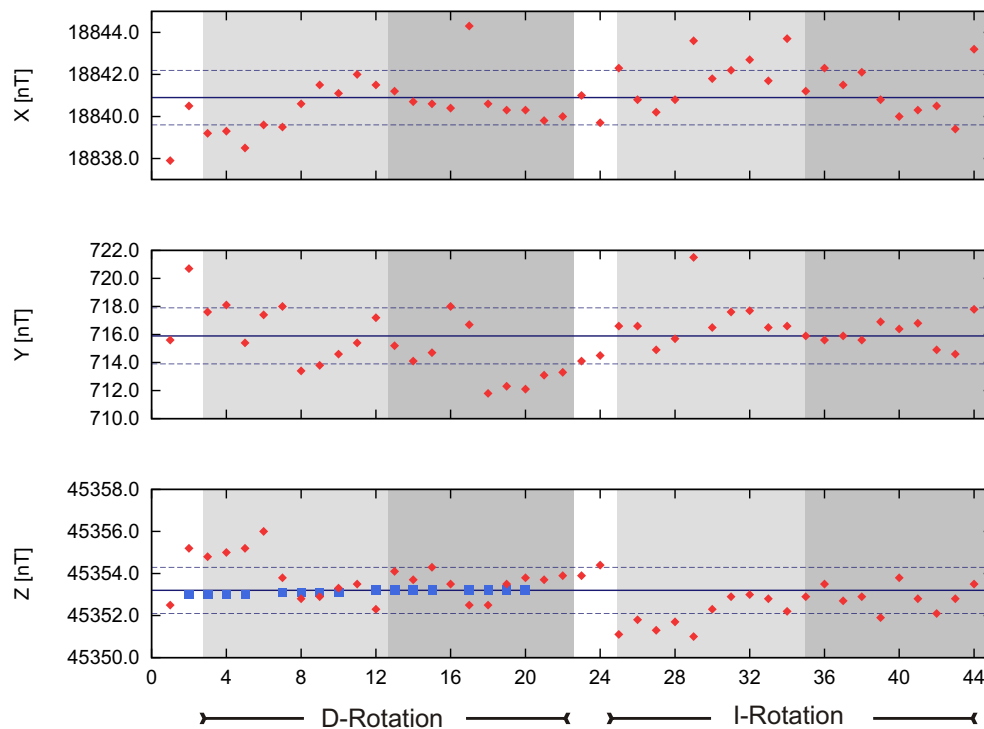
Figure 2.10: Result of an absolute measurement by DI3 consisting of 44 samples. Each individual absolute measurement is marked by a red diamond. For comparison, the Z-components of the field determined in spin axis directions are plotted as blue squares. Sectors with different theodolite positions (D_{up}, D_{down}, I_1 and I_2) are separated by the alternating background shadings. Standard deviations for $[X; Y; Z]$ are $[0.65nT; 1.0nT; 0.55nT]$.

Reduction of random errors: The large number of absolute measurements during one sequence can help to reduce random measurement errors (e.g., angle reading errors). Fig. 2.10 shows the result for all three components derived from one measurement procedure. Using a Zeiss 020B single measurements deviate up to 5 nT, but due the large number of single measurements, the confidence interval given by the standard deviation is in the order of 1-2 nT. This is competitive with results achieved in observatories by well trained personal during IAGA workshops (Reda and Neska, 2007). Using a DI3, the higher numbers of measurements per sequence increases the confidence for the mean value. Performing a standard DI-Flux procedure, in contrast, causes random errors to accumulate because each individual reading contributes to the calculation of D and I.

Detection of fatal errors: Fatal errors like misadjustment of angle positions can easily be detected. As our procedure features a high redundancy, those measurement points

Figure 2.11: An artificial field gradient has been applied on the DI3 instrument by using a Helmholtz system with opposite connected rings. The field gradient leads to differences at the sensor positions drawn on the right side.

can be removed without losing the whole absolute measurement. This makes the procedure less vulnerable to errors of less trained observers. During the field measurements, theodolites are sensitive to heating from the sun and can tilt. With our procedure, the tilting can be quantified and all single measurements can be reduced to the start, when the levelling was still acceptable.

Elimination of systematic errors: Systematic errors, such as field gradients between upper and lower sensor positions, can be separated by the DI3 method. With the standard DI-Flux method, field gradients in only one direction can be discovered. To prove this, we set up a Helmholtz coil system with opposite connected coils around the theodolite (see Fig. 2.11) and took measurements with artificial field gradients of 5nT/cm. The result is striking: Perturbing field gradients can be detected easily (see Fig. 2.12).

Adjustable preferences: Preferred angle adjustments can be determined automatically after the azimuth mark reading because the approximate orientation between the pillar / azimuth mark system and the magnetic field vector is fixed. Therefore, measurement angles can be predicted by the sequence control automatically for each pillar. Hence, a pocket PC was configured that quotes the predefined angles that only have to be approved.

User friendly: The predefined angles only have to be approved and data are sam-
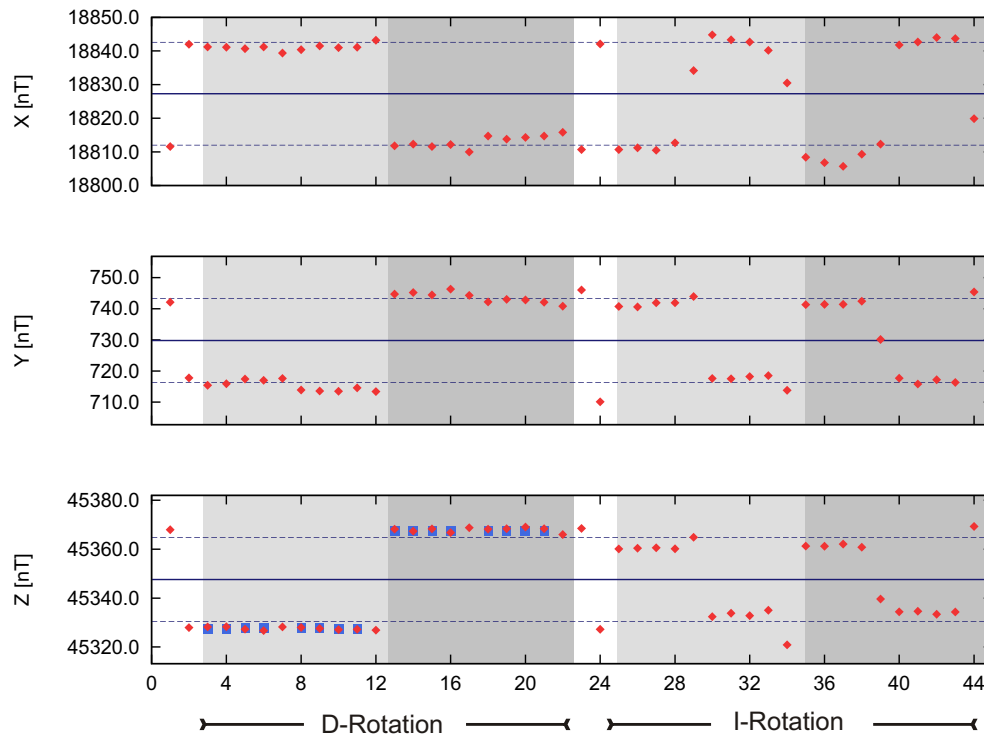
Figure 2.12: Result of an absolute measurement made with artificial field gradients. The error can clearly be separated.

pled automatically. Thus, the observer does not have to be very experienced to obtain satisfying results. Furthermore, all measurements are directly available in digital form allowing for speedy processing and suppressing typos.

Close to standard: Finally, with implementing a 3D fluxgate sensor we offer no disadvantage to observers who prefer the traditional method. By using only one axis, the DI flux method can be applied as usual.

Using a three-component sensor instead of a single-axis instrument increases the redundancy and thus the accuracy of a DI fluxgate measurement. Systematic errors can be detected. Erroneous values can be dropped and random errors can be minimised by increasing the number of angle readings. The requirements on the observer are relaxed: time, magnetometer output and variometer readings are recorded automatically. Angle readings are only necessary at discrete (rounded) angles. The requirements on the theodolite quality can as well be relaxed.

In summary, the automated instrument GAUSS as well as the "faciliating" DI3 instrument

have plenty of future in the equipment of new observatories. The big advantage of GAUSS is that it can run fully automated, although the absolute control of orientation remains the critical point. Levelling and orientation are also critical for the DI3, but can be handled more easily by a real observer.

2.3 Repeat stations

National research facilities commonly carry out regional field measurements on a regular basis leading to spatially highly resolved data sets. Those field surveys provide absolute data on a scale that is finer than the observatory net but at a substantially reduced time resolution. Additionally, *repeat station surveys* attempt to track the secular variation as which they have to be distinguished from from ground vector measurements which rather target to map the field or even crustal anomalies.

I give here some general characteristics of repeat station surveys citing the well developed European network as an example. More details about the South African network analysed in this thesis is given in chapter 4.2. The standard guidebook in this context is the "IAGA guide for geomagnetic repeat station survey" by Newitt et al. (1996) whose main suggestions are summarised.

2.3.1 Repeat station surveys

As stated above, the main objective of repeat station surveys is the increased spatial resolution. Jankowski and Sucksdorf (1996) as well as the Magnetic Network in Europe (MagNetE, 2003) recommend a minimum density of one station in $15000 \, \text{km}^2$ or a mean station distance of $125 - 200 \, \text{km}$. Fig. 2.3.2 shows the distribution of German stations together with maps of declination and inclination for 2008.

The frequency of measurement campaigns varies from country to country. In Germany for example, half of the network is revisited every year whereas e.g. France performs its measurements every $5 \, years$. To improve the comparability of the results, MagNetE is dedicated to bundle the efforts in the European region. But as every institution has its own traditions, coordinated measurements in some tenth of European countries was not yet performed.

From a global point of view, surveys are even less coordinated. Although the national institutions are encouraged to submit their results to the WDC, the way how the data are obtained and processed differs a lot. However, the main intention is not to carry out global coordinated surveys but to improve and densify measurements at regional scale.

2.3.2 Measurements: Station set-up and data output

A repeat station only requires a permanent mark which allows to clearly identify the measurement positions. This can be either a bronze plague or a plug set in concrete. Sometimes, triangulation stations previously installed by national geodetic institutes are
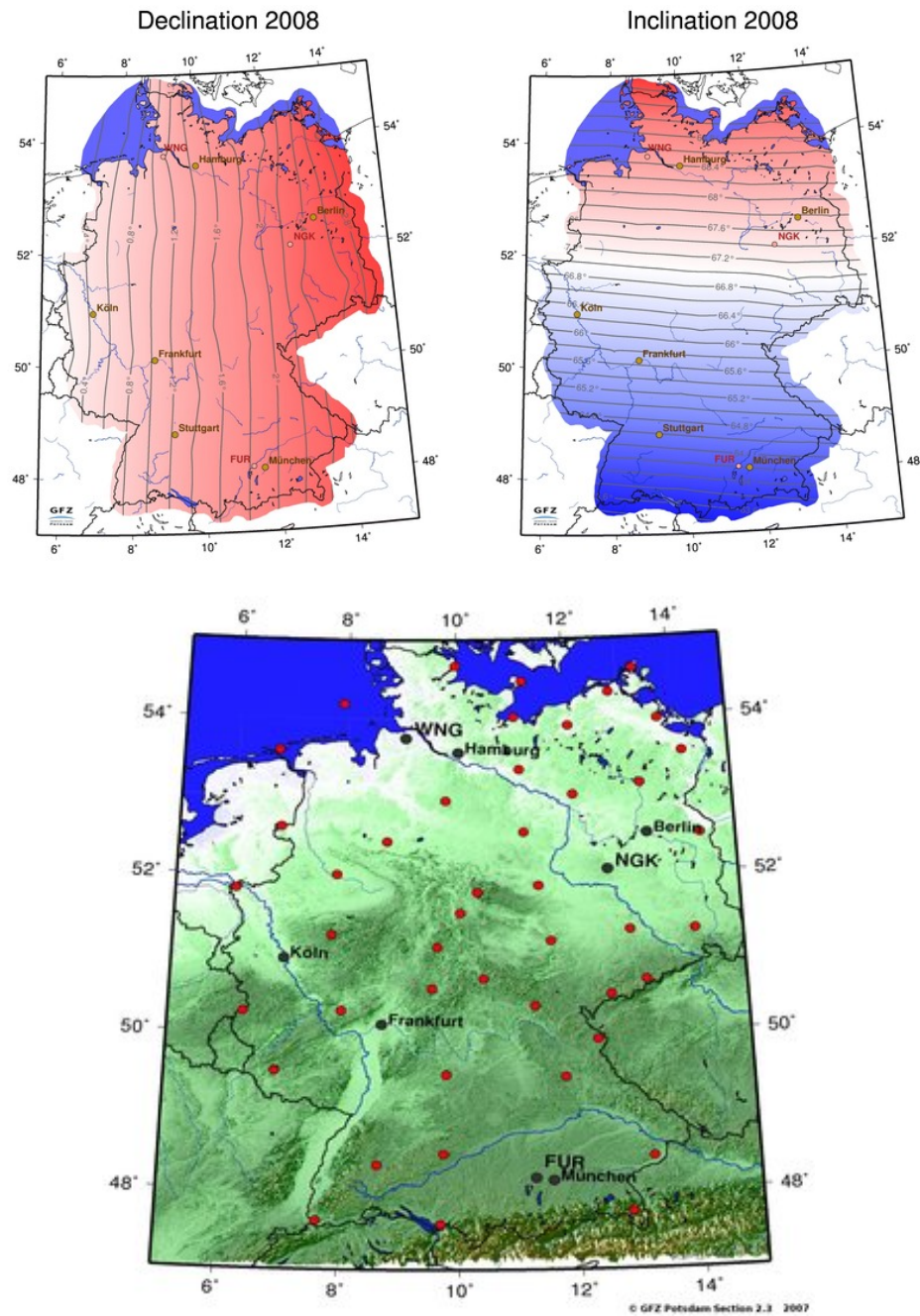
Figure 2.13: The German repeat station network (red dots, centre image) together with maps of the declination (left) and inclination (right) derived for the epoch 2008. Courtesy: GFZ Potsdam, section 2.3.

$$
\begin{array}{llll|llll}
X & \pm\,5\ \text{nT} & - & \pm\,20\ \text{nT} & \dot{X} & \pm\,7\ \text{nT} & - & \pm\,40\ \text{nT} \\
Y & \pm\,4\ \text{nT} & - & \pm\,13\ \text{nT} & \dot{Y} & \pm\,3\ \text{nT} & - & \pm\,26\ \text{nT} \\
Z & \pm\,4\ \text{nT} & - & \pm\,12\ \text{nT} & \dot{Z} & \pm\,3\ \text{nT} & - & \pm\,24\ \text{nT}
\end{array}
$$

Table 2.1: Error estimates for European repeat station surveys according to Korte (1999).

used. If not so, the station exact geographic position is determined by GPS. An auxiliary pillar normally exists in addition where a scalar instrument can be set up. Finally, azimuth marks to identify the measurement orientation have to be selected. As in observatories, those are usually landmarks.

DI flux measurements are performed late in the evening or early in the morning to minimise disturbances from external sources. With a variometer (on site, from a close observatory or from a preliminary variometer station providing data for several surrounding repeat stations), the data can be reduced to the quiet night time. In the final reduction step, the annual mean value for the station is estimated. This can only be done with the closest observatory due to the lack of a very long variometer record at the station. The estimated (annual mean) field component $E(t_e)$ at the repeat station is

$$
E_{\text{FS}}(t_{\text{e}}) = E_{\text{Obs}}(t_{\text{e}}) - E_{\text{Obs}}(t_{\text{s}}) + E_{\text{FS}}(t_{\text{s}})
$$

where t_s denotes the epoch of the survey, t_e the epoch to be reduced to and E_{Obs}, E_{FS} are the field components at the reference or control observatory and the field station, respectively. Problems arise if the secular variation at the repeat station differs non-uniformly from the one measured at the observatory. This is the case e.g. in southern Africa, where a strong spatial gradient exists in the secular variation. Again, Jankowski and Sucksdorf (1996) give a good insight into possible error sources due to data reduction. Even more details can be found in Korte (1999), where error estimates for the secular variation are given.

2.4 Satellite measurements

Launched in May 1958 the Russian satellite Sputnik 3 brought the first magnetometer into an Earth orbit. Although Sputnik carried a three-component fluxgate magnetometer, its accuracy was only of the order of 100nT. Since then, several spacecraft investigated Earth's magnetic field from space with increasing precision.

2.4.1 Ancient magnetic satellite missions

The **P**olar **O**rbiting **G**eophysical **O**bservatories POGO was a series of the near-Earth magnetic satellites (POGO 1, 2, and 3) launched in the late 1960ies, in 1965, 1967, and 1969 respectively. Equipped with optically pumped, self-oscillating rubidium magnetometers, POGO offered the monitoring of the scalar magnetic field with a global coverage (Langel, 1967, 1990). Although the POGO mission was primarily designed to develop and

test standardised observatory-type satellites, the global magnetic data coverage allowed for the first time more detailed geomagnetic field modelling. POGO carried search coil magnetometers as well, but these instrument only served for studying wave phenomena, not main field, because no reference orientation was provided.

2.4.2 Recent missions

Acuña (2002) gives a review of modern magnetometers in space. Here, I want to focus to missions which monitor the Earth's magnetic field and provide the important vector data base used for field modelling.

MAGSAT

First precise, globally distributed magnetic vector data were collected by the NASA satellite MAGSAT. On October 30, 1979, it was launched into a twilight, sun-synchronous, retrograde orbit with inclination 96.76°, perigee 352km and apogee 561km (Langel et al., 1982). It remained in orbit for seven and a half months, until June 11, 1980. To provide vector data, precise knowledge of the instrument orientation towards a geographic reference frame is necessary. Position determination was done using a Doppler tracking system. For attitude control, MAGSAT was equipped with two star trackers. The satellite carried a Caesium vapour optically pumped magnetometer as scalar instrument and a three axial fluxgate magnetometer for vector measurements. The latter one sampled the field 16 times per second with a resolution of 0.5nT. Thanks to the very accurate determination of the magnetometer orientation within 20arcsec, the error in the vector data could be estimated below 6nT.

Ørsted

Denmark's first satellite Ørsted was launched February 23, 1999 and still orbits the Earth almost sun-synchronously at altitudes between $630 - 860$km (Neubert et al., 2001). It carries both an instrument for measuring the magnetic field intensity and one to sample the complete vector. The Overhauser magnetometer providing the field strength is situated at the end of a boom of 8m lengths, in order to minimise disturbances from the satellite electrical systems. A *Compact Spherical Coil* (CSC) fluxgate vector magnetometer is used to measure the strength and direction of the magnetic field. It is situated closer to the satellite body in a so-called "gondola", together with the star imager that determines the orientation of both the satellite and the CSC magnetometer. Though still in orbit Ørsted provided vector data only until December 2005.

SAC-C

The SAC-C is an international Earth observing satellite mission developed in a cooperation between the Argentinian space agency CONAE and NASA, with additional support

Figure 2.14: Artist's view of two of the three Swarm satellites. Courtesy: DTU Space.

in instrumentation and satellite development from other international agencies. The SAC-C satellite was launched in November 2000 into a circular, sun-synchronous orbit at 705km altitude with an inclination of 98.2°. Developed by the Danish Space Research Institute and NASA/JPL, the Magnetic Mapping Payload consists of a vector (CSC) and a scalar (SHM) magnetometers. The vector magnetometer is mounted on an optical bench with a non-magnetic star imager camera head (Colomb et al., 2004).

CHAMP

The Challenging Minisatellite Payload (CHAMP) managed by GFZ Potsdam and the German Space Agency (DLR) was launched on July 15, 2000 into a nearly circular, low orbit with an inclination 84° that covers all local times. The high inclination offers global coverage at varying local times. From an initial altitude of 454km, CHAMP descended to 350km during its nominal life time of five years, but is now (2010), still in operation. Along with a scalar and a directional magnetometer, it carries instruments for atmospheric studies like accelerometer, laser retroreflector, and an ion drift meter. The attitude is controlled by star sensors and a GPS receiver provides the reference frame for the two on board fluxgate magnetometers. Although this configuration may be used in a gradiometer mode, the second fluxgate is only on-board for redundancy reasons. The scalar Overhauser magnetometer provides the absolute magnetic field intensity for in-flight calibration of the fluxgates.

Upcoming: Swarm

Scheduled for launch in 2012, the Swarm mission consists of a constellation of three CHAMP alike satellites in different polar orbits between 400 and 550 km altitude. Two spacecraft will fly side by side at the same altitude whereas the third one will orbit the Earth at a higher altitude. Each satellite carries a scalar and a vector magnetometer

including three starcameras for attitude control. The combination of the satellites allows for space-time resolution so that the different sources of the Earth's magnetic field can be resolved. Apart from the high-resolution magnetic field, the satellites will monitor the electric field, plasma density, electron /ion temperature, air density and thermospheric winds.

Chapter 3

Modelling the magnetic field of the Earth: theory and methods

Since Gauss, scientists and mathematicians have derived techniques for describing the shape of the Earth's magnetic field. Depending on the available data and the base functions, those models can be global or regional, time dependent or static. The mathematical description of the different kinds of field models, their physical backgrounds and applicability are the subjects of this chapter. The first section gives an overview of the standard global technique relying on spherical harmonics and the commonly used temporal description with B-splines concluding some example models. Different approaches for regional modelling are presented afterwards. The last section is devoted to harmonic splines which are applicable globally or regionally. The underlying relations are derived, and after presenting the basics of inverse problems and introducing the necessary implementation steps, the spline approach undergoes a functionality test with synthetic data.

3.1 Global field models

The Earth's magnetic field is a world-wide phenomenon, therefore the most obvious approach is to describe it globally. In the following sections, I first derive the basic equations for the spatial description, then switch to the temporal parametrisation afterwards and introduce finally introduce a few examples of current models.

3.1.1 Spatial description

To describe the magnetic field of the Earth, Maxwell's equation offer a good starting point. All magnetic fields are source-free

$$\nabla \cdot \mathbf{B} = 0 \,. \tag{3.1}$$

Considering the steady state, its curl is generated by currents:

$$\nabla \times \mathbf{B} = \mu_0 \mathbf{j} \,, \tag{3.2}$$

37

where $\mu_0 = 4\pi \cdot 10^{-7} \frac{VS}{Am}$ is the vacuum permeability. On the surface of the Earth, between the crust and the ionosphere, the current density $\mathbf{j}$ is negligible, so that the field is curl-free

$$\nabla \times \mathbf{B} = 0 \,, \tag{3.3}$$

and $\mathbf{B}$ can be presented as the negative gradient of a scalar potential V

$$\mathbf{B} = -\nabla V \,. \tag{3.4}$$

Taking the divergence of this identity leads to the Laplace equation for the potential

$$\Delta V = 0 \,. \tag{3.5}$$

To solve this differential equation, it is convenient to work in geocentric spherical coordinates. Then, r describes the radius or distance of a point from the centre, ϑ is the colatitude (or polar angle) measured from the North pole and φ is the longitude (or azimuthal angle) measured from the Greenwich meridian. The Laplace operator Δ in this system of coordinates applied to the potential V can be written as

$$\Delta V = \left[\frac{1}{r^2} \partial_r \left(r^2 \partial_r \right) + \frac{1}{r^2 \sin \vartheta} \partial_\vartheta \left(\sin \vartheta \partial_\vartheta \right) + \frac{1}{r^2 \sin^2 \vartheta} \partial_\varphi^2 \right] V = 0 \,.$$

This partial differential equation is solved by separation of variables, i.e. by considering the potential $V(r, \vartheta, \varphi)$ as the product of a radial and an angular contribution:

$$V(r, \vartheta, \varphi) = R(r) Y(\vartheta, \varphi) \,.$$

The angular function $Y(\vartheta, \varphi)$ is again separated into a polar contribution depending on latitude and an azimuthal contribution depending on longitude. The solution for the potential is then

$$V(r, \vartheta, \varphi) = R_E \sum_{l=1}^{\infty} \sum_{m=0}^{l} \left[\left(\frac{R_E}{r} \right)^{l+1} \left(\tilde{g}_l^m \cos(m\varphi) + \tilde{h}_l^m \sin(m\varphi) \right) \cdot P_l^m(\cos \vartheta) + \right.$$
$$\left. \left(\frac{r}{R_E} \right)^l \left(q_l^m \cos(m\varphi) + s_l^m \sin(m\varphi) \right) \cdot P_l^m(\cos \vartheta) \right] \,. \tag{3.6}$$

As I stress later, the contributions proportional to r^l refer to fields of external, contributions proportional to $r^{-(l+1)}$ to fields of internal origin. To start with, I investigate the angular dependencies closer. The P_l^m are the *associated Legendre functions* of degree l and order m in the Schmidt semi-normalised form.

To shorten the notation used in Eq. (3.6), it is convenient to write

$$\left(\tilde{g}_l^m \cos(m\varphi) + \tilde{h}_l^m \sin(m\varphi) \right) \cdot P_l^m(\cos \theta) = g_l^m Y_l^m(\theta) \tag{3.7}$$

and to count $m = -l, \ldots, l$. Usually, the convention is that negative orders ($m < 0$) are associated with $\sin(m\varphi)$ terms, whereas zero or positive orders ($m \geq 0$) are associated
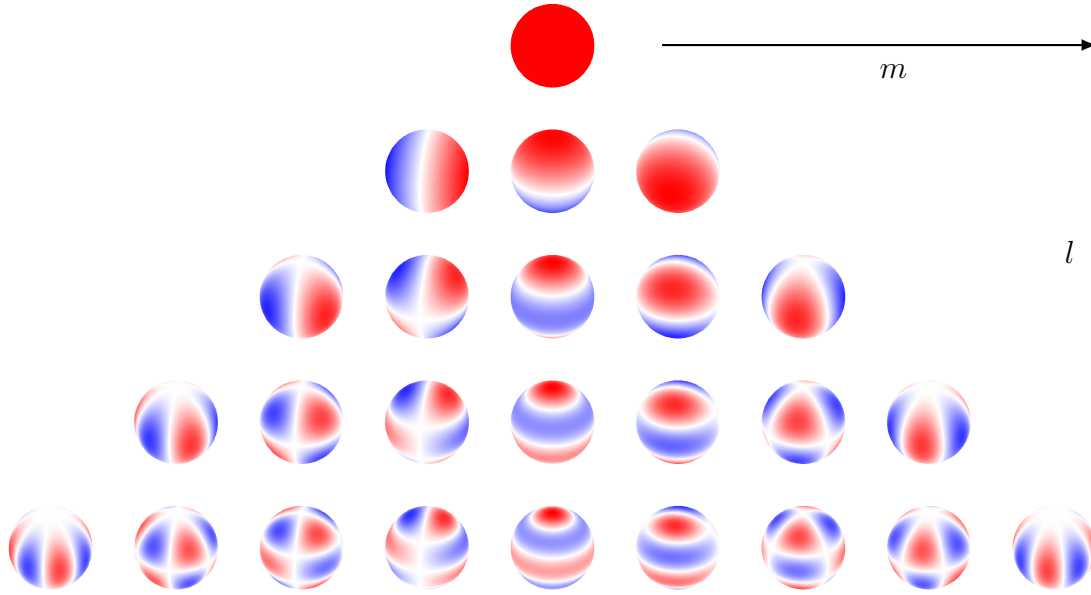
Figure 3.1: The first 25 associated Legendre functions Y_l^m. From top to bottom: $l = 0, \ldots, 4$, from left to right: $m = -l, \ldots, l$. The color coding changes from red ($Y_l^m = +1$) over white ($Y_l^m = 0$) to blue ($Y_l^m = -1$).

with $\cos(m\varphi)$. In this nomenclature, the spherical harmonics Y_l^m (SH) are normalised on the unit sphere Ω by

$$\int_{\theta=0}^{\pi} \int_{\varphi=0}^{2\pi} Y_l^m Y_{l'}^{m'*} d\Omega = \frac{4\pi}{(2l+1)} \delta_{ll'} \, \delta_{mm'} \,. \tag{3.8}$$

Figure 3.1 shows the first 25 spherical harmonics for l between 0 and 4. It is easy to identify the relation between the number of nodal lines and the degree l and order m: Y_l^m is equal to 0 along m great circles passing through the poles, and along $l - m$ circles of equal latitude. Degree l and order m are thus a measure for the wavelength.

Some of the base functions show special characteristics and are named individually:

- **Zonal** functions have vanishing m ($m = 0$) and are independent of longitude φ (centre row in Fig. 3.1).

- For $l = |m|$, there are no zero crossings in latitude, and the functions are referred to as **sectoral** (left and right outer border in Fig. 3.1).

- All other cases are called **tesseral** and the functions vary with both latitude and longitude.

In honour of Carl Friedrich Gauss, the coefficients g_l^m and h_l^m in the harmonic expansion are called *Gauss coefficients*. Following Eq. (3.6), the magnetic potential V and accordingly the magnetic field are described by an expansion from zero to infinity. The term for $l = 0$ corresponds to a magnetic monopole and violates Eq. (3.1). Therefore, it is always

omitted in the analysis of geomagnetic fields. In practice, it is also impossible to compute an infinite number of coefficients, so the series is truncated at an upper boundary $l = L$. With omitted $l = 0$, this requires $L(L+2)$ coefficients to be evaluated if only the internal contribution is considered.

For the radial contributions, we use the factor $R_E = 6371.2\,\text{km}$ as the radius of the Earth. By this scaling, the Gauss coefficients have the same dimension as $\mathbf{B}$. Eq. (3.6) contains two different expansions for the radial contributions. Both satisfy the radial differential equation but show different behaviour: As r approaches zero, $(R_E/r)^{l+1}$ grows infinitely large and thus describes sources from inside of $r = R_E$. Terms in $(r/R_E)^l$ vanish with decreasing r and describe sources from outside $r = R_E$. The field components $\mathbf{B} = (B_r, B_\vartheta, B_\varphi)$ are obtained as derivatives:

$$
B_r = -\frac{\partial V}{\partial r} = \sum_{l=1}^{\infty}\sum_{m=0}^{l}\left(\frac{R_E}{r}\right)^{l+2}(l+1)(g_l^m \cos m\varphi + v_l^m \sin m\varphi)P_l^m(\cos\vartheta)
$$

$$
B_\vartheta = -\frac{1}{r}\frac{\partial V}{\partial \vartheta} = \sum_{l=1}^{\infty}\sum_{m=0}^{l}\left(\frac{R_E}{r}\right)^{l+2}(g_l^m \cos m\varphi + h_l^m \sin m\varphi)\frac{\mathrm{d}P_l^m(\cos\vartheta)}{\mathrm{d}\vartheta}
$$

$$
B_\varphi = -\frac{1}{r\sin\vartheta}\frac{\partial V}{\partial \varphi} = \sum_{l=1}^{\infty}\sum_{m=0}^{l}\left(\frac{R_E}{r}\right)^{l+2}(g_l^m \sin m\varphi - h_l^m \cos m\varphi)\frac{mP_l^m(\cos\vartheta)}{\sin\vartheta}
$$

Note that the measured components, usually directed towards North, East and down (X, Y, Z), are related to $(B_r, B_\vartheta, B_\varphi)$ by

$$
\begin{aligned}
X &= -B_\vartheta & (3.9)\\
Y &= B_\varphi & (3.10)\\
Z &= -B_r & (3.11)
\end{aligned}
$$

The analysis of the Gauss coefficients reveals already insights into the sources of the geomagnetic field. Following Mauersberger (1956) and Lowes (1966), the mean square value of the field over the surface of the Earth produced by harmonics of a given l is given by

$$
R_l = (l+1)\sum_{m=0}^{l}(g_l^m)^2 + (h_l^m)^2\,. \tag{3.12}
$$

In section 3.1.3, that deals with popular global models, we see an example of how the variation of R_l depends on l in a so-called *power* or *Mauersberger-Lowes spectrum*.

3.1.2 Temporal description

The description in terms of spherical harmonics with constant Gauss coefficients is applicable for static "snapshot" fields. However, since the magnetic field changes in space *and*

time, all modern field models use time-dependent Gauss coefficients $g_l^m(t)$. The commonly adopted approach is to model the temporal evolution with spline functions.

The term "spline" and its concept comes from the naval architecture, where it is used as a drawing tool. A long thin wooden lath fixed at specific points by nails or weights tends to minimise its internal tension and adopts a smooth shape without sudden changes in the radius of curvature. Mathematically speaking, a spline is a function defined by piecewise polynomials. In the simplest case, these are straight lines joined at several *nodal points* or *knots*. For higher flexibility, polynomials of higher degree can be used. In case of cubic polynomials, the function shows the same shape as the drawing tool.

In the following paragraph, I briefly review the theory of B(asis)-splines that was developed by de Boor (2001). If $t_i, i = 1, \ldots, m$ are a set of strictly increasing real numbers, and if $s(t)$ is a polynomial of degree $n - 1$ or less in each of the intervals

$$t \leq t_1 \; ; \; t_{i-1} \leq t \leq t_i, i = 1, \ldots, m \; ; \; t_m \leq t; \tag{3.13}$$

and if $s(t)$ and its derivatives up to order $n - 2$ are continuous, then $s(t)$ is a spline function of order n or degree $n - 1$ with knots at $\{t_i\}$. The B-spline of degree $n - 1$ with knots at $t_{i-n}, t_{i-n+1}, \ldots, t_i$ is defined by

$$M_{ni}(t) = \sum_{k=i-n}^{i} \frac{(t_k - t)_+^{n-1}}{W'_{ni}(t_k)} \, , \tag{3.14}$$

where the function t_+^{n-1} is a polynomial of degree $n - 1$ for positive and zero arguments and zero for negative arguments:

$$t_+^{n-1} = \begin{cases} t^{n-1} & \text{for} \quad t \geq 0 \\ 0 & \text{for} \quad t < 0 \end{cases} \tag{3.15}$$

The derivative W'_{ni} is given by

$$W'_{ni} = \frac{d}{dt}[W_{ni}] = \frac{d}{dt}[(t - t_{i-n})(t - t_{i-n+1}) \ldots (t - t_i)]. \tag{3.16}$$

M_{ni} is zero for $t \geq t_i$ and for $t \leq t_{i-n}$ and is strictly positive for $t_{i-n} < t < t_i$. B-splines are piecewise linear for $n = 2$, piecewise quadratic for $n = 3$, cubic for $n = 4$, and so forth. To fit data with order n B-splines in the range t_l to t_h, a set of knots $\{t_i, i = 1, \ldots, m\}$ has to be defined in the interval (t_l, t_h) and $2n$ additional knots have to be introduced such that

$$t_{-n+1} \leq t_{-n+2} \leq \ldots \leq t_0 \leq t_l \text{ and } t_h \leq t_{m+1} \leq \ldots t_{m+n-1} \leq t_{m+n} \, . \tag{3.17}$$

The general order n B-spline over $[t_l, t_h]$ is then given by

$$s(t) = \sum_{i=1}^{m+n} c_i M_{ni}(t) \, , \tag{3.18}$$

or in the case of Gauss coefficients

$$g_l^m(t) = \sum_{i=1}^{m+n} a_{l,i}^m M_{ni}(t) \tag{3.19}$$

In main field modelling, the choice of the order n limits the describable field changes: if cubic B-splines are used for the expansion of the Gauss coefficients, the secular acceleration, as the second derivative, is just linear between the spline knots and it reaches its maximum at the knots.

The use of B-splines for the temporal description of geomagnetic field features several advantages: as the basis functions are non-zero only on discrete adjoining intervals, they can easily map localised features like temporal discontinuities. Furthermore, the spline function has the smallest curvature among all twice continuously differentiable functions that satisfy the interpolation condition.

All main field models presented in the following section use B-splines for temporal modelling, even though they are piecewise linear only in the case of the IGRF.

3.1.3   Example models

First used by Gauss in 1838, the spherical harmonics are widely employed to describe the magnetic field as derivative of a potential in a spherical coordinate system until today. Relying on intensity, declination and inclination data, Gauss was already able to derive harmonic coefficients through degree and order four, considering only internal contributions. Subsequently, geomagnetic models were published going to higher degree and order. Until the mid-20th century, magnetic field models with $L = 6$ were calculated and until now, L is still increasing with improving computer capability and data availability.

Making use of the spline approach for temporal description, scientists world-wide derive global magnetic field models. During the last ten years, the decade of the geopotential research, several satellites provided highly accurate magnetic measurements with a global coverage (cf. 2.4.2). Together with the observatory network, those data serve as input for the recent field models, the most important of which are summarised here.

IGRF

The *International Geomagnetic Reference Field* IGRF is an internationally agreed series of global SH models of the Earth's magnetic field whose sources are mainly in the Earth's core. It is provided by the IAGA Division V-MOD. The Gauss coefficients are considered linearly time dependent for five-year intervals and calculated as a weighted average of several candidate models submitted to IAGA.

The first generation of IGRF was available in 1969. Every five years, international teams are called to provide main-field candidate models through SH degree and order 13 for a given date, a so called *epoch*, e.g. for 2010.0 in the current 11th generation. Additionally, a predictive linear secular variation has to be given to degree 8 for the subsequent five
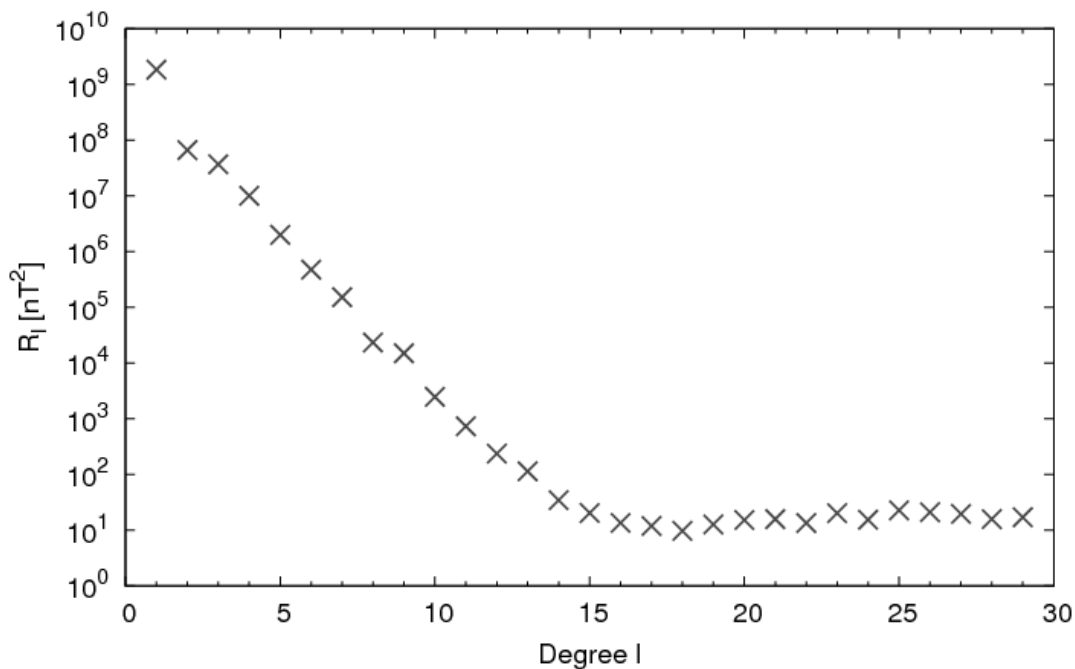
Figure 3.2: Power spectrum of the CM4 model for 1990. For more explanation see text below.

years (Finlay et al., 2010). All contributing teams have access to the same data base, so that the main differences in the submitted models come from either the data selection algorithms or applied ionospheric, plasma or tidal corrections.

With the announcement of a new IGRF, its precedessor is reprocessed with an improved data set that was not yet available at the time of production. The modified previous model is called the Definitive Geomagnetic Reference Field (DGRF) and a series of DGRFs is available in five-year intervals since 1945.

Due to the very simple model of constant secular variation in the five-year intervals, the model is not appropriate for long term studies of the field behaviour. Nonetheless, it is widely used for field prediction also beyond the geomagnetic community, also thanks to the published source codes and online calculators (for series of Gauss coefficients see IGRF homepage [1]).

CM4

The fourth version of the *Comprehensive Model* was developed by Sabaka et al. (2004). This model relies on POGO, MAGSAT, Ørstedt and CHAMP satellite data and observatory hourly means and is continuous through the time span from 1960 to 2002.5. The spherical harmonic expansion goes to degree and order 65 with SV represented by cubic B-splines with 2.5-years knot spacing through degree and order 13. The *comprehensive* approach of this model is its sophisticated parametrisation of external sources: not only

---

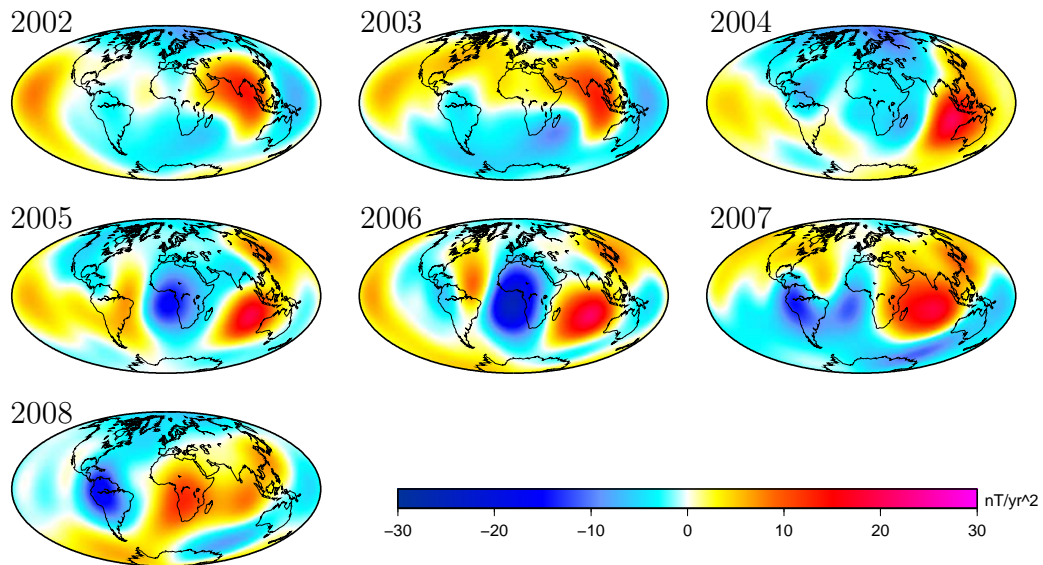[1] www.ngdc.noaa.gov/IAGA/vmod/IGRF-10

Figure 3.3: A sequence of the secular acceleration (z-component) derived from GRIMM-2 model at the Earth's surface.

the internal core and crustal contributions are modelled, but, at the same time, ionospheric and magnetospheric sources dependent on seasonal effects and solar activity, and their induced counterparts are included. Altogether, 25243 parameters are necessary to describe the geomagnetic field in such detail.

For the CM4 model, Fig. 3.2 shows the measure of energy per degree (R_l in eq. 3.12) over the degree in a so-called "power spectrum". A clear break is visible around spherical harmonic degree 13. This break, common to all SH descriptions of the Earth's magnetic field, represents the change from dynamic core processes to quasi-static lithospheric ones.

GRIMM

Lesur et al. (2008) derived the *GFZ Reference Internal Magnetic Model* (GRIMM) and its successor GRIMM-2 (Lesur et al., 2010) from CHAMP satellite data and observatory hourly means. GRIMM-2[2] covers the years 2000.0 to 2010.0. Its special characteristic is the use of full vector satellite data at high latitudes at all local times. Like that, GRIMM attempts to separate fields into the contributions generated by the ionosphere and field aligned currents on one hand, and, on the other hand, the contributions generated in the Earth's core and lithosphere. With this selection technique data gaps during the polar summers are avoided and the modelling of the core field can be achieved with high time resolution. Order six B-splines with 0.5 years knot separation are used to model the core field up to degree 16. This leads to a quadratic behaviour of the secular acceleration and prevents abrupt changes at the time knots. Figure 3.1.3 shows the time evolution of the secular acceleration at the Earth's surface derived from GRIMM-2.

---

[2]`http://www.gfz-potsdam.de/portal/gfz/Struktur/Departments/Department+2/sec23/`
`topics/models/GRIMM2`

Despite the high order in the time representation, GRIMM-2, as well as other comparable up-to-date global field models, fail to fit the SV calculated from observatory monthly means. More insights in this problem are given in chapter 5.

CHAOS

Comparable to the GRIMM series are the CHAOS models derived by Olsen et al. (2006, 2009). Also based on satellite and observatory data, Olsen et al. (2009) pay special attention to variations on subdecadal time scales in their CHAOS-2s model. The authors consider those variations as of internal origin and conclude the occurrence of at least two jerks during the last decade. Again, I describe this problem in more detail and give a possible solution in chapter 5.

MF6

Provided by Maus et al. (2008), the MF6 model is an example for lithospheric field modelling. Using four years (2004-2007) of readings from the CHAMP fluxgate magnetometer, MF6 estimates the lithospheric magnetic field to spherical harmonic degree 120 which corresponds to 333 km wavelength resolution. Thereby, MF6 even resolves the direction of oceanic magnetic lineaments.

Many more global field models based on different data types (ground based, satellite, paleomagnetic) considering several field sources and covering different time periods (archeomagnetic to recent time) are derived by researchers. On the internet, some institutions provide their models together with online calculators or source codes. Those codes are convenient for generating *synthetic data*: If one is interested in field values that are not contaminated by any errors and obey Eq. (3.6), "clean data" can be obtained by evaluating these field models. The GFZ German Research Centre for Geosciences[3] or the National Oceanic and Atmospheric Administration NOAA[4] offer a good overview on the great number of field models together with user-friendly calculators.

3.2   Regional field models

Chapter 2 showed that observatories, satellites and repeat stations offer different data distributions with different quality. While the previously described field models lean on the worldwide network of observatories and on the global coverage of satellite data, repeat station surveys provide more dense but still very accurate data sets. As already mentioned, such surveys are primarily carried out to obtain small scale, better resolved regional magnetic field maps. To extract regional models and maps from discrete, regionally distributed data, several techniques exist. Haines (1990) and more recently Schott and

---

[3]http://www.gfz-potsdam.de/portal/gfz/Struktur/Departments/Department+2/sec23/topics/models
[4]http://geomag.org/

Thébault (2010) give a detailed overview of various regional modelling approaches, several of which are outlined below.

3.2.1 Polynomial fits

Assuming that the area is so small that the curvature of the Earth can be neglected, a simple model can be derived using a surface polynomial. Each component, or its associated time derivative, is modelled as spatial polynomial in latitude ϑ and longitude φ, here exemplary given for the North component:

$$
\begin{aligned}
E(\vartheta, \varphi_0) = a &+ b(\vartheta - \vartheta_0)^3 + c(\varphi - \varphi_0)(\vartheta - \vartheta_0)^2 + d(\varphi - \varphi_0)^2(\vartheta - \vartheta_0) \\
&+ f(\vartheta - \vartheta_0)^2 + g(\varphi - \varphi_0)(\vartheta - \vartheta_0) + h(\varphi - \varphi_0)^2 \\
&+ i(\varphi - \varphi_0) + j(\vartheta - \vartheta_0)
\end{aligned} \tag{3.20}
$$

with (ϑ_0, φ_0) being the centre of the area of interest. Data from different measurement epochs can be included using time-dependent coefficients $a(t), b(t), \ldots, i(t)$ described e.g. by B-splines. Polynomial models are suitable for technical use (e.g. to obtain declination maps for navigation), but do not allow a deeper understanding of the physical processes which drive the observed spatial and temporal changes. Furthermore, it is not possible to include different data types like ground-based, airborne, or satellite measurements.

3.2.2 Spherical Cap Harmonic Analysis

The solution of Laplace's equation on a spherical cap rather than on the entire sphere, the so-called *Spherical Cap Harmonic Analysis* (SCHA), was developed by Haines (1985) for modelling MAGSAT data over Canada. Hence, SCHA permits the use of data from only a portion of the Earth while satisfying the constraints of potential field theory. As the bounding conditions are periodic along the cap border but not necessarily orthogonal to it, the solution involves associated Legendre functions of integral order l as in classical SH analysis but - remarkably - non-integral degree k. The base functions comprise two infinite sets, within each of which the functions are mutually orthogonal. However, orthogonality is not given for functions of both sets.

As Haines (1988) also provided source codes, the method was often applied for the construction of regional models, see for example Nevanlinna et al. (1988), DeSantis et al. (1997), Korte (1999), Kotzé (2001) or Toh et al. (2007).

Although widely used in geomagnetism, the SCHA technique suffers several drawbacks. Because the base functions are not completely orthogonal, determination of model coefficients becomes difficult: coefficients can be rejected because of statistical insignificance (as proposed by Haines), or because of physical arguments (Korte and Holme, 2003). Moreover, Thébault et al. (2004) have stressed that the exact upward continuation can be incorporated properly only if a 3-D boundary value problem is solved, and more refined versions had to be developed (Thébault and Gaya-Piqué, 2008, Thébault, 2008).

3.2.3   Wavelet Analysis

During the last few years, several authors (Holschneider et al., 2003, Chambodut et al., 2005) proposed to use wavelet frames for constructing regional potential field models. Unlike the base functions, the elements of one frame are not necessary linearly independent. An example of implementation of the wavelet representation for potential fields is the work done by Panet et al. (2006). The authors apply the wavelet method to refine a global, "low"-resolution gravity field with local, high-resolution data, leading to a combined gravity field in French Polynesia. For the same area, a crustal magnetic field model based on CHAMP satellite data only was obtained using the same approach.

The forthcoming chapters make use of a further, different approach of geomagnetic field modelling, namely the harmonic splines. Hence, I devote a separate section to the derivation of this method which can be applied either globally or regionally.

3.3   Harmonic Splines

The *harmonic splines* were first introduced by Shure et al. (1982) and used mainly for global modelling (cf. e.g. Whaler, 1994, Shure et al., 1985). Highlighting localised constraints connected with local base functions, Lesur (2006) describes a representation close to the method used here. This section summarises the basics of the method while stressing the main differences in the presented approach that is applied in the forthcoming chapters.

We consider a functional ϕ as the integral of the square of the second derivative of the radial component of the magnetic field over a sphere Ω defined by a reference radius a:

$$\phi = \int_\Omega |\nabla_h^2 B_r|^2 d\Omega \,, \tag{3.21}$$

where the horizontal derivative $\nabla_h = \nabla - \partial_r/r$ affects only the angular dependencies. As the second derivative corresponds to the curvature of a function, the functional ϕ can be regarded as a measure of smoothness. Minimizing ϕ leads hence to a radial magnetic field that varies only sparsely on the reference sphere.
Following the classical notation, we express the radial field component as

$$B_r = \sum_{l,m}^L (l+1) g_l^m \left(\frac{a}{r}\right)^{l+2} Y_l^m(\vartheta, \varphi) \,, \tag{3.22}$$

where $\sum_{l,m}^L$ denotes the double sum over l and m and the g_l^m are the Gauss coefficients. The orthogonality relation of the spherical harmonics Y_l^m over the unit sphere Ω can be written as

$$\int_\Omega Y_l^m Y_{l'}^{m'} d\omega = \frac{4\pi}{2l+1} \delta_{mm'} \delta_{ll'} \,, \tag{3.23}$$

where $\delta_{ll'}$ is the Kronecker delta that equals 1 if $l = l'$ and zero else. The horizontal derivative of a spherical harmonic is given by

$$\nabla_h^2 Y_l^m = -l(l+1)Y_l^m \, . \tag{3.24}$$

The integral in Eq. (3.21) then reduces to

$$\phi = \sum_{l,m}^{L} (l+1)^4 \, l^2 \, \frac{4\pi}{2l+1}(g_l^m)^2 \, . \tag{3.25}$$

This integral may be expressed as a scalar product:

$$< \mathbf{a}, \mathbf{b} > = \sum_{l,m}^{L} 4\pi \frac{l^2(l+1)^4}{2l+1} a_l^m b_l^m . \tag{3.26}$$

We now consider a data set made of N measurements of the radial component of the magnetic field at given points $(\vartheta_i, \varphi_i, r_i)$, $i = 1, 2, \ldots, N$. We write each of these values as a scalar product of the form (3.26).

$$B_r(\vartheta_i, \varphi_i, r_i) = \sum_{l,m}^{L} (l+1)\left(\frac{a}{r_i}\right)^{l+2} Y_l^m(\vartheta_i, \varphi_i)g_l^m \tag{3.27}$$

$$= \sum_{l,m}^{L} 4\pi \frac{(l+1)^4 l^2}{2l+1} \, k_{li}^m \, g_l^m \tag{3.28}$$

$$= \; < \mathbf{k_i}, \mathbf{g} > \tag{3.29}$$

where $\mathbf{k_i} = [\, k_{li}^m \,]_{\{l,m\}}$ and $\mathbf{g} = [\, g_l^m \,]_{\{l,m\}}$. The vector components k_{li}^m are defined by:

$$k_{li}^m = \frac{2l+1}{4\pi(l+1)^3 l^2} \left(\frac{a}{r_i}\right)^{l+2} Y_l^m(\vartheta_i, \varphi_i). \tag{3.30}$$

The vectors $\mathbf{g}$ can be written as a linear combination of the vectors $\mathbf{k_i}$:

$$\mathbf{g} = \sum_{j=1}^{N} \alpha_j^r \mathbf{k_j}. \tag{3.31}$$

Thus, Eq. (3.29) can be written for all N data values and using Eq. (3.31) leads to the linear system:

$$[B_r(\vartheta_i, \varphi_i, r_i)]_{\{i\}} = \mathbf{\Gamma} \cdot \alpha^{\mathbf{r}} \tag{3.32}$$

where $\alpha^{\mathbf{r}} = [\, \alpha_j^r \,]_{\{j\}}$ and the matrix $\mathbf{\Gamma}$ is defined by:

$$\Gamma_{ij} = \sum_{l,m}^{L} 4\pi \frac{(l+1)^4 l^2}{2l+1} k_{li}^m k_{lj}^m . \tag{3.33}$$

Once the $\alpha^{\mathbf{r}}$ vector is known, magnetic field values can be computed at any point (ϑ, φ, r) by:

$$
\begin{aligned}
\mathbf{B}(\vartheta, \varphi, r) &= -\nabla a \sum_{l,m}^{L} g_l^m \left(\frac{a}{r}\right)^{l+1} Y_l^m(\vartheta, \varphi) \\
&= -\nabla a \sum_{l,m}^{L} \left\{ \sum_j k_{lj}^m \alpha_j^r \right\} \left(\frac{a}{r}\right)^{l+1} Y_l^m(\vartheta, \varphi) \\
&= -\nabla \sum_j \alpha_j^r \left\{ a \sum_{l,m}^{L} \frac{2l+1}{4\pi l^2 (l+1)^3} \times \right. \\
&\qquad \left. \left(\frac{a}{r_j}\right)^{l+2} Y_l^m(\vartheta_j, \varphi_j) \left(\frac{a}{r}\right)^{l+1} Y_l^m(\vartheta, \varphi) \right\}
\end{aligned}
\tag{3.34}
$$

We rewrite this expression in a compact form:

$$
\mathbf{B}(\vartheta, \varphi, r) = -\sum_j \alpha_j^r \, \nabla F_j^{Lr}(\vartheta, \varphi, r),
\tag{3.35}
$$

where the function $F_j^{Lr}(\vartheta, \varphi, r)$ is defined by:

$$
F_j^{Lr} = a \sum_{l,m}^{L} f_l (l+1) \left[\left(\frac{a}{r_j}\right)^{l+2} Y_l^m(\vartheta_j, \varphi_j) \right] \left(\frac{a}{r}\right)^{l+1} Y_l^m(\vartheta, \varphi),
\tag{3.36}
$$

with $f_l = \frac{2l+1}{4\pi(l+1)^4 l^2}$. The benefit and special characteristic of the derived coefficient f_l is that the obtained field model minimises the functional ϕ introduced in Eq. (3.21) and hence is a smooth field model.

The functions F_j^{Lr} are defined at the measurement positions $(\vartheta_j, \varphi_j, r_j, j = 1, ..., N)$ and are interpolatory (Parker, 1977), i.e. they allow an exact fit to the radial component data, as long as the data contain SH degree lower or equal L.

This method is equivalent to the harmonic spline method presented in Shure et al. (1982). The main difference lies in the use of *finite* series to define F_j^{Lr}. Working with truncated series, i.e. choosing a maximum L allows the results to be comparable to global field models, that are also made of spherical harmonics.

3.3.1 Derivation of additional base functions

The magnetic field model defined in Eq. (3.35) might not fit the tangential components of the magnetic field at the points $(\vartheta_i, \varphi_i, r_i)$, $i = 1, 2, \ldots, N$. To include them in the model derivation, we introduce two further series of functions, similar to F_j^{Lr} in Eq. (3.36):

$$
F_j^{L\vartheta}(\vartheta, \varphi, r) = a \sum_{l,m}^{L} f_l \left(\frac{a}{r_j}\right)^{l+2} \partial_\vartheta Y_l^m(\vartheta_j, \varphi_j) \times \left(\frac{a}{r}\right)^{l+1} Y_l^m(\vartheta, \varphi)
\tag{3.37}
$$

and $\quad F_j^{L\varphi}(\vartheta, \varphi, r) = a \sum_{l,m}^{L} f_l \left(\frac{a}{r_j}\right)^{l+2} \frac{\partial_\varphi}{\sin \vartheta_j} Y_l^m(\vartheta_j, \varphi_j) \times \left(\frac{a}{r}\right)^{l+1} Y_l^m(\vartheta, \varphi).$ $\quad$ (3.38)

The derivations of $F_j^{L\vartheta}$ and $F_j^{L\varphi}$ are given in appendix A.

With these additional base functions, the magnetic field can be written as

$$\mathbf{B}(\vartheta, \varphi, r) = -\nabla \left(\sum_j \alpha_j^r F_j^{Lr}(\vartheta, \varphi, r) + \sum_j \alpha_j^\vartheta F_j^{L\vartheta}(\vartheta, \varphi, r) + \sum_j \alpha_j^\varphi F_j^{L\varphi}(\vartheta, \varphi, r) \right) \quad (3.39)$$

In this representation, and because the functions are defined at the observation locations, we are able to fit three-component data exactly.

Additionally, a time dependency is introduced by expanding each of the coefficients α_j^r on a basis of B-splines, as provided in section 3.1.2

$$\alpha_j^r = \sum_{k=1}^{n_{knots}} \beta_{kj}^r b_k(t) \,, \quad (3.40)$$

where n_k is the number of knots, and similarly for the α_j^φ and α_j^ϑ.

3.3.2   The inverse problem

The harmonic splines are applied in the following chapters 4 and 5 to two regional main field data sets and to a global SV data set. To obtain the respective model parameters, an *inverse problem* needs to be solved. Before assessing the special cases, I review the standard techniques and nomenclature of linear inverse problems.

The starting place of any inverse problem is a description of given data, derived e.g. from measurements. The data can be assembled in a data vector d of length N

$$\mathbf{d}^T = (d_1, d_2, \ldots d_N) \,. \quad (3.41)$$

We describe a model by a set of P parameters assembled in a model vector of length P

$$\mathbf{m}^T = (m_1, m_2, \ldots m_P) \,. \quad (3.42)$$

The basic assumption is that the data depend on the model parameters

$$\mathbf{d} = A(m) \quad (3.43)$$

and, considering a linear relationship, that dependency may be written in the matrix form

$$\mathbf{d} = \mathbf{Am} \quad (3.44)$$

where $\mathbf{A}$ is a $N \times P$ matrix of coefficients that are independent of data and model. In the case of modelling magnetic fields e.g. with spherical harmonics, $\mathbf{A}$ contains P base

functions evaluated at N data positions. $\mathbf{m}$ then comprises the Gauss coefficients and $\mathbf{d}$ the data to be described, e.g. the vertical component of the Earth's magnetic field at those N locations.

If all P lines are included, the conditions equations read

$$d_i = \sum_{j=1}^{P} A_{ij} m_j \,. \tag{3.45}$$

Usually, one has more data available than parameters to be resolved, which means $N > P$. In this case, the above equation cannot be satisfied for every i (assumed that the data are defective). The inverse problem has no exact solution and is *overdetermined*. Hence, model parameters are sought such that eq. 3.44 is solved approximately. The *least squares* method minimises the sum of the squares of the errors and thus to find the "best" approximate solution. The misfit between data and model prediction is

$$e_i = d_i - \sum_{j=1}^{P} A_{ij} m_j \,. \tag{3.46}$$

from where we gain an expression for the the sum of squares of these misfits as

$$E^2 = \sum_{i=1}^{N} e_i^2 = \sum_{i=1}^{N} \left(d_i - \sum_{j=1}^{P} A_{ij} m_j \right)^2 \,. \tag{3.47}$$

We want to obtain the parameter set where E^2 is minimal, so we set $\partial E^2 / \partial m_k = 0$ and obtain

$$2 \sum_{i=1}^{N} \left[d_i - \sum_{j=1}^{P} A_{ij} m_j \right] (-A_{ik}) \;=\; 0 \tag{3.48}$$

$$\rightarrow \sum_{i=1}^{N} \sum_{j=1}^{P} A_{ij} A_{ik} m_j \;=\; \sum_{i=1}^{D} A_{ik} d_i \,. \tag{3.49}$$

Expressed in matrix notation, this equation reads

$$\mathbf{A}^T \mathbf{A} \mathbf{m} = \mathbf{A}^T \mathbf{d} \,. \tag{3.50}$$

Data can be affected by different error sources (see Chapter 2) and these error sources can even be correlated. The *covariance matrix* $\mathbf{C}$ is introduced to account for this correlation. Generally, it is defined for two random variables by

$$\mathbf{C}(X, Y) = \mathcal{E}[(x - \mathcal{E}(x))(y - \mathcal{E}(y))] \,, \tag{3.51}$$

where $\mathcal{E}(x)$ is the expected value of the variable x. For uncorrelated data, the covariance matrix is diagonal. In practice, it is not always easy to define what is the expected value

$\mathcal{E}(x)$, but if chosen properly, the covariance matrix divides each row and datum by its variance:

$$E^2 = (\mathbf{d} - \mathbf{Am})^T \mathbf{C}^{-1} (\mathbf{d} - \mathbf{Am}) \tag{3.52}$$

Inverse problems are usually *ill-posed*: small deviations in the data can lead to considerable changes in the parameters. The error amplification must be mitigated by appropriate measures in the solution process: inverse problems can be regularised by introducing additional summands on the left-hand side of Eq. (3.52).

3.3.3 Implementation

We return to the special case of fitting geomagnetic data with harmonic splines. A linear system $\mathbf{d} = \mathbf{Am}$ is built from equations (3.39) and (3.40). We have to solve for the unknown model parameters β_{kj}^r, β_{kj}^ϑ and β_{kj}^φ as defined in eq. (3.40) and, in case of main field modelling, additionally for crustal offsets at each measurement location. The β_{kj}^r, β_{kj}^ϑ and β_{kj}^φ together with the crustal offsets constitute the parameter vector $\mathbf{m}$. As introduced in the last section, a solution in the least squares sense can be performed by minimising

$$J = (\mathbf{d} - \mathbf{Am})^T \mathbf{C}^{-1} (\mathbf{d} - \mathbf{Am}), \tag{3.53}$$

which we name the functional J.

In the subsequent chapters we want to built models from different data sets. How the elements of the respective covariance matrix are derived is explained in the associated sections 4.3.1, 4.3.2 and 5.3.

To obtain a robust model, regularisation is required. For the regularisation in time we minimise the squared second time derivative of the radial field integrated over the whole sphere Ω and the entire timespan:

$$\int_{t=t_{start}}^{t=t_{end}} \int_\Omega (\partial_t^2 B_r)^2 d\omega dt \tag{3.54}$$

which can be written as

$$\int_{t=t_{start}}^{t=t_{end}} \int_\Omega \left[(\ddot{B}_r^r)^2 + (\ddot{B}_r^\vartheta)^2 + (\ddot{B}_r^\varphi)^2 + 2\ddot{B}_r^r \ddot{B}_r^\vartheta + 2\ddot{B}_r^r \ddot{B}_r^\varphi + 2\ddot{B}_r^\vartheta \ddot{B}_r^\varphi \right] d\omega dt. \tag{3.55}$$

The expressions for the six integrals are given in the appendix A.

For the regularisation in space we minimise the integral over space and time of the squared horizontal divergence of the radial field component:

$$\int_{t=t_{start}}^{t=t_{end}} \int_\Omega |\nabla_h^2 B_r|^2 d\omega dt. \tag{3.56}$$

Accordingly, damping matrices Λ_s and Λ_t are introduced for regularisation in space and time, respectively. Thus, we rewrite Eq. (3.53) as

$$J = (\mathbf{d} - \mathbf{Am})^T \mathbf{C}_e^{-1} (\mathbf{d} - \mathbf{Am}) + \lambda_t \mathbf{m}^T \Lambda_t \mathbf{m} + \lambda_s \mathbf{m}^T \Lambda_s \mathbf{m} \tag{3.57}$$

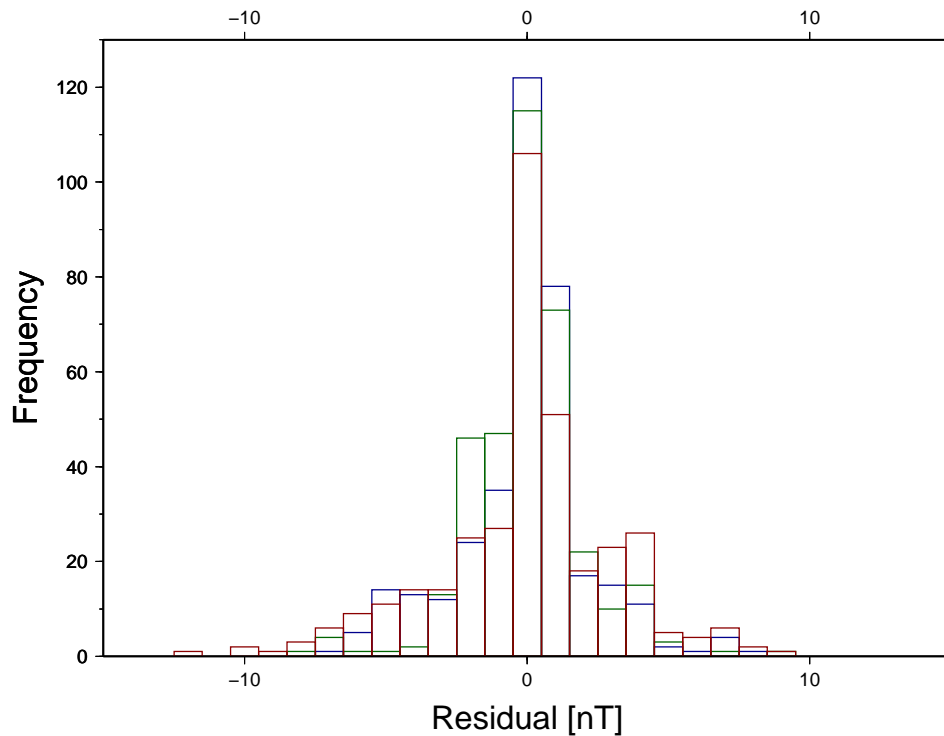The choice of λ_t and λ_s is discussed in the next section.

Figure 3.4: Histogram of errors in fit to CM4 "data". Errors in X, Y and Z are shown in red, green and blue.

3.3.4   Testing the approach with synthetic data

The harmonic spline approach was primary revisited in order to provide a regional field model of the southern African continent. Therefore, a test of the modelling approach is performed using a synthetic data set covering the same time span and data distribution as the real data. The details of the synthetic and real south African data bases are described in chapter 4. In summary, the data set concerns three-component magnetic field data measured yearly at three observatory locations and at 35 repeat stations at 5-year intervals, all in the period 1961-2001. For the temporal parametrisation, a time representation of order six B-splines with 27 spline knots spaced at 2.5 year intervals from 1961.0 to 2001.0 is chosen to follow the field variations closely. To test the sensitivity of the model to the maximum degree, L is changed from 5 to 60 without imposing any damping. The fit to the synthetic data is satisfactory, i.e. with a rms of the order of 0.1 nT, using a maximum degree $L = 20$. This degree is small enough to show mainly contributions from the core, but still large enough to resolve smaller scale features. Global main field models usually use spherical harmonics up to degree and order 14. With the slightly enhanced L we account for the known strong spatial field gradients in this region. Figure 3.4 shows a stacked histogram of the misfit each of the three magnetic components in the synthetic data set. Obviously, the errors are centred at zero and decay rapidly, what is required for a fit to "good" synthetic data.
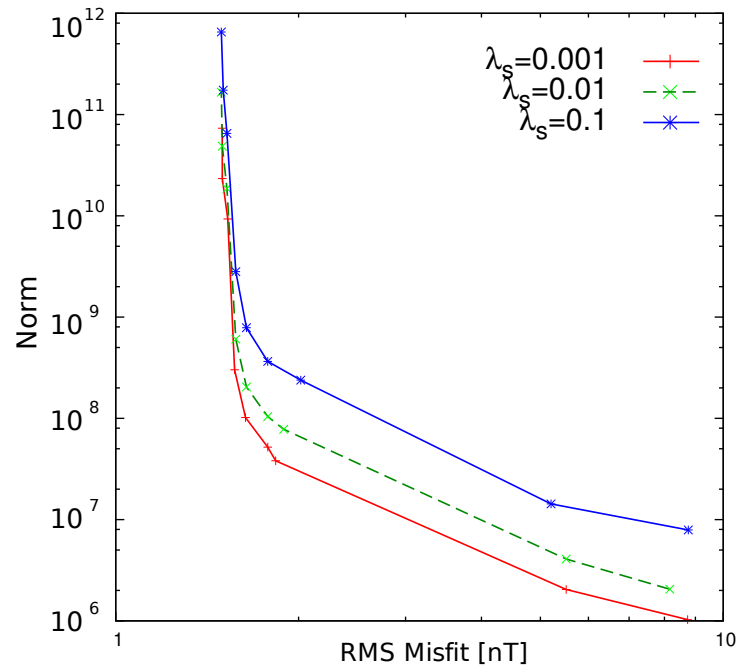
Figure 3.5: Trade-off curves between data misfit and the roughness of the model. The three lines show trade-off curves for three fixed λ_s ($\lambda_s = 0.001$ in red, $\lambda_s = 0.01$ in green and $\lambda_s = 0.1$ in blue) and varying λ_t ($\lambda_t = 1e^{-1}, ..., 1e^{-9}$.) The norm was calculated according to eq. (3.54).

As a next step, the damping parameters λ_s and λ_t are varied systematically and the associated norms calculated following Eqs. (3.54) and (3.56). Fig. 3.5 shows several trade-off curves for three fixed λ_s and varying λ_t. A prominent knee-shape can be observed in all three curves for $\lambda_t = 1 \times 10^{-4}$. The same procedure was done for fixed λ_t and varying λ_s leading to $\lambda_s = 1 \times 10^{-1}$.

In summary, we see that the harmonic splines easily fit the synthetic data set and that the regularization works reasonably. This gives confidence to apply this approach to real data sets in the following sections.

Chapter 4

Regional main field modelling: the South African region

The previous chapters have shown how geomagnetic data are acquired and what mathematical tools are available to describe them. This knowledge is now applied to study the magnetic field regionally. For this purpose, I present a region suitable for intensive studies: the southern African area. After a short introduction that underlines the exceptional features appearing in this region, I first look closer at the magnetic field data available and describe roughly the distinctive features of the field behaviour. The data set is differentiated into two subsets, an ancient and a recent set. In a second step, both sets are compared to global field models in order to obtain estimates about deviations in the data and crustal biases. Finally, two magnetic field models, SAMS and X-SAMS, based on the two data sets are derived using the harmonic splines approach. Both models are the first continuous potential field models over this area and are convenient to study the special features in more detail.

4.1 The South African region: a geomagnetic hotspot

The magnetic field of the Earth is varying with time. Considering the last 30 years, the time span between MAGSAT's first high accurate measurements in 1979 and CHAMP at the end of its lifetime in 2009, the changes are remarkable. The comparison of the m102389 model based on MAGSAT data Cain et al. (1989) for 1979 with the GRIMM-2 model evaluated in 2009 reveals the non-uniformity of these changes: in the southern Atlantic, the field decreased by nearly 10% whereas the Western Indian Ocean undergoes an increase of 4% (cf. Fig. 4.1). Encircled by this two areas lies the southern African region where the field rapid changes can be observed on land. Following Kotzé (2003) and Mandea et al. (2007) this most interesting characteristics in the area covering the Republic of South Africa, Namibia and Botswana are reflected in the strong temporal and spatial gradients. The properties of the magnetic field evolution of the last 70 years are approached by studying the time series of the annual mean values of the three observatories
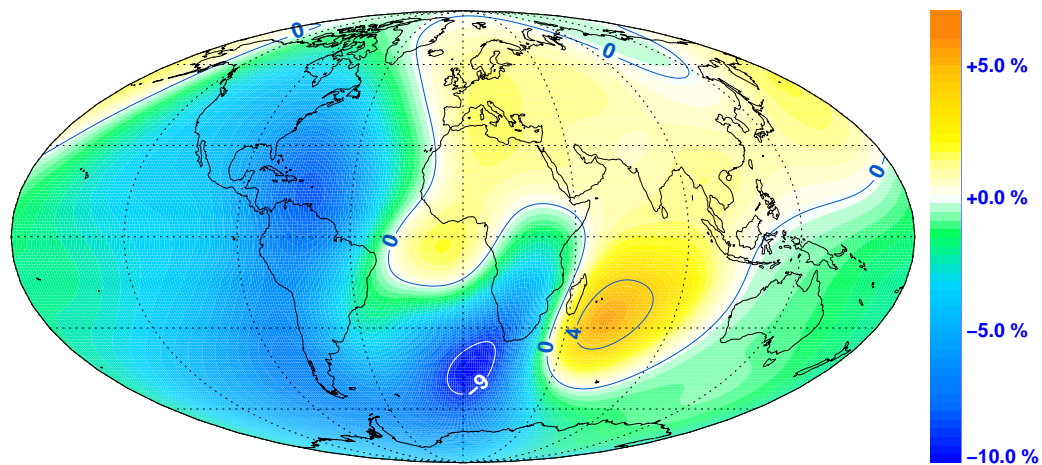
Figure 4.1: Difference in total field between MAGSAT (1989) and CHAMP (2009) epochs.

located in the region of interest (Fig. 1.6). As expected for annual mean values, the graphs change only smoothly. However, the different behaviour of the Y component for Hermanus (HER) in the South and Hartebeesthoek (HBK) in the Eastern part of South Africa on the one hand and for Tsumeb (TSU) on the other hand is obvious: while Y is decreasing for HBK and HER since the end of the last century, TSU features an increasing East component. The Z component stays nearly constant between 1964 and 1980 in TSU and then decreases more rapidly than in the other observatories. Another important feature is the decrease in the field intensity: In Hermanus, F declined more than 20% during the 70 years of measurements. Hartebeesthoek shows the same trend, but with decreasing slope in the last fifteen years.

The origin of this exceptional behaviour is not well understood yet. From field models like GRIMM-2 or CHAOS it is known that the core mantle boundary shows regions where the radial component of the magnetic field, which is usually expected to be directed inward North of the geomagnetic equator and outward South of it, is reversed. One of this revers flux patches is located below the Southern Africa. However, the global models rely exclusively on observatory measurements, although this region additionally houses a very well developed repeat station network that could contribute to a more detailed field description. Kotzé (2003) used this data set to derive regional magnetic field models based on SCHA. Those models were epoch-based only for intervals of five years between 1975 and 2000 and hence did not allow to study the temporal evolution intensively. A more recent polynomial model derived by Kotzé et al. (2007) is also only a snapshot field. The high variability of the South African field together with the great amount of repeat station data and the lack of any continuous regional model qualify this "hot spot" area for an application of the harmonic splines.
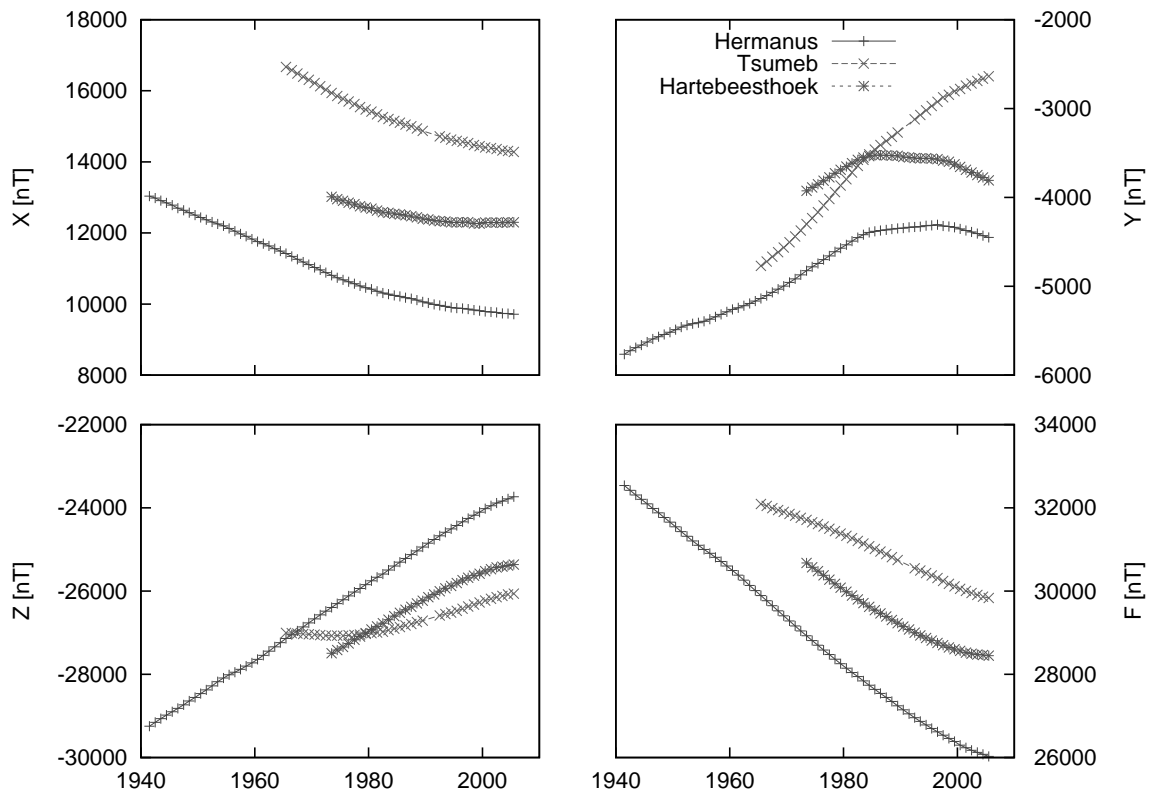
Figure 4.2: Observatory annual mean values for Hermanus, Tsumeb and Hartebeesthoek. The figure shows X (North), Y (East), Z (vertical) component and total intensity F.

4.2 The South African data set

The following section gives an overview over all data available for this study. The data acquisition is discussed, some representative time series are shown, and the noise in the data is estimated.

4.2.1 Data type I: Observatory data

Several observatories are located in the region of interest, namely Hermanus (HER) in the South, Hartebeesthoek (HBK) close to Johannesburg and Tsumeb (TSU) in the North of Namibia. Out of this three, Hermanus Magnetic Observatory is in operation for the longest time span: it officially commenced operation on 1st January 1941. Its location at the southern tip of Africa was chosen after suburban electric railway system was affecting the geomagnetic field observations in Capetown, where the observatory was founded in 1841. The small town of Hermanus is not touched by this problem: Sir William Hoy, General Manager of the South African Railways in the early 1900's ensured that the natural beauty of Hermanus should stay unspoilt by blocking any attempt to extend the railway line to the village. Until today, Hermanus misses any connection to the railroad network
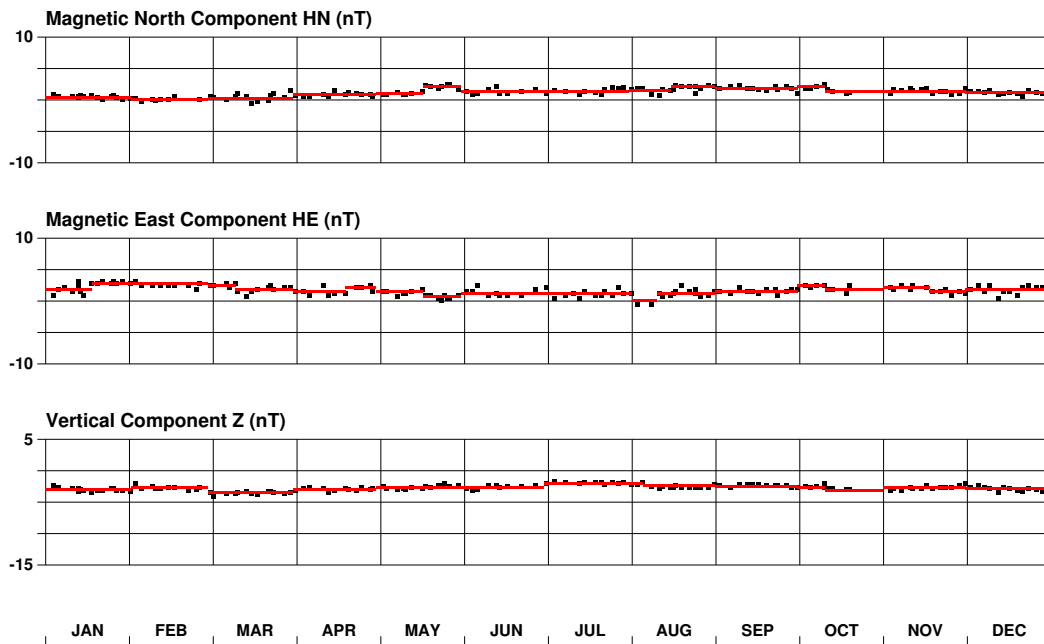
Figure 4.3: Baseline of Hermanus Magnetic Observatory for 2005. Absolute measurements are performed frequently and the observed baseline values do not deviate much, neither from the mean value nor from the adopted baseline. Courtesy: Hermanus Magnetic Observatory.

allowing for undisturbed geomagnetic measurements.

In Hermanus Magnetic Observatory (HMO), the continuous variation measurements are nowadays performed by a type FGE fluxgate manufactured by the Danish Meteorological Institute, complemented by a Geometrics PPM for magnetic intensity. Absolute measurements are normally carried out twice a week. Figure 4.3 shows the HMO baseline for 2005. Baseline adoption is done piece-wise, therfore it shows (slight) jumps. But overall, the baseline looks quite smooth with only low noise. As Hermanus Magnetic Observatory not only takes care of regular geomagnetic measurements but is as well a research facility of the National Research Foundation, about 30 people work in this place. Thus, very well-trained staff is always available to perform regular absolute measurements and to take care of all instruments, ensuring very reliable, high quality data output in this observatory.

During the International Geophysical Year in 1957, the German Max-Planck-Institute for Aeronomy installed a permanent ionospheric observation station outside Tsumeb in Northern Namibia. Six years later, in the frame of the World Magnetic Survey, buildings were set up for housing the geomagnetic observatory instruments, and continuous measurements started on the first of January 1964. Ionospheric research was abandoned by the Max-Planck-Institute in 2001, but the geomagnetic observatory was still maintained by HMO, though from that time on, only laypersons performed the measurements without any scientific infrastructure.
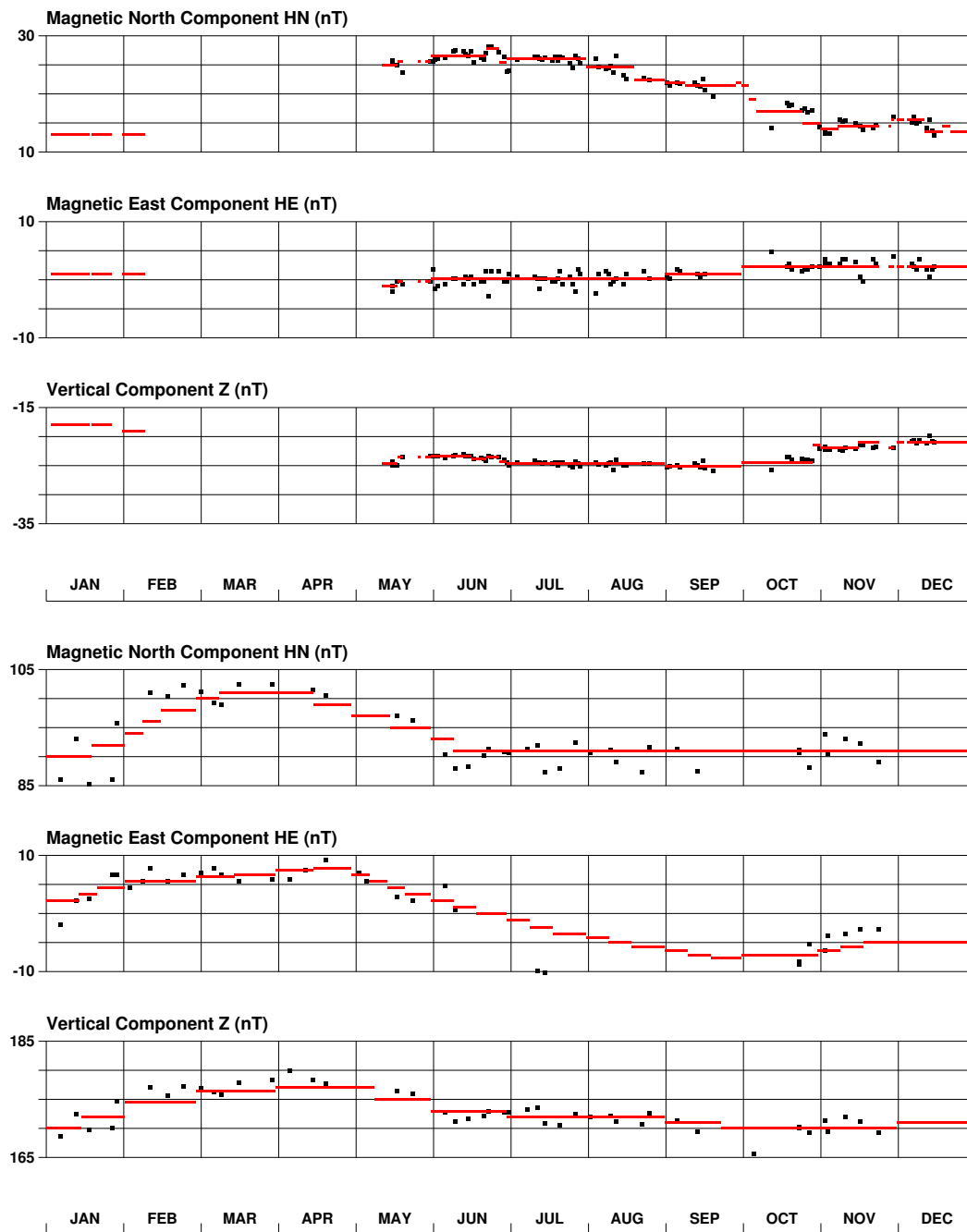
Figure 4.4: Example baselines at Tsumeb (top) and Hartebeesthoek (bottom) magnetic observatories for 2005. More description in the text. Courtesy: Hermanus Magnetic Observatory.

Nowadays, Tsumeb observatory (TSU) is equipped similarly as HMO: a type FGE flux-gate is in charge of the variation recordings, total intensity is measured by a Geometrics PPM, and absolute measurements should be performed once a week with the help of a Zeiss theodolite. An example baseline for the year 2005 (Fig. 4.4 top) shows the drawbacks of this remote observatory: For nearly the first half of 2005, no results are available. From May on, measurements are performed up to twice a week, but the scatter in all components is obvious. While Z stays constant within 5 nT, the North and East components are poorly resolved. X shows a trend decreasing by 15 nT in eight months, the noise in Y is at ± 5 nT.

Hartebeesthoek observatory (HBK), set up in 1972 on the grounds of the South African Radio Astronomy observatory, completes the network since then. The instrumentation is the same as in Tsumeb. Being linked to the Radio Astronomy observatory, the maintenance of the observatory and regular absolute measurements should be more easy to realize. In fact, the 2005 baseline (Fig. 4.4 bottom) shows weekly measurements, however with several gaps (e.g. in September or December). Besides, all components show large drifts, especially in the first half of the year exceeding nearly the ordinate ranges defined by INTERMAGNET.

In a first study, the observatory annual means, taken over all days in a year are used, where noise and drifts in the data are expected to be averaged out partly. Nevertheless, the variance in the data from HBK and TSU is higher than the one in HMO. In chapter 2, I show that an observatory should be accurate down to ± 5 nT according to the INTERMAGNET requirements. For a start, this value is adopted for all observatories for all years.

Altogether, 146 annual mean values are available for these three observatories consisting of 68 data sets from Hermanus (1941.5-2008.5), 36 data sets from Hartebeesthoek (1973.5-2008.5) and 42 data sets from Tsumeb (1965.5-2008.5, with a gap in 1990/91). The time variations of these data are shown in Fig. 4.2. An additional data set offers the use of monthly mean data. Even though they may be still be contaminated by seasonal effects, they allow for a better temporal resolution. Monthly means derived from hourly means are available for HER for the period 1956.0 - 2008.96, for TSU (1964-2008.96) and for HBK (1972-2008.96).

In a cooperation with GFZ Potsdam, another geomagnetic observatory was set up Keetmanshoop in the south of Namibia in 2006 to achieve a better spatial coverage. As data are available for the last two years only, annual mean values of this observatory are not regarded in this study.

A fifth observatory is planned for Botswana to cover the North-East part of this region, and will also be set up with equipment and experience brought in by GFZ.

4.2.2   Data type II: Repeat stations

In 1939, a long-term magnetic secular variation program in southern Africa was instituted. The program consisted initially of 44 permanent field stations covering, with a fairly uniform distribution, the whole of South Africa, Namibia and Botswana. A grid was laid
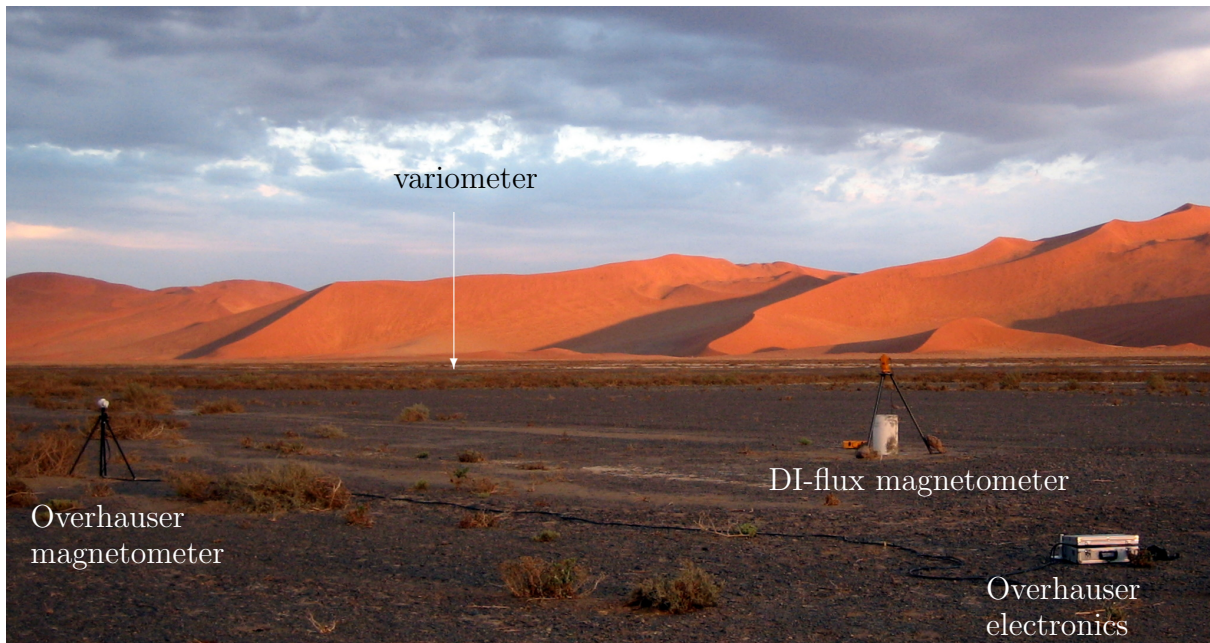
Figure 4.5: Measurement set up at Sossusvley in the Namib desert, East Namibia. The DI Flux-gate magnetometer is set up on concrete pillar (right). In a distance of a few meters, the Overhauser magnetometer is set up (left).

out over the country with ±200 km spacing between points. In most cases the stations were chosen close to towns so as to not be too far away from certain infrastructure. To ensure exact reoccupation during subsequent surveys, concrete beacons were erected at each field station to mark the position of the instruments during observations (cf. section 2.3).

For the first decades, the measurement method is not reported. Since the 1970's a QHM (H), declinometer (D) and a PPM (F) were the standard equipment during any survey. For the period 2001-2004, the DI magnetometer together with a Geometrics PPM replaced the separate Horizontal and Declination measurements for all observations. In this period, measurements were carried out on a yearly basis at a reduced number of eight stations, namely Cradock, Garies, Maun, Messina, Okaukuejo, Severn, Sossusvley, and Underberg, called *super stations*. From 2005 on, a large number of about 40 stations was reoccupied again with an instrumentation completed by an Overhauser Magnetometer and a LEMI-008 magnetometer as on-site variometer. Figure 4.5 shows as an example the station at Sossusvley in the Namib desert in East Namibia, last visited in 2009. Clearly visible are the DI-flux and the PPM in some metres distance. The LEMI variometer is buried underneath the bushes.

Originally, the surveys were conducted as a sort of ground vector measurements (cf. 2.3). Thus, the station positions changed frequently over the years, stations were given up and ones were new installed. 124 different station positions are reported in the time between 1948 and 2004.5, leading to 633 single measurements. Only about half of the stations (i.e.
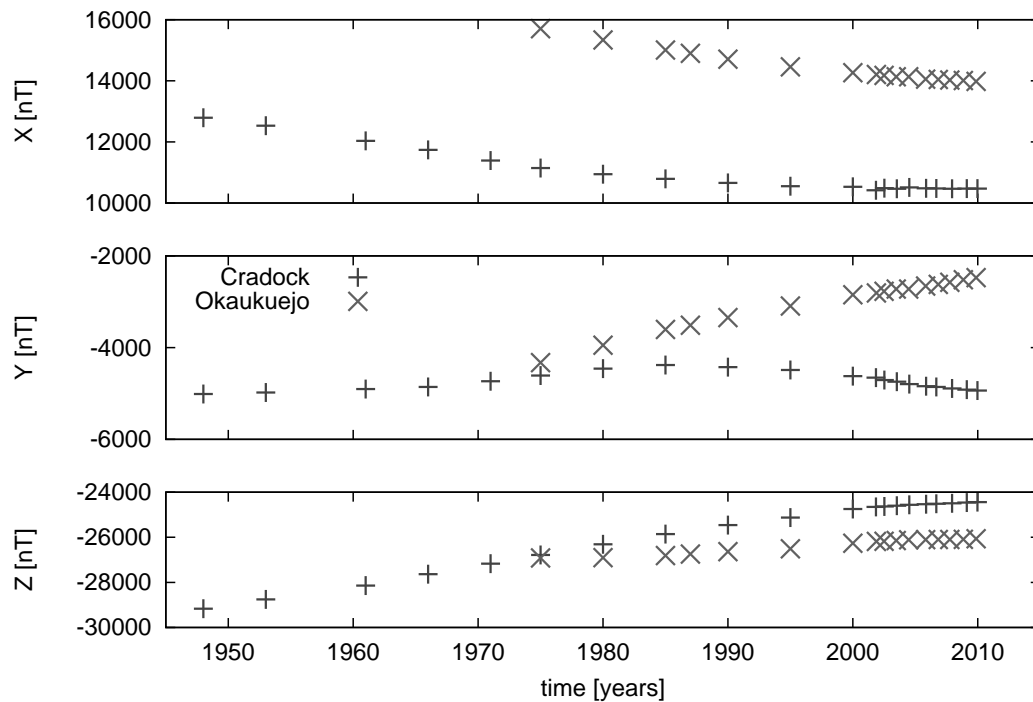
Figure 4.6: Example of measurements in Cradock and Okaukuejo: In Cradock, the pillar was exactly reoccupied 15 times, in Okaukuejo 9 times, covering 50 years and 30 years respectively.

60) were occupied more than four times (234 observations reported).

As usual for magnetic field data, all measurements are reduced to the middle of the year with the help of the closest geomagnetic observatory. For our region of interest, this standard data processing is problematic: The magnetic field gradient over the Southern African continent is so strong, that this kind of data reduction can possibly introduce errors. Data prior to 2002 are only available in this preprocessed form. From 2002 on, the unprocessed data is also available so that the real date of the measurement can be considered, without any reduction applied. As for the observatories, all repeat station data were first checked visually by inspecting the single time series in order to detect obvious jumps or spikes. The time series of two frequently visited sample stations, Cradock and Okaukuejo, being located in the South and in the North West of the area of interest respectively, are shown in Fig. 4.6. As for the observatories, different trends can be detected for the Y component: increasing in Okaukuejo, decreasing for Cradock. For both stations, the frequency of visits is higher in this century (once per year) than it was in the last one, where the time span between two subsequent visit was five years, on average.

The further investigation of the data is twofold, separated by their date of measurement: I set up an *ancient* data set first, which consists of repeat station data collected between 1960 and 2000 and observatory annual mean data, provided by the BGS [1]. A *recent* data

---

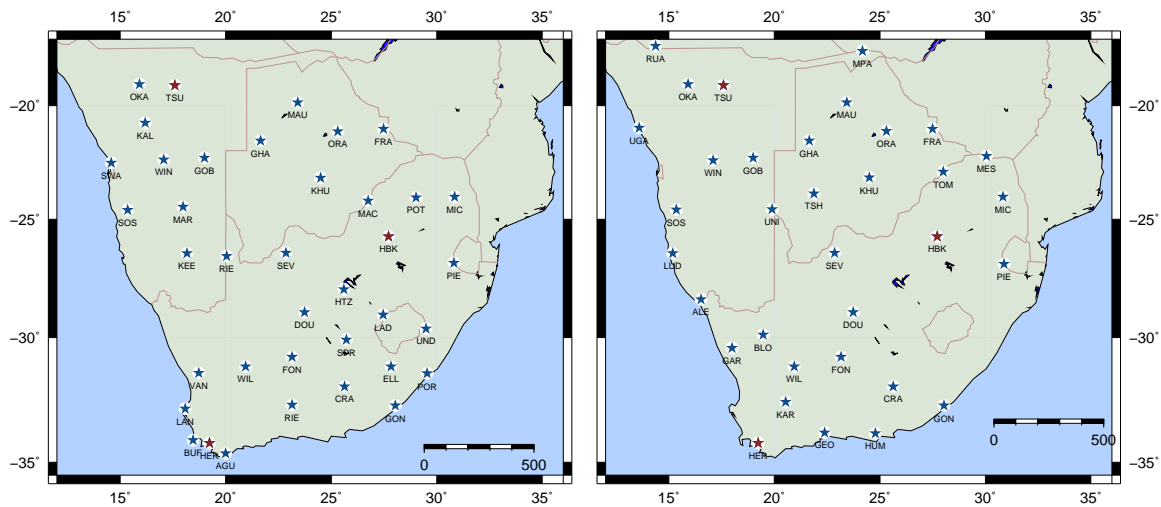[1]http://www.geomag.bgs.ac.uk/gifs/annual_means.shtml

Figure 4.7: Location of stations (blue) and observatories (red) incorporated in the ancient (left) and recent data set.

set is made of repeat station data from 2005.47 and 2009.97 and monthly mean data (I. Wardinski, personal communication).

The ancient data set

From the overall 114 stations, several were only visited once or twice. To be sure to work with reliable time series, only stations that were reoccupied at least eight times between 1961 and 2001 were picked up. An exception was made for the repeat stations in Botswana: Although none of them was visited more than five times, their data are included for reasons of spatial coverage. The remaining data set consists of 35 repeat stations and the three observatories. Their location can be seen in Fig. 4.7, the geographical positions of all stations are listed in table B in the Appendix.

The recent data set

The data characteristics changed remarkably during the last decade. At the beginning of the millennium, 10 "super stations" are selected. The idea was to visit less stations more frequently, namely at an annual basis. The measurements at these stations were carried out with improved measurement accuracy due to the use of the DI-flux method combined with an Overhauser magnetometer and an on-site variometer. From 2005 on, the joint efforts of HMO and GFZ Potsdam in the frame of the Inkaba project[2] allowed for annual returns of the entire network of about 40 stations. Korte et al. (2007) give a detailed insight in the measurement methods and the processing applied to the data acquired on
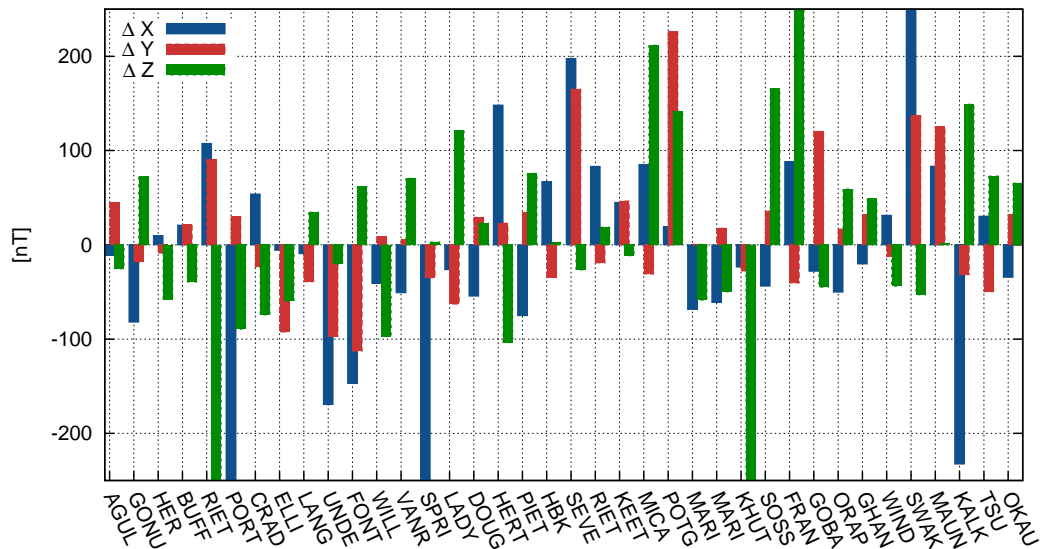
---

[2]http://www.inkaba.org/

Figure 4.8: Crustal biases calculated as average difference between annual mean values and CM4 data. The geomagnetic latitude of the stations increase from left to right.

this network.

A detailed inspection of the time series of all stations visited between 2000 and 2010 reveals that the improvements in accuracy are striking especially after 2005. For further analysis, the *recent data set* was compiled of measurements taken after 2005 and visited at least 4 times until 2010 yielding 31 repeat stations. Monthly mean values between 2005 and 2009 of the three observatories HER, HBK and TSU complete the data set.

4.2.3   Comparison with global models

In this section, both data sets are compared with global field models. From the misfit between data and model, crustal contributions and data covariances can be estimated, the shortcomings of the global models can be demonstrated.. The ancient data between 1961 and 2001 are compared to the long term model CM4. For the more recent data, the GRIMM-2 model is chosen.

Comparison with CM4: Crustal Biases

The extended comprehensive model, already described in section 3.1.3, is the most appropriate model for the long term comparison. Unlike the IGRF, CM4 is continuous over its 42 years validity period.

As the information in the repeat station data is comparable to annual mean values, the magnetic field at the 38 repeat station and observatory locations are computed with CM4 and averaged over one whole year. The resulting field deviates from the measured one and this difference changes in time. The average bias is calculated as a mean value over all residuals for all visits of one station. This bias is displayed in Fig. 4.8 where the stations
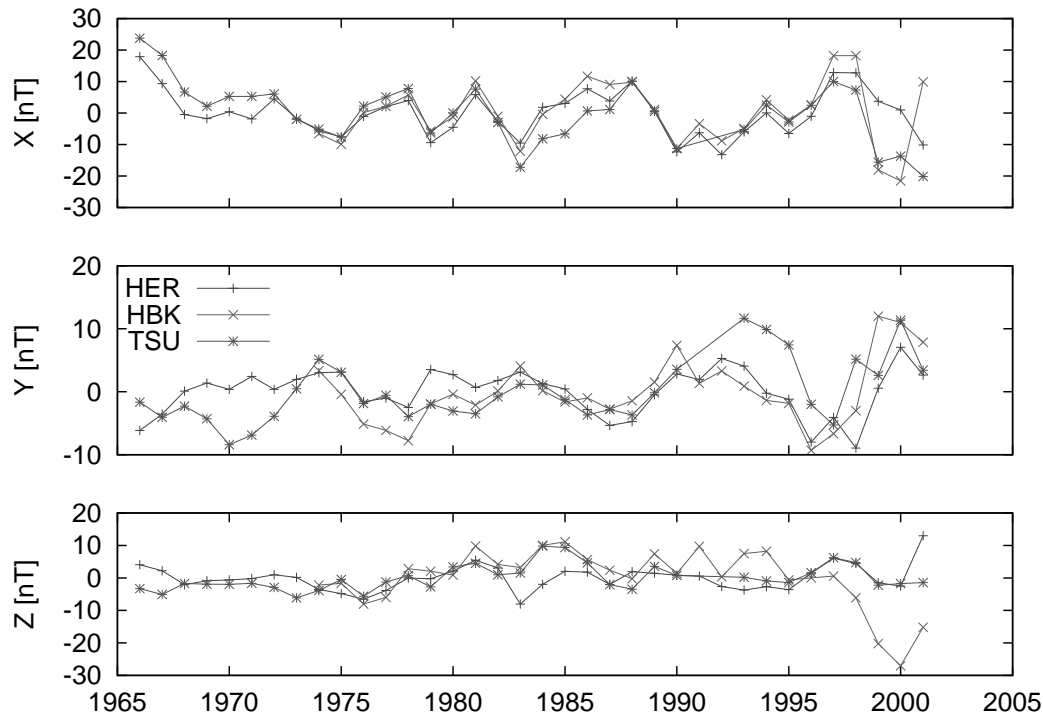
Figure 4.9: X,Y and Z residuals at the three observatories after subtracting CM4 model predictions and the average crustal contribution.

are ordered according to their geomagnetic latitude. For most stations, the absolute value of the average bias is lower than 50 nT in all components. The Y component features the smallest deviations, due to the fact that Y is the smallest component of all. For X and Z, deviations of 150 nT and higher occur more frequently, namely at POR, UND, SPR, SEV, SWA and KAL for X and RIE, MIC, KHU, SOS and FRA for Z. The biggest difference is noted for Francistown: The average of the deviation of the Z component is about 470 nT.

The distribution of the most deviating stations looks unsystematic: stations with high deviations are distributed all over the area of interest. High biases also seem not to be correlated with known magnetic anomalies. One would expect high differences for stations close to the Beattie anomaly in South of Africa, but only one station with high bias coincides with this anomaly.

The observatory biases can be compared to the ones found by Mandea and Langlais (2002), but the agreement is found to be low. For TSU, the sign and the order of magnitude match in all components, but the biases for HMO and HBK cannot be confirmed.
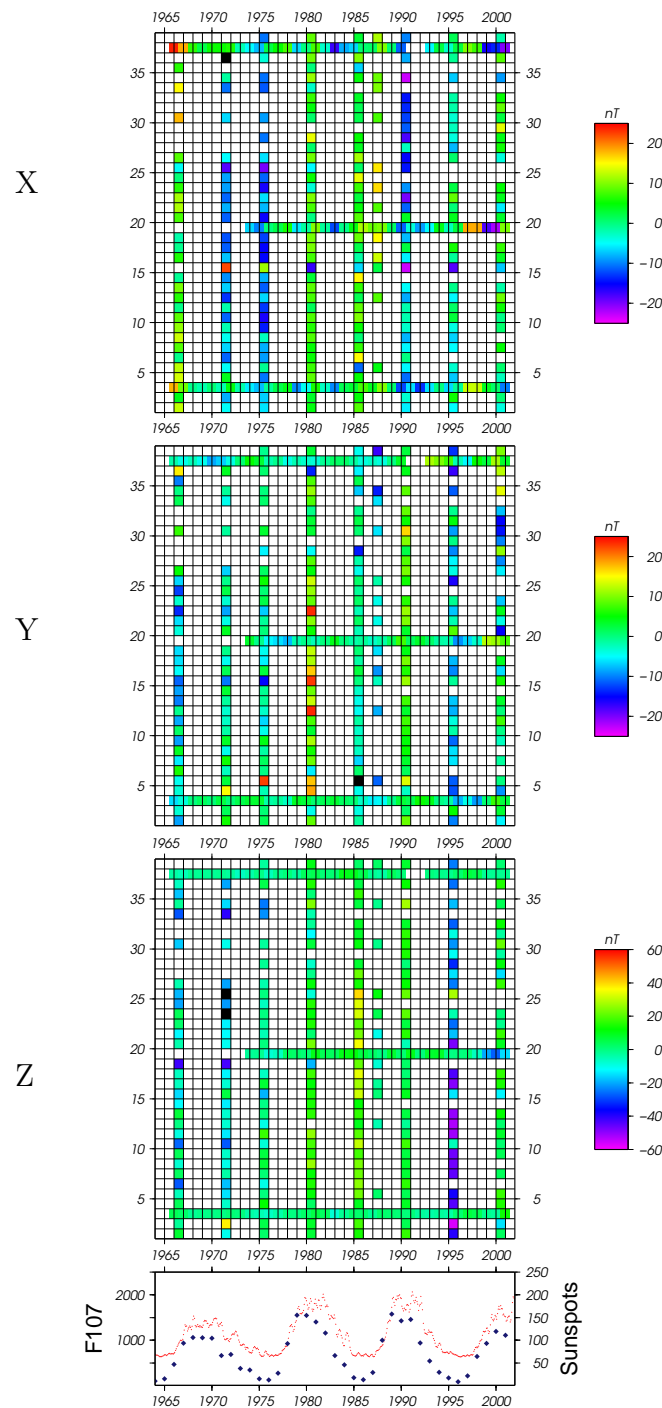
Figure 4.10: Differences between the real data and the corresponding synthetic data estimated from CM4 model, ordered according to the station and observatory numbers (cf. table B). Crustal biases (average of differences between data and CM4 predictions for each location) are subtracted. X, Y and Z components are shown from top to bottom. Variations in time are similar for all stations. The graph on the bottom displays the sunspot number (blue) and the solar flux irradiation (red) as an expression of external field activity.

Evolution of crustal biases

For a deeper understanding of the biases, differences between modeled and real values with subtracted bias are also examined. Figure 4.9 shows time series of the three observatories. The CM4 model prediction and the crustal bias derived in the previous section are subtracted from the real data. The residuals vary slightly in time. In the Z component, HBK shows a distinct minimum around 2000.0 which is not visible in HER and HBK. The Y component features different trends for HER and TSU between 1965 and 1975, but except for this, most of the variations are common to all three locations.

Ordered according to their geomagnetic latitude, the deviations of the field value from the predicted value minus the bias are plotted in Fig. 4.10 for stations and observatories. The sun spot number and the solar flux irradiation are shown below for comparison with to external influences.

Due to the fact that the repeat stations were only visited every five years, the matrix of the temporal variation is filled scarcely; only the observatories show continuous time series. Still, some common features can be noticed: For Y and Z, the differences are negative in the solar minimum of 1995 and positive in the solar maximum of 1990, for X this is vice versa. This trend can be discovered also for the other years, but less distinctively. For European observatory annual means, Verbanac et al. (2007) proposed a correction scheme for those (possibly) external contributions. First, all data are compared to CM4 and biases are calculated as averages of the residuals. From the remaining variations, a template can be produced reflecting the average in each component, where only the least scattering observatories are considered. This template is then subtracted from all annual means.

However, I did not apply this data cleaning procedure, because the matrix of the evolution of the crustal contributions is too sparse to build a reliable template. Thus to avoid the possible introduction of additional errors in the datam, I regard the remianing external signals acceptable.

Comparison with GRIMM-2

For the recent data set (2005.0-2009.97), a similar comparison with the global GRIMM-2 model is performed. As for this period the data are provided in an unreduced format, the GRIMM-2 internal field for the exact measurement date is calculated providing another set of crustal biases.

Due to the few number of data per station, the estimates of crustal biases are less reliable and an inspection of their temporal evolution is dispensable. Nonetheless, the biases agree well with the ones derived from the ancient data set. For the three observatories, the biases are listed in table 4.1. TSU observatory shows the best accordance.

observatory	ΔX	ΔY	ΔZ	ΔX	ΔY	ΔZ
HER	3.3	13.3	9.3	9.5	-8.7	-57.8
HBK	80.8	-7.5	28.6	67.0	-34.6	2.7
TSU	25.4	-52.8	71.6	30.3	-49.6	72.9

Table 4.1: Observatory biases derived for the ancient (left columns) and recent data set (right columns).

4.3   Specific Models: SAMS and X-SAMS

The elaborate data set favours regional geomagnetic field modelling. However, until now, only a few attempts have been conducted. The models presented in Kotzé (2003) and Kotzé et al. (2007) offered epoch-based description and were based on SCHA and polynomials fields respectively. Harmonic splines for spatial combined with B-splines for temporal offer for the first time the derivation of a continuous, potential field model.

Applying the splines technique to the two data sets described in chapter 4.2, two continuous field models are derived: SAMS covering the long term from 1961 to 2001, X-SAMS based on the recent data from 2002.4 to 2009.2. In this chapter, the main characteristics of the two models are first described and the results concerning the main field and the secular variation are interpreted afterwards.

4.3.1   SAMS: The South African Model made of Splines

From the study of the synthetic data set made of CM4 'annual means' (see chapter 3.3.4), we adopt the following parameters:

- The damping coefficients are set to $\lambda_t = 1 \times 10^{-1}$ and $\lambda_s = 1 \times 10^{-4}$.

- Order five B-splines are used to describe the evolution in time. Spline knots are separated by 2.5 years from 1961 to 2001 leading, to 27 knots

Unlike the synthetic data, the real measurements contain a crustal offset in each of the three field components. This requires $3 \times n_{loc} = 3 \times 38$ additional free parameters.

Results concerning the main field

The quality of the obtained Southern African Spline Model (SAMS) is firstly checked by comparing the residuals with respect to the used data. We compute the residual average for all three components. It stays below 0.01 nT with a rms value of about 4.5 nT for X and Y components and 6.5 nT for the Z component. This is of the order of the expected data error.

From the SAMS model, synthetic data can be computed at any epoch. However, only results for 1971 and 1990 are used, as for these epochs measurements are available for nearly all stations. Figures 4.11 and 4.12 show comparative maps for the core field derived from the SAMS and CM4 models. Each disc, centred on an observatory or repeat station

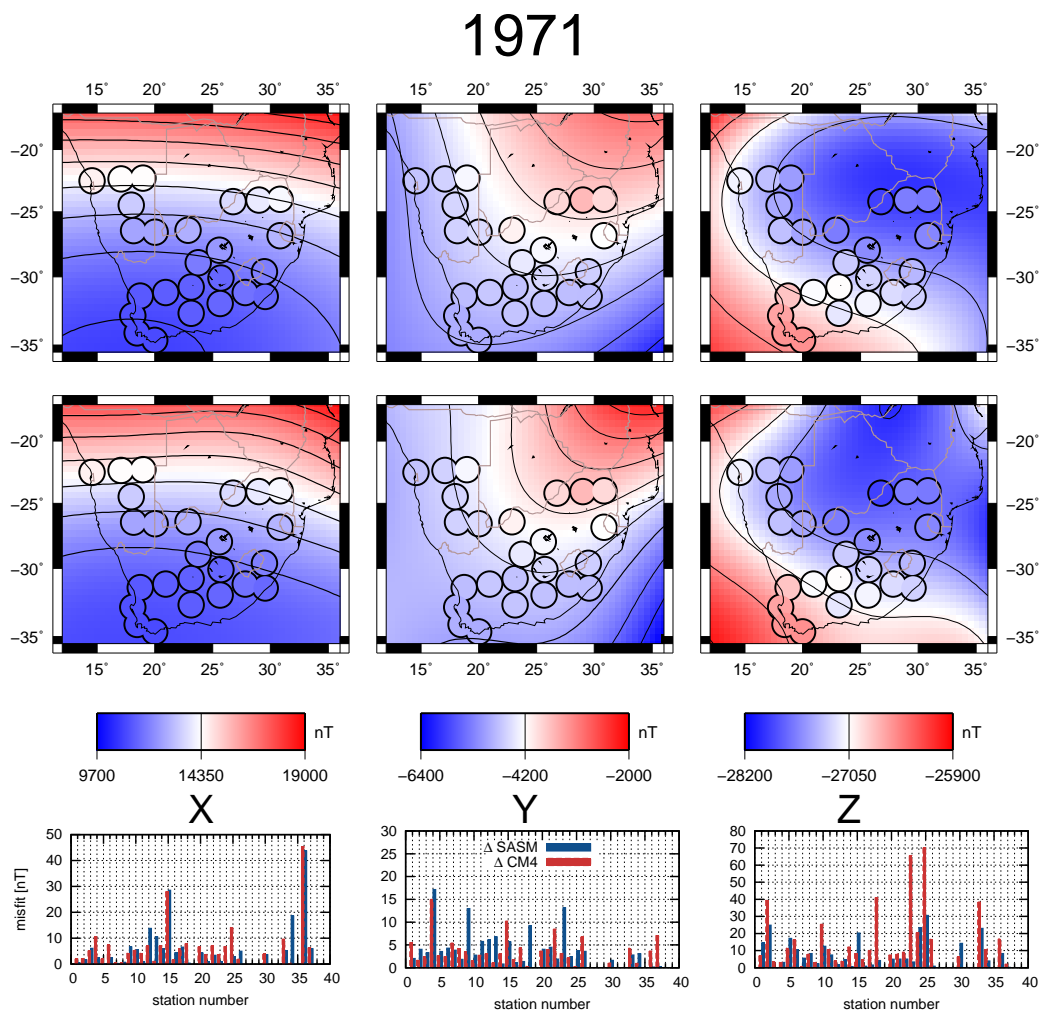**Figure 4.11:** Maps of the X, Y and Z components of the core field in (nT) as derived from CM4 (top) and SAMS (bottom) models for the epoch 1971. For comparison, the differences between measurements and synthetic data derived from CM4 corrected for the crustal offset as estimated in section 4.2.3 are also shown. The station and observatory numbers correspond to those in table B. For more explanation see text.
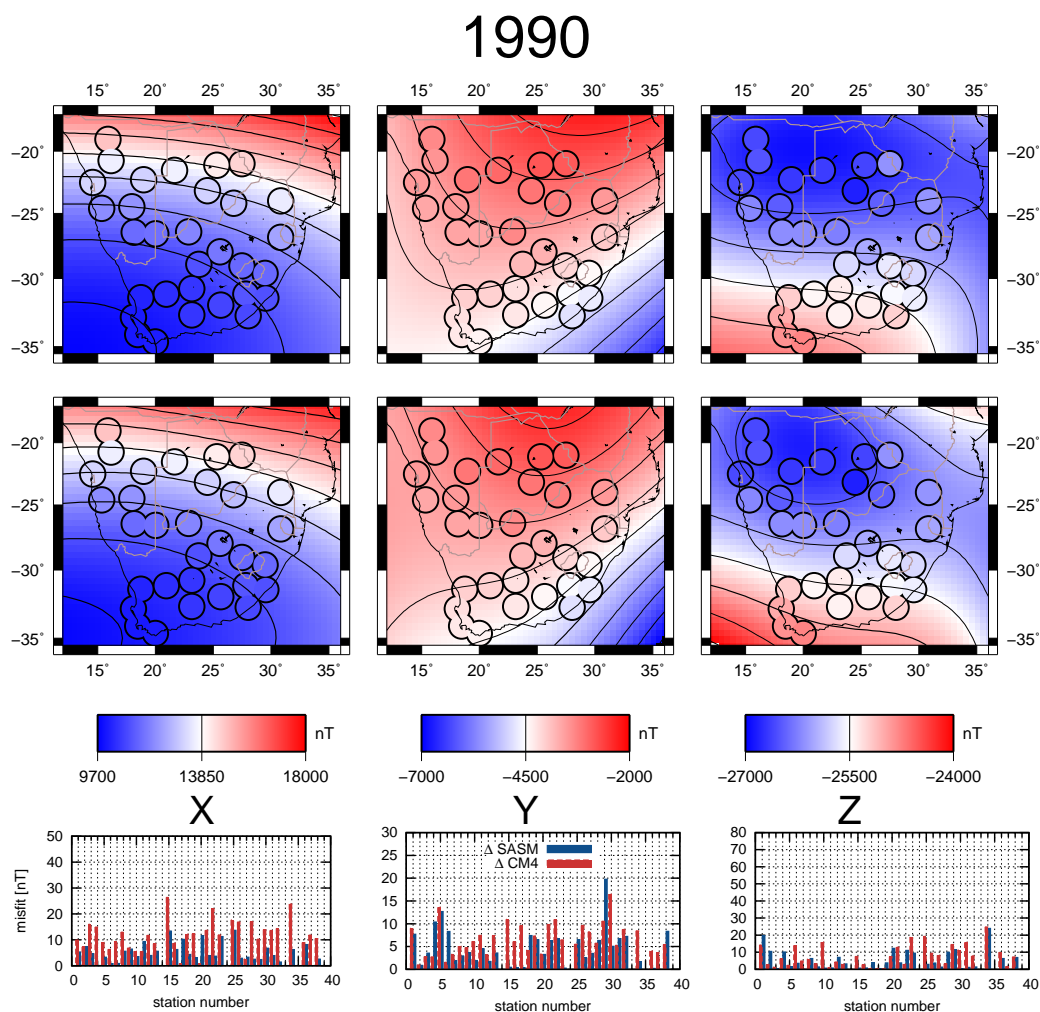
Figure 4.12: Same as figure 4.11 for the epoch 1990.

position, indicates the measured data at this epoch. The same color scales are used for models and measurements. Contour lines are separated by 1000 nT for X and by 500 nT for Y and Z. The bottom panels show the differences (for X, Y and Z components, with different vertical scales) between measurements and synthetic data derived from SAMS (blue). The regional SAMS model fits the available measurements better than CM4 does. Moreover, SAMS is able to describe some small scale features, such as the curvature in the Z component, clearly visible in 1971. Also for the other components and other epochs, the contour plots derived from SAMS are more structured. To underline SAMS' ability to follow the field behaviour more closely, the differences are shown separately, ordered according to the station location. These differences, generally of the order of some tens of nT for the 1990 epoch, are smaller when SAMS is used. For both models, the residuals of the Z-component for 1990 are dramatically reduced compared to 1971, indicating clearly the change in the instrumentation used for field measurements.
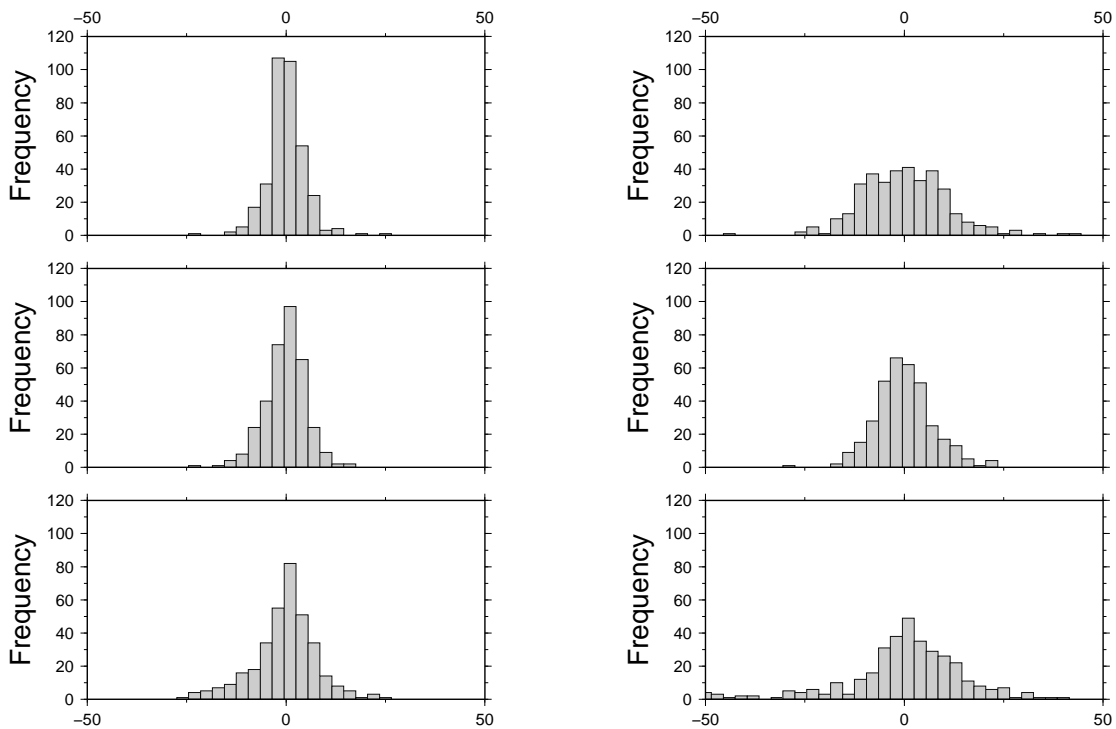
Figure 4.13: Histograms of misfit for all stations and all years when modeled by SAMS (left) and CM4 (right) models have been used. The X, Y, and Z components are shown from top to bottom.

Finally, histograms of misfit for predictions by SAMS and CM4 are computed (Fig. 4.13). The histogram obtained from SAMS are narrow, centred on zero and decrease rapidly, while the histograms computed from CM4 appear much broader in shape. This distribution is expected, but it also underlines that a regional model like SAMS can rather map spatial variations than global ones.

Results concerning secular variation

As for the core field, maps of the X, Y, and Z secular variation can be computed and drawn easily. They are available as animations[3]. Probably the most significant improvement of the presented model, compared to previous geomagnetic models over this region, is its ability to map small-scale features of the secular variation. This is illustrated in Fig. 4.14, which shows observatory monthly mean and modeled values (from SAMS and CM4) of the first time derivative of the X, Y, and Z components at Hermanus and Hartebeesthoek observatories. The SAMS model describes well the secular variation in X and Y components. For Z component, the fit is less good, and especially for HBK,

---

[3]see supplementary material:
`www.gfz-potsdam.de/portal/gfz/Struktur/Departments/Department+2/sec23/projects/`
`modeling/SAMS`
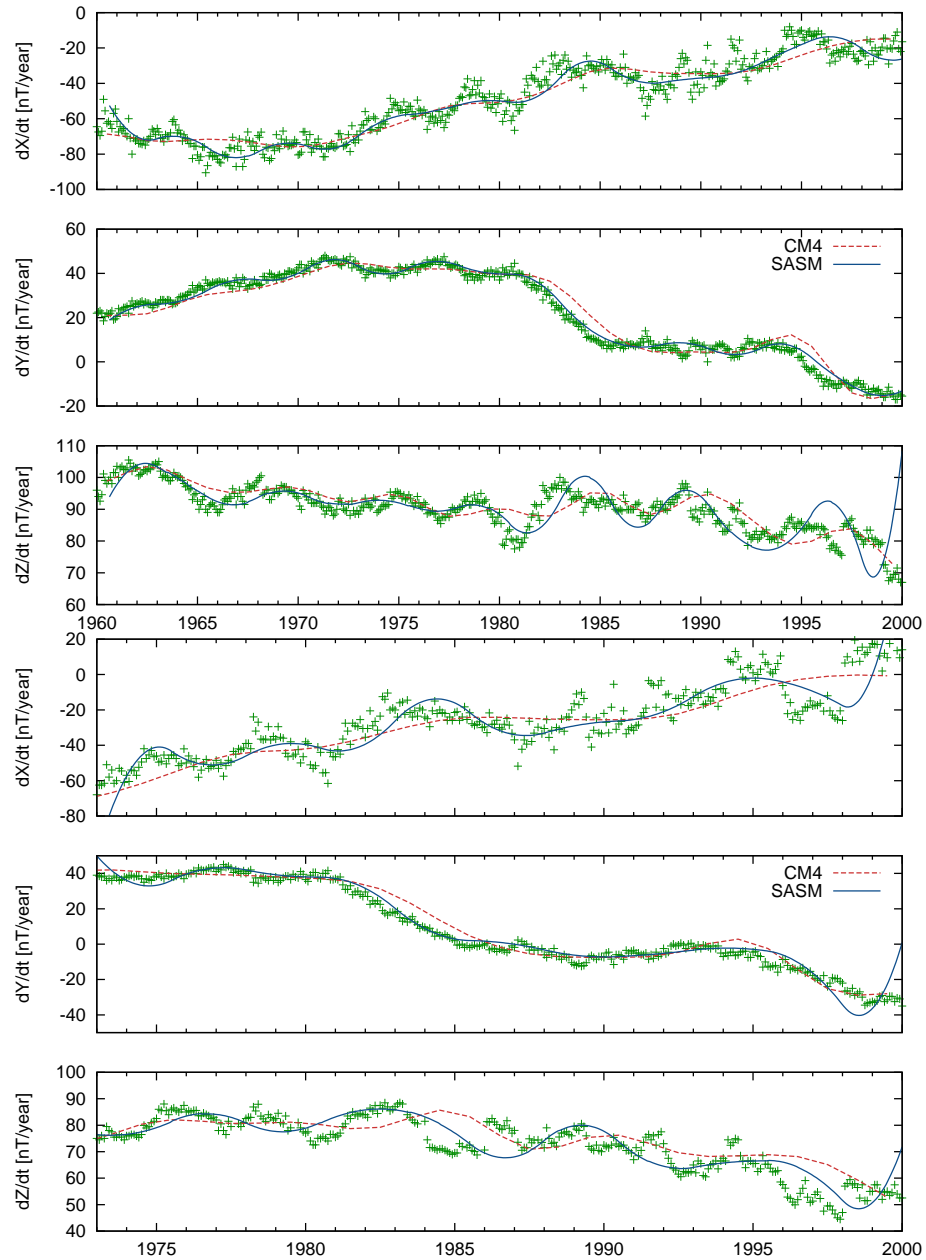
Figure 4.14: Secular variation at Hermanus and Hartebeesthoek observatories derived from monthly means (crosses) and predicted by SAMS (blue) and CM4 (red) models.
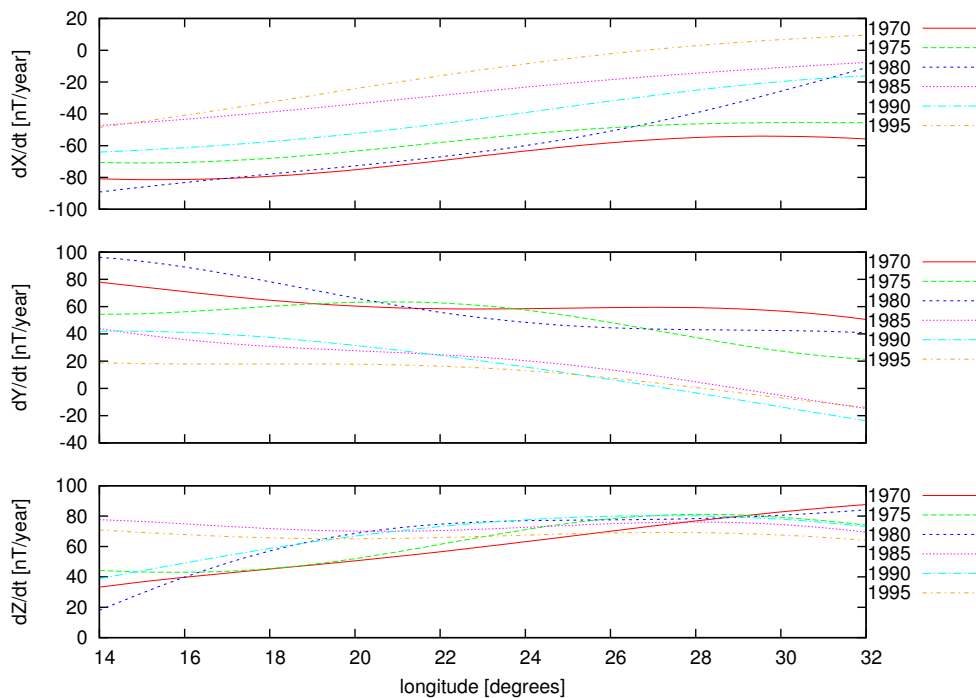
Figure 4.15: Secular variation estimated from SAMS model on a profile going from $14°$ to $30°$ E longitude at fixed latitude ($\vartheta = 25°$S).

temporal edge effects can be observed. However, our model is able to follow more closely the real data than the CM4 model. We therefore regard SAMS as a suitable model to describe geomagnetic field changes over this region.

To point out some interesting features of the secular variation in this region, I investigate the changes of the secular variation on different profiles, the one shown here being at latitude $25°$S, from $14°$ to $30°$ E longitude (Fig. 4.15). The X component has a nearly flat longitudinal gradient, its changes in time being marked by a decrease of $30 - 50$ nT/year from 1975 to 1995. More complicated is the Y component behaviour, for which the changes are dramatically important in the most western part and at the beginning of the period. Finally, remarkable accelerations (from 80 nT/year to 20 nT/year) are seen in the Z component in the western part, while the secular variation remaining at around the same order of about 80 nT/year in the eastern part. This value is comparatively high compared to the global rms value of $dZ/dt \sim 66$ nT/year calculated from the IGRF for 1970, which underlines once more the exceptional behaviour of the magnetic field in this region.

4.3.2 The Extended South African Spline Model

The elaborate data set favours regional geomagnetic field modelling. However, until now, only a few attempts have been conducted. Kotzé (2003) applied SCHA and used SV data
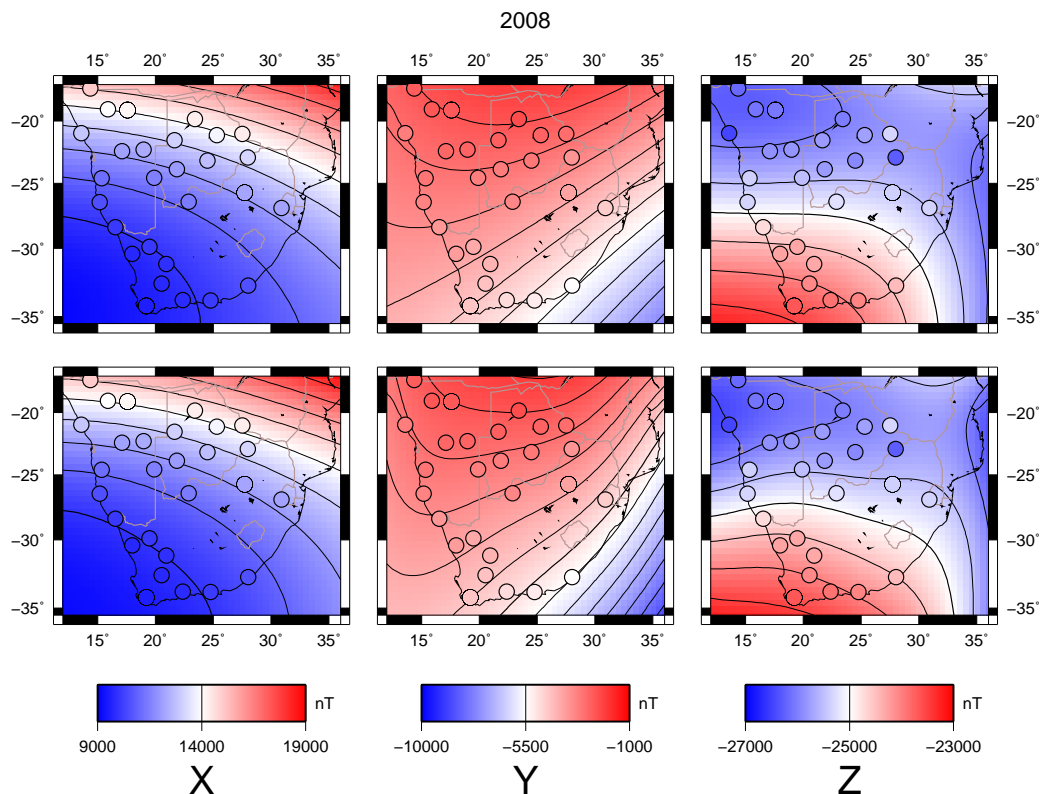
Figure 4.16: The X-SAMS model prediction for 2008 (bottom) and the respective map calculated from GRIMM-2 model (top). As in Fig. 4.11, the belonging data measured at the epoch are shown as circles in the same color scale.

to build a polynomial model for epoch 2005.0. As illustrated in section 4.2.2, a separate field model is developed for the recent data to account for the improved measurement quality and frequency in the recent years. The Extended South African Spline Model (X-SAMS) is parametrized as follows: Cubic B-splines are used with spline knots only at the outer borders 2005.0 and 2010.0 and with one interior knot at 2005.0. This low temporal resolution is owed to the fact that only four or five measurements are available per repeat station. The damping parameters used already for the model applied to the ancient data turned out to be the optimum also for this data distribution.

The model achieves a slightly better accuracy than its predecessor: The rms value amounts to about 3.1 nT for the X and Y components and 4.5 nT for the Z component, reflecting the improved measurement quality.

Results concerning main field and secular variation

Figure 4.16 shows a map of X-SAMS for epoch 2008 in comparison with the respective GRIMM-2 prediction. Differences are mainly visible in Y and Z. For these components, contour lines in the centre areasshow notably differing shapes.

Extracting information about the SV derived from data covering only five years should
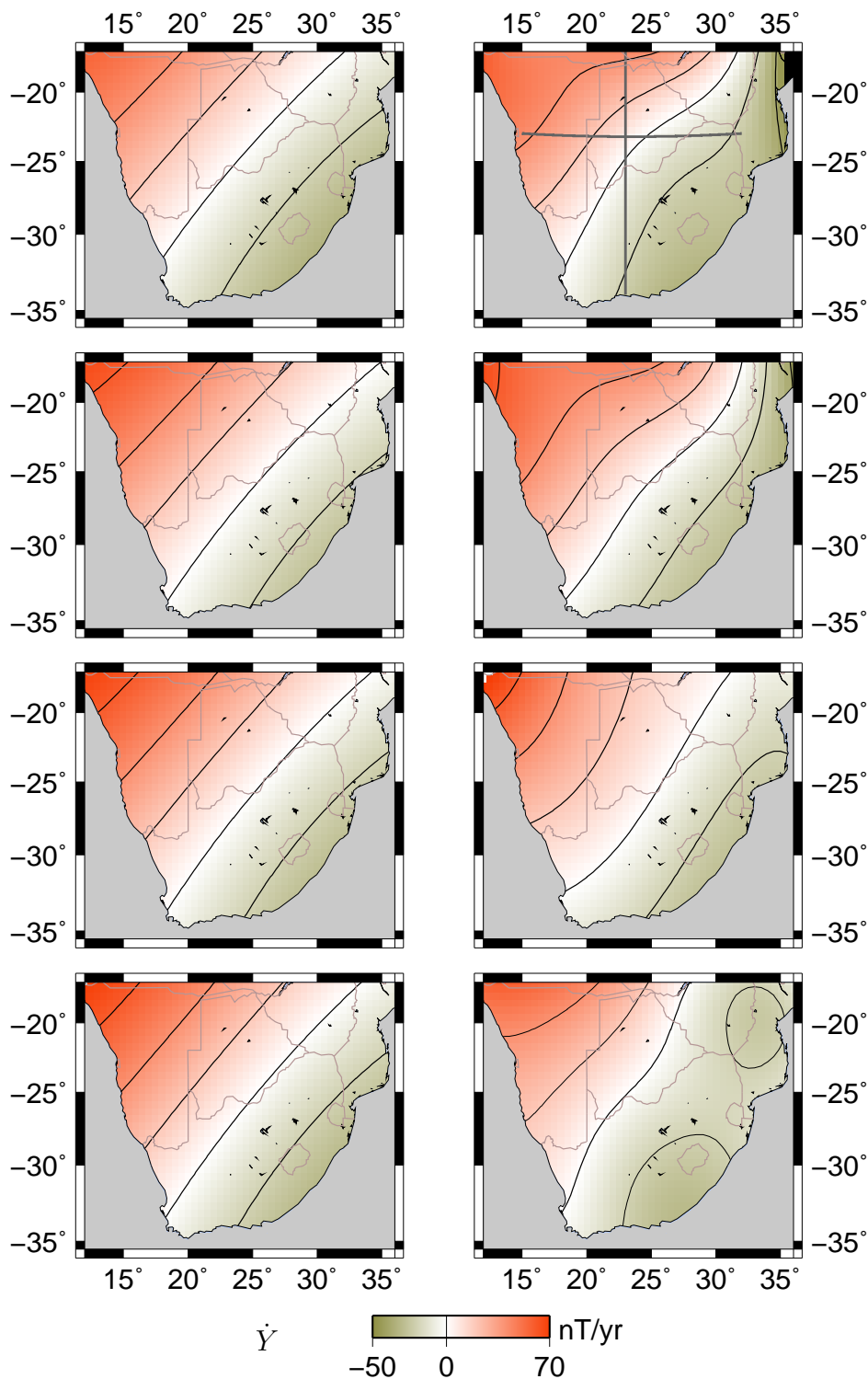
Figure 4.17: Prediction of secular variation of the Y component derived from GRIMM-2 (left) and X-SAMS model (right) for the epochs 2006.5, 2007.5, 2008.5 and 2009.5 from top to bottom. Contour lines are separated by 20 nT/year. The cross in the upper left map shows the location of the profiles in Fig. 4.18.
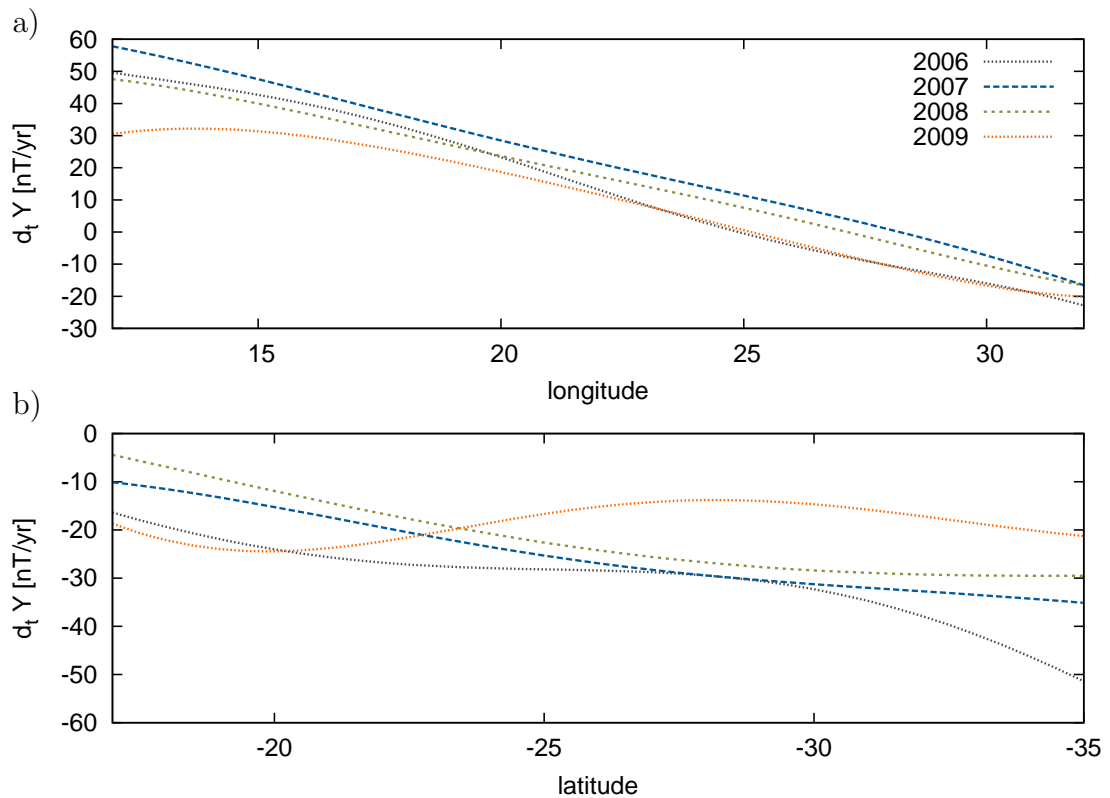
Figure 4.18: Profile of secular variation of the East component at a fixed latitude of $\vartheta = 23°$S (a, top) and at a fixed longitude of $\varphi = 23°$E (b, bottom) for four epochs.

be done with precaution. Nonetheless, we draw a map of the SV of the East component ($\dot{Y}$) predicted for the epochs 2006.5, 2007.5, 2008.5 and 2009.5 and compare it with the respective maps derived from GRIMM-2 (Fig. 4.17). The most eye-catching feature, the strong gradient from North-West to South-East is common to all epochs and both models. North-West of the zero line, the secular variation is positive (shown in red) effecting an increasing East component and declination, while both components tend to decrease in the South-East. However, the contour lines for GRIMM-2 are nearly parallel and rather keep their shape and position throughout the four epochs shown here. In contrast, the contour lines of X-SAMS are more curved and especially the line of vanishing secular variation is steeper. Figure 4.18 shows profiles of $\dot{Y}$ along a fixed latitude of 23° S and along fixed longitude 23° E. The East-West profile is nearly straight for all epochs except for 2009, while the North-South profile is rather dynamic.

Chapter 5

Probing the global secular variation with splines

Thanks to the past decade of Geopotential Field Research, including the satellites CHAMP, Ørsted and SAC-C, recent core magnetic field models achieve a high accuracy and are able to describe fields measured at the Earth's surface and at satellite altitude. However, if the SV predictions from sophisticated models like GRIMM-2 or CHAOS-2 are compared to SV estimates derived from observatory monthly means, several variations are not captured. These differences become evident when the short term SV is considered, i.e. very fast variations of a few months duration are not reflected by the models. Annual differences of monthly means are usually considered as SV estimates and hence regarded as purely of internal origin , but the observed short periods rather hint for external sources. In this section, I identify observatories for which SV time series are not fitted properly. The differences between the SV derived from monthly means and GRIMM-2 are then modelled with the harmonic spline functions introduced in chapter 3. This basis is useful because it is interpolatory and hence permits an exact fit to the data. After a rotation into the geomagnetic system of coordinates, the model reveals a a uniform behaviour of the globally distributed observatories and thus indicate an external origin.

5.1 Discrepancy between data and models

The compilation of IGRF-11 stimulated the generation of several candidate models. In this context, Olsen et al. (2009) developed the main field model CHAOS-2 spanning the years 1997.0-2009.5. The model is available in two versions: either as a smooth (more damped) version CHAOS-2s or the rough (less damped) version CHAOS-2r. The rough version gives a lot of freedom to the model and allows to follow up even short (< 1 year) variations. Figure 5.1 shows secular variation estimates (annual differences of monthly means) of the vertical component for the observatories Kakioka (Japan) and Guam (in the Pacific) along with the respective predictions from the global models CHAOS, CHAOS-2 and GRIMM. For both observatories, the data feature a high variability, especially in the
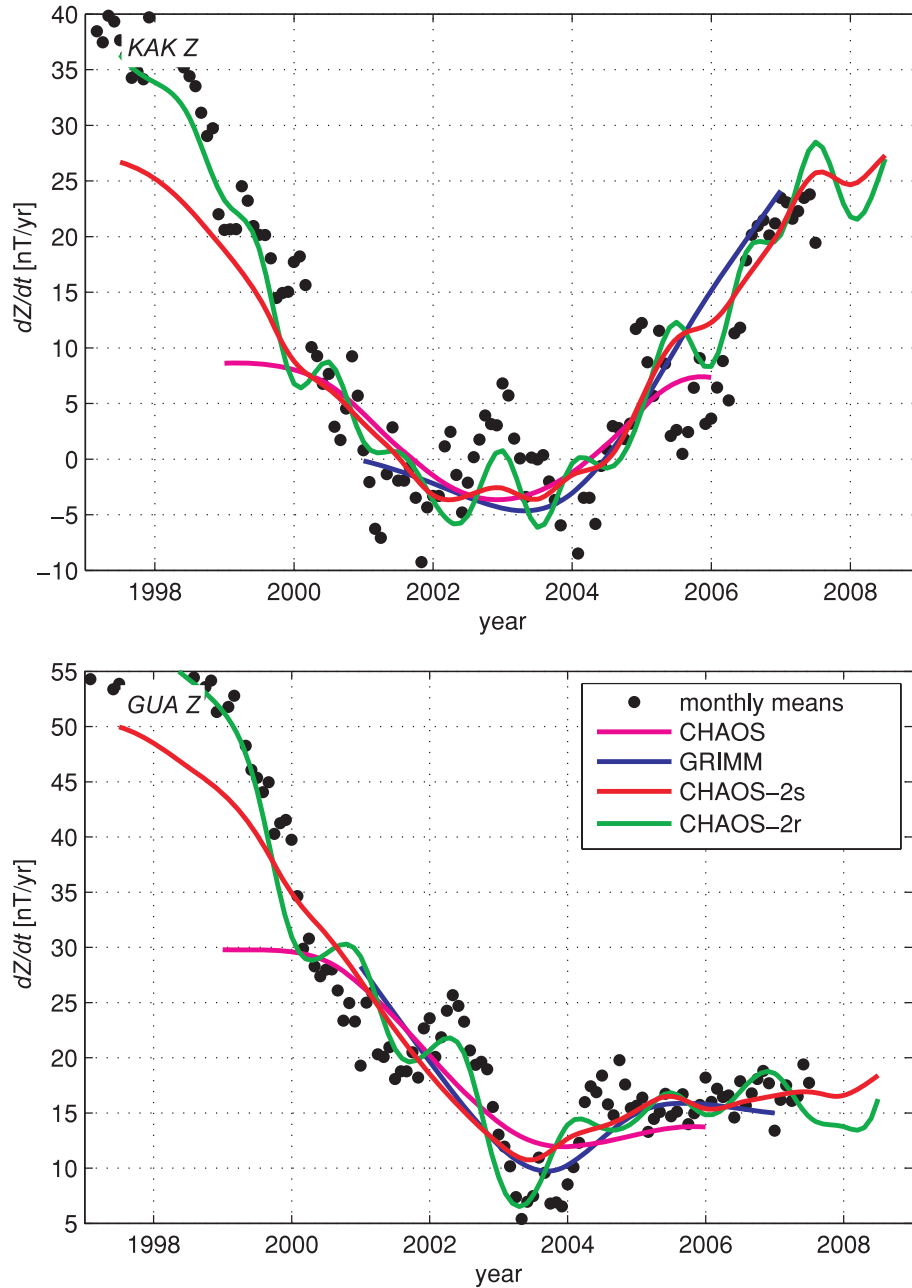
Figure 5.1: Secular Variation of the vertical component derived from observatory monthly means together with predictions from the recent field models CHAOS, CHAOS-2 and GRIMM at Kakioka, Japan (left) and Guam, Pacific Ocean (right). Explanation see text. From Olsen et al. (2009).
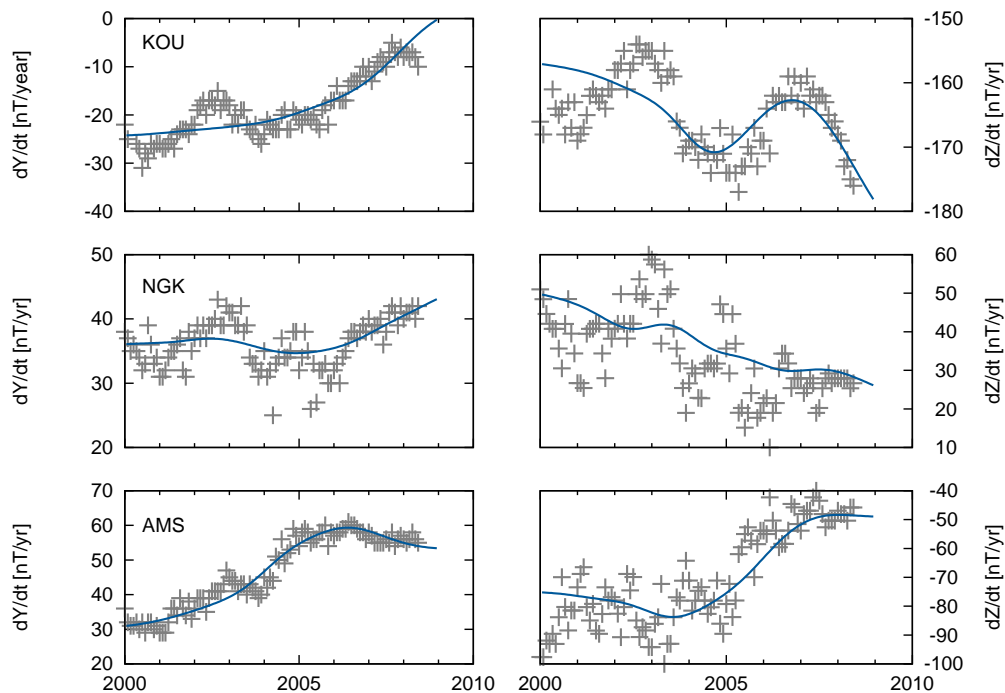
Figure 5.2: Secular variation derived from monthly means (crosses) with the respective GRIMM-2 prediction (solid line) for Niemegk, Kourou and Amsterdam Island (from top to bottom) in East (left) and vertical (right) direction.

period between 2001-2004. Neither CHAOS (magenta line), CHAOS-2s (red solid line) nor GRIMM (blue line) reproduce these rapid changes. The rough version CHAOS-2r (green solid line) accomplishes this task but at the expense of introducing several small "wiggles", also at places where no fluctuations are obvious in the data. Olsen et al. claim to suppress any ionospheric contributions by using only quiet-time satellite and monthly means ground-based data. As the variations can be reproduced by an internal potential field, magnetospheric influences are also unlikely. Hence, the authors conclude that the rapid variations are of internal origin. A further argument for the internal provenance can be drawn from an investigation of small-scale core flows as presented by Olsen and Mandea (2008). The authors indicate the spatial localization of the core flow leading to large local accelerations. They also link those accelerations with length of day (LOD) variations generated by the unequal mass transport in the Earth's core.

To analyse the discrepancy between predicted and observed secular variation in more detail, Fig. 5.2 shows SV estimates from monthly means together with the GRIMM-2 prediction at some more observatories, i.e. Kourou (KOU) in French Guayana, Niemegk (NGK) in Germany and Amsterdam Island (AMS) in the South Indian Ocean. The noisy X component is omitted. GRIMM-2 captures accurately the trend for all observatories (except for the dZ/dt in Kourou at the beginning of the millennium), but several deviations remain. The East component shows clearly an enhancement around 2003.0 for all three observatories, even though less pronounced for AMS. The vertical data is more am-

biguous, a remaining fluctuation between 2000.0 and 2005.0 not mapped by the GRIMM-2 prediction is obvious.

According to Olsen et al. (2009), those observations might result from sources internal of the Earth's surface. The authors are cautious and avoid a definitive conclusion. In fact, several aspects are in the favour for an external origin. A strong argument considers the structure of the Earth. Between the outer fluid core, where the main field is generated, and the Earth's surface, where the field is measured, lies the mantle, composed amongst others of metallic material. Its conductivity is able to shield variations generated in the core: the higher the conductivity, the higher frequencies are shielded. Very early (Runcorn, 1955) already showed that for a secular variation impulse of 4 years duration not to be screened by a plate of thickness 2000 km, the average electrical conductivity of the plate must be less than $100\,\Omega^{-1}m^{-1}$. This value was confirmed by (Ducruix et al., 1980). Faster variations would imply an even lower value, which is not considered in the modern literature Kuvshinov and Olsen (see e.g. 2006), Constable and Constable (see e.g. 2004), Velimsky et al. (see e.g. 2006) .

The mismatch between global models and SV estimates is a promising application for the harmonic splines. Especially its interpolatory characteristic is useful: We can be sure that all data are fitted by this model and hence be able to study the structure of the residuals.

5.2   Selected data subset

To test the hypothesis of an external source, 18 observatories were selected according to the following aspects: The belonging time series should either agree well (like AMS) or show remarkable deviations (like KOU) from the GRIMM-2 predictions. Furthermore, the locations should be more or less equally distributed over the globe. The limited number of 18 observatories allows an easy-to-handle amount of data and to skip observatories with incomplete time series. Figure 5.3 shows a map of the considered observatories, an exact list containing the geocentric positions and observatory codes is given in the appendix B. From these observatories, the secular variation estimates were calculated as annual differences of monthly means (cf. chapter 2.1.2)

I want to focus on the remaining variations that are not fitted by GRIMM-2. For that purpose, GRIMM-2 is subtracted from the data. The SV estimates are not modelled directly but only the residuals between data and GRIMM-2 prediction.

5.3   Modelling approach

To describe the differences between GRIMM-2 and the SV estimates, I use the harmonic spline functions derived in the previous chapter. The maximum degree was chosen to $L = 8$, reflecting allowing to resolve the typical core wavelengths. To parametrise the
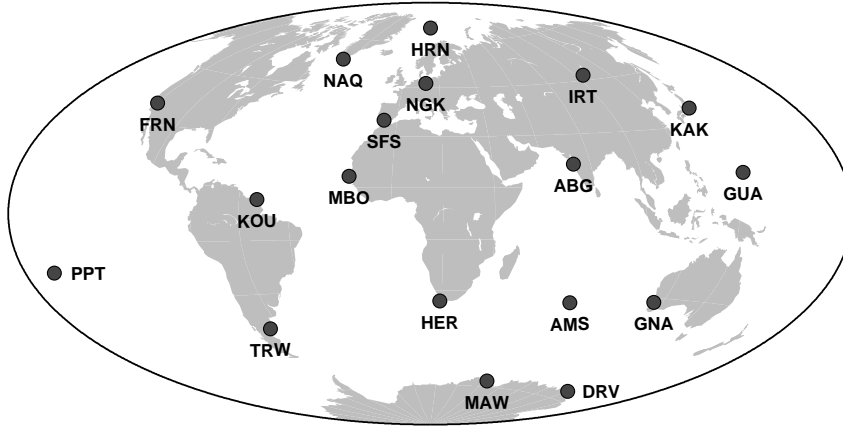
Figure 5.3: Distribution of the 18 observatories selected for the global study.

model in time, cubic B-splines are chosen with a knot separation of 0.5 years between 2000.0 and 2008.5. The degree and knot position is identical with the parametrisation used for GRIMM-2. An improved fit to the data can therefore not be attributed to a different temporal representation.

As I suppose an external source, the main signal is expected to be seen parallel to the dipole axis. Hence, the data and base functions are rotated into a geomagnetic coordinate system where the Z_{mag} axis is radial parallel to the dipole axis. The coordinates of the north pole $(\vartheta_{\mathrm{NP}}, \varphi_{\mathrm{NP}})$ can be derived using the first Gauss coefficients following

$$\vartheta_{\mathrm{NP}} = \arctan \frac{g_1^0}{\left(g_1^1\right)^2 + \left(g_1^{-1}\right)^2} \quad \text{and} \quad \varphi_{\mathrm{NP}} = \arctan \frac{g_1^1}{g_1^{-1}} \ . \tag{5.1}$$

The linearly time-dependent IGRF coefficients are sufficient for this coordinate transformation. The orientation of two other, tangent components is not intuitive but also not important.

5.4 Results and interpretation

Applying the harmonic splines to the residuals between GRIMM-2 and real data yields a good fit with an average residual of 0.01 nT/year for components. The rms amounts to about 2.1 nT/year in X_{mag}, 3.5 nT/year in Y_{mag} and 6.1 nT/year in Z_{mag}. Figure 5.4 shows the input "data", hence the residuals between SV derived from monthly means and GRIMM-2, as grey crosses. In this stacked plot, all data and the resulting harmonic splines fit are plotted together. Each blue line indicates the fit to one observatory. Apparently, the data and the fit are very scattered, centred around zero and uncorrelated between the different observatories. Although some major outliers can be remarked, the splines attempt to fit only noise. The result for the component aligned with the dipole is more striking: all time series for all observatories are in phase for most of the time.
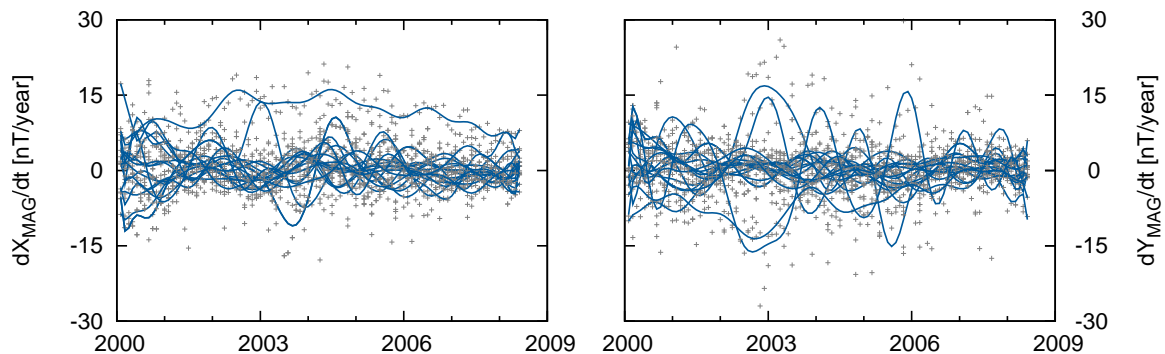
Figure 5.4: Stacked plot of the residuals between GRIMM and SV in two directions orthogonal to the dipole dX_{mag}/dt and dY_{mag}/dt (left). Crosses indicate the residuals, the blue lines show the harmonic splines fit to the data.

Until approximately 2002, the correlation is less evident. But between 2003 and 2008, an oscillation with a period of nearly two years and an amplitude decreasing from $30\,\mathrm{nT/year}$ to about $5\,\mathrm{nT/year}$ is more than obvious. This common, dipole-aligned behaviour clearly hints to an external source.

Considered as a case study for the applicability of the harmonic splines, I do not focus more on the possible sources generating these variations. However, their global and external properties can be pointed out. Hence, I am confident stating that the "SV estimates" derived from monthly means are contaminated by external contributions and cannot be considered as true SV which originating only in the core. If they are, nonetheless, chosen to derive the temporal change of the main field, more effort has to be paid for minimising external contributions. A possible approach to address this task is already done by Wardinski and Holme (2010). In a joint inversion of magnetic field and SV, the authors detect Eigendirections of the noisiest components in the SV. Exploiting a correlation with the D_{ST} index, they derive their model after several iterations, minimzing the error in each step. However, this customised method cannot be generalised easily, and it will depend on the individual approach what processing of SV data is applicable. Especially for global field models, a higher parametrisation of external contributions is rather required.
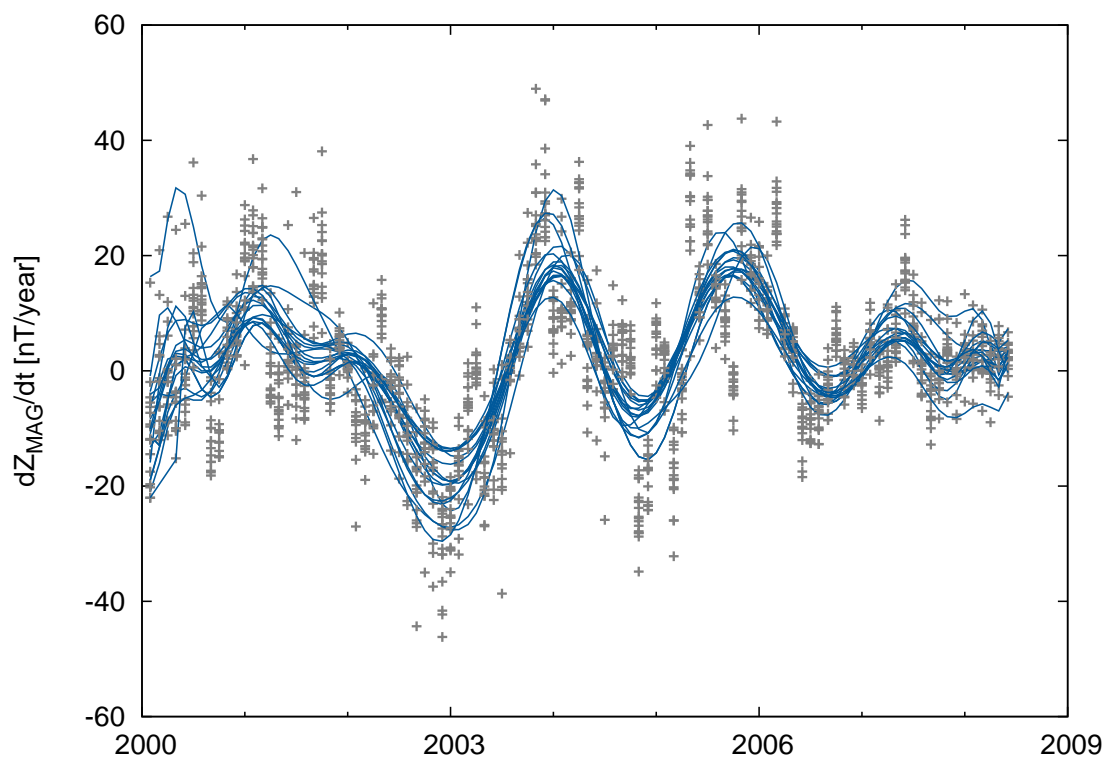
Figure 5.5: Same as Fig. 5.4 but along the direction of the dipole (dZ_{mag}/dt).

Chapter 6

Conclusion and Outlook

This thesis aimed to improve both geomagnetic measurement and modelling techniques. In the last chapter, I conclude the efforts that have been undertaken in both fields and point out what issues are still open for commitment.

6.1 Instrumentation

The set-up of GAUSS has shown that several problems of automation of absolute measurements can be overcome. It is possible to built a non-magnetic system that takes automated absolute measurements including instrument calibration and remote control. From the last two years of continuous measurements it is also clear that all chosen components work reliably on the long term. However, a satisfying base-line that can compete with one obtained by manual absolute measurements is still missing. Whether this has to be attributed to instrument intrinsic parameters or, more likely, to pillar drifts that are not yet resolved, still lacks explanation.

The DI3 technique targets the application in remote observatories where lay persons conduct the absolute measurements. An improved baseline control can be achieved because of the redundancy in one measurement set. Until now, measurements have only been performed to test he procedure and to show its potential and were carried out by skilful personal. If blind tests reveal that the accuracy of this method does not depend on the observer's experience, the DI3 technique should be adopted in several remote observatories.

6.2 Modelling

The resumption of the harmonic splines for magnetic field modelling has turned out to be successful. Due to their interpolatory characteristics, they are an easy-to-handle tool for describing geomagnetic fields from global to regional scales.

The modelling technique has been applied to the South African region and a detailed field description covering the last 50 years could be achieved, where the direct comparison to

<center>85</center>

global field models was based on the distinct maximum order L. SAMS provided a quiet long-term field description that is suitable for studying the field behaviour in this region. X-SAMS, even if only short term, still assesses the field structure and evolution satisfyingly. With every new repeat station campaign regularly carried out in the southern spring months, more data can easily be included.

However, the resolution of both models is limited both spatially and temporally. A better coverage can be achieved at two stages: The first is the installation and reliable maintenance of additional observatories in this region. The observatory in Keetmanshoop is already up and running since 2006. Its data should be included in future studies to close the spatial gap between Hermanus in the South and Tsumeb in the North. Another observatory to characterise the field behaviour in the North-East should be erected in Botswana in the medium term. Although a cooperation is planned, the search for a location is the most crucial point. Korte et al. (2009) give an overview of efforts undertaken for the installation of new observatories in Southern Africa and the South Atlantic. Anyway, additional observatories are needed to cover the area more uniformly at a high temporal resolution. The second possibility to improve the data coverage is the use of satellite data. Before CHAMP will descend and cease its life-time at the end of this year, it has collected magnetic field measurements for more than ten years. To use its data for a regional field model, sophisticated data selection is required. As I am only interested in core field and secular variation, an approach of virtual magnetic observatories as proposed by Olsen and Mandea (2007) could be useful. They extracted satellite monthly means on a regular grid at 400 km altitude to investigate the space-time structure of the short-period variation of the Earth's magnetic field. A similar approach could be used to fill the gap in between two subsequent repeat station campaigns at high spatial resolution. Indeed, the harmonic splines allow the inclusion of data from different altitudes in contrast to surface polynomials.

Furthermore, the splines have proven to be also suitable for global modelling. In a very short study, I showed that misfits arising in global models can easily be modelled by harmonic splines, especially if the appropriate geomagnetic coordinate system is used. Exploiting the interpolatory characteristics of the spline technique allowed for an exact fit to the data and revealed the global, external properties of the variances. The localized characteristic of the base function can also be used for introducing localized constraints as proposed by (Lesur, 2006). This is advantageous if the data density is not equal globally, e.g. for satellite data where measurements in the polar regions have to be skipped. Revisiting the approach of (Olsen and Mandea, 2008), the harmonic splines could also be useful to constrain localized flow features.

Altogether, the two regional and the global models benefited from the harmonic spline technique.

As long as the Earth dynamo is not ceasing, the magnetic field will continue to vary on all scales. Hence, efforts both in instrument development and in modelling techniques will prevail a dynamic field of research in the coming years.

Appendix A

Auxiliary Calculations

Derivation of additional functions

In this appendix, we derive the two additional kernels $F_i^{L\vartheta}$ and $F_i^{L\varphi}$. This is done analogously to the derivation of F_i^{Lr}, but considering the two tangential components, B_ϑ and B_φ respectively, instead of the radial component in eq. 3.27. From this, twe obtain expressions for $F_i^{L\vartheta}$ and $F_i^{L\varphi}$ comparable to the one for F_i^{Lr} (equation 3.36).

We first express B_ϑ at a certain point $(\vartheta_i, \varphi_i, r_i)$

$$
\begin{aligned}
B_\vartheta(\vartheta_i, \varphi_i, r_i) &= -\frac{1}{r}\frac{\partial V}{\partial \vartheta} \\
&= -\sum_{l,m}^{L} g_l^m \left(\frac{a}{r_i}\right)^{l+2} \partial_\vartheta \, Y_l^m(\vartheta, \varphi)|_{\vartheta=\vartheta_i, \varphi=\varphi_i} \\
&= -\sum_{l,m}^{L} 4\pi \frac{(l+1)^4 l^2}{2l+1} \underbrace{\left[\frac{2l+1}{4\pi(l+1)^4 l^2}\left(\frac{a}{r_i}\right)^{l+2} \partial_\vartheta \, Y_l^m(\vartheta, \varphi)|_{\vartheta=\vartheta_i, \varphi=\varphi_i}\right]}_{h_{li}^m} g_l^m \\
&= \sum_{l,m}^{L} 4\pi \frac{(l+1)^4 l^2}{2l+1} \, h_{li}^m \, g_l^m \\
&= \; < \mathbf{h_i} \, , \, \mathbf{g} >
\end{aligned}
$$

where $\mathbf{h_i} = [\, h_{li}^m \,]_{\{l,m\}}$, $\mathbf{g} = [\, g_l^m \,]_{\{l,m\}}$ and $f_l = \frac{2l+1}{4\pi(l+1)^4 l^2}$. The $\mathbf{h_i}$ are linearly independent vectors, and therefore, $\mathbf{g}$ can be written as a linear combination of these vectors:

$$
\mathbf{g} = \sum_{j=1}^{N} \alpha_j^\vartheta \mathbf{h_j}. \tag{A.1}
$$

87

Once the α^ϑ vector is known, the magnetic field can be computed at any point (ϑ, φ, r) by:

$$
\begin{aligned}
\mathbf{B}(\vartheta, \varphi, r) &= -\nabla a \sum_{l,m}^{L} g_l^m \left(\frac{a}{r}\right)^{l+1} Y_l^m(\vartheta, \varphi) \\
&= -\nabla a \sum_{l,m}^{L} \left\{ \sum_j h_{lj}^m \alpha_j^\vartheta \right\} \left(\frac{a}{r}\right)^{l+1} Y_l^m(\vartheta, \varphi) \\
&= -\nabla \sum_j \alpha_j^\vartheta \left\{ a \sum_{l,m}^{L} -\frac{2l+1}{4\pi(l+1)^4 l^2} \left(\frac{a}{r_j}\right)^{l+2} \partial_\vartheta Y_l^m(\vartheta, \varphi)|_{\vartheta=\vartheta_j, \varphi=\varphi_j} \left(\frac{a}{r}\right)^{l+1} Y_l^m(\vartheta, \varphi) \right\} \\
&= -\sum_j \alpha_j^\vartheta \ \nabla F_j^{L\vartheta}(\vartheta, \varphi, r) \qquad \text{(A.2)}
\end{aligned}
$$

where we substitute

$$
F_i^{L\vartheta}(\vartheta, \varphi, r) = a \sum_{l,m}^{L} f_l \left(\frac{a}{r_i}\right)^{l+2} \partial_\vartheta Y_l^m(\vartheta_i, \varphi_i) \left(\frac{a}{r}\right)^{l+1} Y_l^m(\vartheta, \varphi) \qquad \text{(A.3)}
$$

Notice that the f_l is the same as in eq. 3.36.
Finally, we consider the B_φ component:

$$
\begin{aligned}
B_\varphi(\vartheta_i, \varphi_i, r_i) &= -\frac{1}{r \sin\vartheta} \frac{\partial V}{\partial \varphi} \\
&= -\sum_{l,m}^{L} g_l^m \left(\frac{a}{r_i}\right)^{l+2} \frac{\partial_\varphi}{\sin\vartheta} Y_l^m(\vartheta, \varphi) \Bigg|_{\vartheta=\vartheta_i, \varphi=\varphi_i} \\
&= -\sum_{l,m}^{L} 4\pi \frac{(l+1)^4 l^2}{2l+1} \underbrace{\left[f_l \left(\frac{a}{r_i}\right)^{l+2} \frac{\partial_\varphi}{\sin\vartheta} Y_l^m(\vartheta, \varphi) \Bigg|_{\vartheta=\vartheta_i, \varphi=\varphi_i} \right]}_{s_{li}^m} g_l^m \\
&= \sum_{l,m}^{L} 4\pi \frac{(l+1)^4 l^2}{2l+1} s_{li}^m \ g_l^m \\
&= \ <\mathbf{s_i} \ , \ \mathbf{g}> \qquad \text{(A.4)}
\end{aligned}
$$

Again, we can write $\mathbf{g}$ as a linear combination, now of the vectors $\mathbf{s_i}$

$$
\mathbf{g} = \sum_{j=1}^{N} \alpha_j^\vartheta \mathbf{s_j}, \qquad \text{(A.5)}
$$

and we rewrite the magnetic field as

$$
\begin{aligned}
B(\vartheta, \varphi, r) &= -\nabla a \sum_{l,m}^{L} g_l^m \left(\frac{a}{r}\right)^{l+1} Y_l^m(\vartheta, \varphi) \\
&= -\nabla a \sum_{l,m}^{L} \left\{ \sum_j s_{lj}^m \alpha_j^\varphi \right\} \left(\frac{a}{r}\right)^{l+1} Y_l^m(\vartheta, \varphi) \\
&= -\nabla \sum_j \alpha_j \left\{ a \sum_{l,m}^{L} -f_l \left(\frac{a}{r_j}\right)^{l+2} \frac{\partial_\varphi}{\sin\vartheta} Y_l^m(\vartheta, \varphi) \Big|_{\vartheta=\vartheta_j, \varphi=\varphi_j} \right. \\
&\qquad\qquad\qquad \left. \times \left(\frac{a}{r}\right)^{l+1} Y_l^m(\vartheta, \varphi) \right\} \\
&= -\sum_j \alpha_j \ \nabla F_j^{L\vartheta}(\vartheta, \varphi, r)
\end{aligned}
\tag{A.6}
$$

so that we obtain

$$
F_i^{L\varphi}(\vartheta, \varphi, r) = a \sum_{l,m}^{L} f_l \left(\frac{a}{r_i}\right)^{l+2} \frac{\partial_\varphi}{\sin\vartheta} Y_l^m(\vartheta_i, \varphi_i) \left(\frac{a}{r}\right)^{l+1} Y_l^m(\vartheta, \varphi)
\tag{A.7}
$$

Integrals

For the B_r^r component, the integral from equation 3.21 can be written as

$$
\int_\Omega (\ddot{B}_r^r)^2 d\omega = \int \sum_{l,m} \sum_{l',m'} \ddot{\alpha}_i^r \ddot{\alpha}_j^r (l+1)^2 (l'+1)^2 f_l f_{l'} \left(\frac{a}{r}\frac{a}{r_i}\right)^{l+2} \left(\frac{a}{r}\frac{a}{r_j}\right)^{l'+2}
\tag{A.8}
$$

$$
\cdot \underbrace{Y_l^m(\vartheta_i, \varphi_i) Y_{l'}^{m'}(\vartheta_j, \varphi_j)}_{P_l^0(\cos\gamma)} \underbrace{Y_l^m(\vartheta, \varphi) Y_{l'}^{m'}(\vartheta, \varphi)}_{\frac{4\pi}{2l+1}\delta_{mm'}\delta_{ll'}} d\omega
\tag{A.9}
$$

$$
= \sum_{i,j} \sum_l \ddot{\alpha}_i^r \ddot{\alpha}_j^r \frac{4\pi(l+1)^4}{2l+1} f_l^2 \left(\frac{a}{r}\right)^{2l+4} \left(\frac{a}{r_i}\frac{a}{r_j}\right)^{l+2} P_l^0(\cos\gamma)
\tag{A.10}
$$

using the spherical harmonic addition theorem

$$
\sum_m Y_l^m(\vartheta_i, \varphi_i) Y_l^m(\vartheta_j, \varphi_j) = P_l(cos\gamma)
$$

where γ is the angle between (ϑ_i, φ_i) and (ϑ_j, φ_j). a is the reference radius (6371.2 km) as introduced in section 3.3.

The remaining five contributions are more complex

$$\int_\Omega (\ddot{B}_r^\vartheta)^2 d\omega = \sum_{i,j} \sum_{l,m} \left[\ddot{\alpha}_i^\vartheta \ddot{\alpha}_j^\vartheta \frac{4\pi}{2l+1}(l+1)^2 f_l^2 \left(\frac{a}{r}\right)^{2l+4} \right. \tag{A.11}$$

$$\left. \times \left(\frac{a}{r_i}\frac{a}{r_j}\right)^{l+2} \partial_\vartheta Y_l^m(\vartheta_i, \varphi_i) \partial_\vartheta Y_l^m(\vartheta_j, \varphi_j) \right] \tag{A.12}$$

$$\int_\Omega (\ddot{B}_r^\varphi)^2 d\omega = \sum_{i,j} \sum_{l,m} \left[\frac{\ddot{\alpha}_i^\vartheta \ddot{\alpha}_j^\vartheta}{\sin\vartheta_i \sin\vartheta_j} \frac{4\pi}{2l+1}(l+1)^2 f_l^2 \left(\frac{a}{r}\right)^{2l+4} \right. \tag{A.13}$$

$$\left. \times \left(\frac{a}{r_i}\frac{a}{r_j}\right)^{l+2} \partial_\varphi Y_l^m(\vartheta_i, \varphi_i) \partial_\varphi Y_l^m(\vartheta_j, \varphi_j) \right] \tag{A.14}$$

$$\int_\Omega \ddot{B}_r^r \ddot{B}_r^\vartheta d\omega = \sum_{i,j} \sum_{l,m} \left[\ddot{\alpha}_i^r \ddot{\alpha}_j^\vartheta \frac{4\pi}{2l+1}(l+1)^3 f_l^2 \left(\frac{a}{r}\right)^{2l+4} \right. \tag{A.15}$$

$$\left. \times \left(\frac{a}{r_i}\frac{a}{r_j}\right)^{l+2} Y_l^m(\vartheta_i, \varphi_i) \partial_\vartheta Y_l^m(\vartheta_j, \varphi_j) \right] \tag{A.16}$$

$$\int_\Omega \ddot{B}_r^r \ddot{B}_r^\varphi d\omega = \sum_{i,j} \sum_{l,m} \left[\frac{\ddot{\alpha}_i^r \ddot{\alpha}_j^\vartheta}{\sin\vartheta_j} \frac{4\pi}{2l+1}(l+1)^3 f_l^2 \left(\frac{a}{r}\right)^{2l+4} \right. \tag{A.17}$$

$$\left. \times \left(\frac{a}{r_i}\frac{a}{r_j}\right)^{l+2} Y_l^m(\vartheta_i, \varphi_i) \partial_\varphi Y_l^m(\vartheta_j, \varphi_j) \right] \tag{A.18}$$

$$\int_\Omega \ddot{B}_r^\vartheta \ddot{B}_r^\varphi d\omega = \sum_{i,j} \sum_{l,m} \left[\frac{\ddot{\alpha}_i^\vartheta \ddot{\alpha}_j^\varphi}{\sin\vartheta_j} \frac{4\pi}{2l+1}(l+1)^2 f_l^2 \left(\frac{a}{r}\right)^{2l+4} \right. \tag{A.19}$$

$$\left. \times \left(\frac{a}{r_i}\frac{a}{r_j}\right)^{l+2} \partial_\vartheta Y_l^m(\vartheta_i, \varphi_i) \partial_\varphi Y_l^m(\vartheta_j, \varphi_j) \right] \tag{A.20}$$

Appendix B

Locations of stations and observatories

This appendix lists the stations and observatories used for the regional and the global modelling.

station number	station code	station name	Geocentric colatitude	Coordinate longitude
1	FRN	Fresno	53.0950	240.2800
2	HRN	Hornsund	13.0850	15.5500
3	NAQ	Narsarsuaq	29.0030	314.5600
4	NGK	Niemegk	38.1210	12.6830
5	IRT	Patrony	38.0210	104.4500
6	KAK	Kakioka	53.9590	140.1870
7	SFS	San Fernando	53.5140	354.0600
8	HER	Hermanus	124.2370	19.2330
9	TRW	Trelew	133.0760	294.6180
10	GNA	Gnangara	121.6030	115.9400
11	DRV	Dumont d'Urville	156.5260	140.0160
12	MBO	MBour	75.7080	343.0330
13	GUA	Guam	76.5270	144.8700
14	PPT	Pamatai	107.4560	210.4160
15	KOU	Kourou	84.8250	307.2690
16	MAW	Mawson	157.4640	62.8800
17	AMS	Martin de Vivies	123.6180	77.5740
18	ABG	Alibag	71.4780	72.8720

Table B.1: List of the observatories used in the global study.

station number	station code	station name	Geocentric colatitude	Coordinate longitude	Geomagnetic colatitude	Coordinate longitude
1	AGU	Agulhas	124.65	20.00	124.28	84.38
2	GON	Gonubie Mouth	122.76	28.03	123.89	92.74
3	HER	Hermanus	124.25	19.23	123.74	83.73
4	BUF	Buffels Bay	124.13	18.45	123.50	83.01
5	RIB	Rietbron	122.72	23.15	122.96	87.96
6	POR	Port St. Johns	121.46	29.54	122.89	94.58
7	CRA	Cradock	121.99	25.63	122.70	90.58
8	ELL	Elliot	121.18	27.83	122.31	92.95
9	LAN	Langebaan	122.89	18.08	122.21	82.97
10	UND	Underberg	119.62	29.49	121.08	94.98
11	FON	Fontentje	120.78	23.15	121.07	88.44
12	WIL	Williston	121.18	20.94	121.06	86.18
13	VAN	Vanrhynsdorp	121.45	18.73	120.93	83.96
14	SPR	Springfontein	120.09	25.71	120.86	91.13
15	LAD	Ladybrand	119.05	27.46	120.16	93.11
16	DOU	Douglas	118.94	23.74	119.37	89.46
17	HTZ	Hertzogville	117.99	25.59	118.78	91.51
18	PIT	Piet Retief	116.86	30.82	118.63	96.96
19	HBK	Hartebeesthoek	115.73	27.71	116.96	94.12
20	SEV	Severn	116.44	22.86	116.77	89.18
21	RIF	Rietfontein	116.58	20.04	116.40	86.39
22	KMH	Keetmanshoop	116.46	18.16	115.94	84.58
23	MIC	Mica	114.02	30.84	115.84	97.61
24	POT	Potgietersrus	114.05	29.02	115.55	95.79
25	MCO	Marico	114.20	26.75	115.29	93.51
26	MAR	Mariental	114.46	17.97	113.94	84.83
27	KHU	Khutse	113.19	24.50	113.88	91.51
28	SOS	Sossusvley	114.59	15.35	113.60	82.25
29	FRA	Francistown	111.03	27.48	112.30	94.92
30	GOB	Gobabis	112.32	18.99	112.03	86.28
31	ORA	Orapa	111.14	25.31	112.02	92.75
32	GHA	Ghanzi	111.56	21.66	111.77	89.06
33	WIN	Windhoek	112.39	17.07	111.76	84.40
34	SWA	Swakopmund	112.53	14.57	111.44	81.93
35	MAU	Maun	109.85	23.42	110.41	91.15
36	KAL	Kalkfeld	110.77	16.18	110.01	83.86
37	TSU	Tsumeb	109.08	17.58	108.60	85.58
38	OKA	Okaukuejo	109.03	15.91	108.25	83.95

Table B.2: Stations of the ancient data set

station number	station code	station name	Geocentric colatitude	Coordinate longitude	Geomagnetic colatitude	Coordinate longitude
1	RUA	Ruacana	107.31	14.38	106.28	82.80
2	OKA	Okaukuejo	109.03	15.91	108.25	83.95
3	MPA	Mpacha	107.52	24.18	108.27	92.38
4	TSU	Tsumeb	109.08	17.58	108.60	85.58
5	UGA	Ugab	110.99	13.58	109.75	81.29
6	MAU	Maun	109.85	23.43	110.41	91.16
7	GHA	Ghanzi	111.56	21.66	111.77	89.06
8	WIN	Windhoek	112.43	17.10	111.80	84.42
9	ORA	Orapa	111.14	25.31	112.02	92.75
10	GOB	Gobabis	112.32	18.99	112.03	86.28
11	FRA	Francistown	111.04	27.50	112.32	94.93
12	SOS	Sossusvley	114.59	15.35	113.60	82.25
13	KHU	Khutse	113.19	24.50	113.88	91.51
14	MES	MES	112.23	30.05	113.95	97.21
15	TSH	Tshane	113.88	21.87	114.08	88.78
16	TOM	Tom Burke	112.93	28.00	114.26	95.03
17	UNI	Unions End	114.57	19.89	114.40	86.69
18	LUD	Luderitz	116.46	15.18	115.40	81.68
19	MIC	Mica	114.02	30.84	115.84	97.61
20	SEV	Severn	116.44	22.86	116.77	89.18
21	HBK	Hartebeesthoek	115.73	27.71	116.96	94.12
22	ALE	Alexanderbay	118.41	16.52	117.55	82.54
23	PIE	Pietretief	116.92	30.89	118.69	97.01
24	DOU	Douglas	118.94	23.74	119.37	89.46
25	BLO	Blouvley	119.88	19.47	119.52	85.06
26	GAR	Garies	120.43	17.99	119.79	83.49
27	WIL	Williston	121.18	20.94	121.06	86.18
28	FON	Fonteintje	120.78	23.15	121.07	88.44
29	KAR	Kareebos	122.62	20.54	122.39	85.43
30	CRA	Cradock	121.99	25.63	122.70	90.58
31	HER	Hermanus	124.25	19.23	123.74	83.73
32	GON	Gonubie Mouth	122.76	28.03	123.89	92.74
33	GEO	George	123.83	22.38	123.91	86.90
34	HUM	Humansdorp	123.86	24.78	124.38	89.25

Table B.3: Stations of the ancient data set

Nomenclature

CMB	Core Mantle Boundary
DI-Flux	Declination-Inclination Fluxgate magnetometer
EEJ	Equatorial electrojet
IAGA	International Association of Geophysics and Aeronomy
INTERMAGNET	International Real-time Magnetic Observatory Network
MagNetE	Magnetic Network in Europe
MF	Main Field
PPM	Proton Precession Magnetometer
QHM	Quartz Horizontal Magnetometer
SAA	South Atlantic Anomaly
SCHA	Spherical Cap Harmonic Analysis
SV	secular variation
VPM	Vector Proton Magnetometer

Bibliography

Acuña, M. (2002). Space-based magnetometers. *Review of scientific instruments*, 73:3717.

Alexandrescu, M. (1998). Database of geomagnetic observatory monthly means seeks contributors. *EOS Transactions*, 79:345–345.

Alexandrescu, M., Gibert, D., Hulot, G., Le Mouël, J., and Saracco, G. (1995). Worldwide wavelet analysis of geomagnetic jerks. *Journal of Geophysical Research*, 100:12557–12572.

Aschenbrenner, H. and Goubau, G. (1936). Eine Anordnung zur Registrierung rascher magnetischer Störungen. *Hochfrequenztechnik und Elektroakustik*, 47:177–181.

Auster, H. U. (2000). *Kalibrierung von Fluxgate Magnetometern mittels Relativbewegungen zwischen Sensor und Magnetfeld*. PhD thesis, Technische Universität Carolo Wilhelmina zu Braunschweig.

Auster, H. U. and Auster, V. (2003). A new method for performing an absolute measurement of the geomagnetic field. *Meas. Sci. Technol.*, 14:1013–1017.

Auster, H. U., Fornaçon, K. H., Georgescu, E., Glaßmeier, K. H., and Motschmann, U. (2002). Calibration of flux-gate magnetometers using relative motion. *Meas. Sci. Technol.*, 13(7):1124–1131.

Auster, H. U., Glassmeier, K. H., Magnes, W., Aydogar, O., Baumjohann, W., Constantinescu, D., Fischer, D., Fornacon, K. H., Georgescu, E., Harvey, P., Hillenmaier, O., Kroth, R., Ludlam, M., Narita, Y., Nakamura, R., Okrafka, K., Plaschke, F., Richter, I., Schwarzl, H., Stoll, B., Valavanoglou, A., and Wiedemann, M. (2008). The THEMIS Fluxgate Magnetometer. *ßr*, 141:235–264.

Auster, H. U., Lichopoj, A., Rustenbach, J., Bitterlich, H., Fornacon, K. H., Hillenmaier, O., R. Krause, J. Schenk, H., and Auster, V. (1995). Concept and first results of a digital fluxgate magnetometer. *Meas. Sci. Technol.*, 6:477–481.

Auster, H. U., Mandea, M., Hemshorn, A., Pulz, E., and Korte, M. (2007). Automation of absolute measurement of the geomagnetic field. *Earth, Planets, and Space*, 59:1007–1014.

97

Bartels, J. (1957). The geomagnetic measures for the time-variations of solar corpuscular radiation, described for use in correlation studies in other geophysical fields. *Ann. Intern. Geophys. Year*, 4:227–236.

Cain, J. C., Wang, Z., Kluth, C., and Schmitz, D. R. (1989). Derivation of a geomagnetic model to n = 63. *Geophysical Journal International*, 97(3):431–441.

Chambodut, A., Panet, I., Mandea, M., Diament, M., Holschneider, M., and Jamet, O. (2005). Wavelet frames: an alternative to spherical harmonic representation of potential fields. *Geophysical Journal International*, 163:875–899.

Chulliat, A. and Telali, K. (2007). World Monthly Means Database Project. In Reda, J. (editor), *XII IAGA Workshop on Geomagnetic Observatory Instruments, Data Acquisition and Processing*.

Colomb, F., Alonso, C., Hofmann, C., and Nollmann, I. (2004). SAC-C mission, an example of international cooperation. *Advances in Space Research*, 34(10):2194–2199.

Constable, S. and Constable, C. (2004). Observing geomagnetic induction in magnetic satellite measurements and associated implications for mantle conductivity. *Geochem. Geophys. Geosyst.*, 5, Q01006.

Courtillot, V. and Le Mouël, J. L. (1984). Geomagnetic secular variation impulses. *Nature*, 311(5988):709–716.

Courtillot, V. and Le Mouël, J. L. (1988). Time variations of the Earth's magnetic field - From daily to secular. *Annual Review of Earth and Planetary Sciences*, 16:389–476.

de Boor, C. (2001). *A practical guide to splines*. Applied mathematical sciences , ISSN 0066-5452. Springer, New York, NY, rev. ed., 1. hardcover printing edition.

DeSantis, A., Falcone, C., and Torta, J. (1997). SHA vs. SCHA for modelling secular variation in a small region such as Italy. *Journal of Geomagnetism and Geoelectricity*, 49:359–371.

Ducruix, J., Courtillot, V., and Le Mouël, J. L. (1980). The late 1960s secular variation impulse, the eleven year magnetic variation and the electrical conductivity of the deep mantle.

Finlay, C., Maus, S., Beggan, C., Hamoudi, M., Lowes, F., Olsen, N., and Thébault, E. (2010). Evaluation of candidate geomagnetic field models for IGRF-11. *Earth Planets Space*, 20:1–19.

Forbes, A. J. (1987). General Instrumentation. In Jacobs, J. (editor), *Geomagnetism, Volume 1*, pages 51–142. Academic Press.

Gauss, C. F. (1833). Die Intensität der erdmagnetischen Kraft zurückgeführt auf absolutes Maaß. *Annalen der Physik*, 104:591–615.

Gauss, C. F. (1839). Allgemeine Theorie des Erdmagnetismus. *Resultate aus den Beobachtungen des magnetischen Vereins 1838*, pages 208–230.

Glaßmeier, K.-H., Soffel, H., and Negendank, J. F. W. (2009). *Geomagnetic Field Variations*. Springer.

Gubbins, D. and Herrero-Bervera, E. (2007). *Encyclopedia of Geomagnetism and Paleomagnetism*.

Haines, G. V. (1985). Spherical cap harmonic analysis. *Journal of Geophysical Research*, 90:2583–2592.

Haines, G. V. (1988). Computer programs for spherical cap harmonic analysis of potential and general fields. *Comput. Geosci.*, 14(4):413–448.

Haines, G. V. (1990). Regional magnetic field modelling - A review. *Journal of Geomagnetism and Geoelectricity*, 42:1001–1018.

Hemshorn, A. (2007). GAUSS - A Geomagnetic Automated System, Automatisierung einer Absolutwertmessung des Erdmagnetfeldes. Diplomarbeit, Technische Universität Carolo Wilhelmina zu Braunschweig.

Hemshorn, A., Auster, H. U., and Fredow, M. (2009a). TECHNICAL DESIGN NOTE: DI-flux measurement of the geomagnetic field using a three-axial fluxgate sensor. *Meas. Sci. Technol.*, 20(2):027004–027007.

Hemshorn, A., Pulz, E., and Mandea, M. (2009b). GAUSS: Improvements to the Geomagnetic AUtomated SyStem. In Love, J. (editor), *Proceedings of the XIIIth IAGA Workshop on Geomagnetic Observatory Instruments, Data Acquisition, and Processing*.

Heppner, J. P. (1963). The world magnetic survey. *Space Science Reviews*, 2(3):315–354.

Holschneider, M., Chambodut, A., and Mandea, M. (2003). From global to regional analysis of the magnetic field on the sphere using wavelet frames. *Physics of the Earth and Planetary Interiors*, 135:107–124.

Jankowski, J. and Sucksdorf, C. (1996). *Guide for magnetic measurements and observatory practice*. International Association of Geomagnetism and Aeronomy, Boulder.

Korhonen, J. V., Reeves, C., Ghidella, M., Ishihara, T., Litvinova, T., Mandea, M., Maus, S., McLean, S., Milligan, P., Purucker, M., and Ravat, D. (2007). Magnetic anomaly map of the world. Map published by Commission for Geological Map of the World, supported by UNESCO. 1st Edition, GTK, Helsinki. ISBN 978-952-217-000-2.

Korte, M. (1999). *Kombination regionaler magnetischer Vermessungen Europas zwischen 1955 und 1995.* PhD thesis, Freie Universiät Berlin.

Korte, M. and Holme, R. (2003). Regularization of spherical cap harmonics. *Geophysical Journal International*, 153:253–262.

Korte, M., Mandea, M., Kotzé, P., Nahayo, E., and Pretorius, B. (2007). Improved observations at the southern African geomagnetic repeat station network. *South African Journal of Geology*, 110(2-3):175–186.

Korte, M., Mandea, M., Linthe, H. J., A.Hemshorn, Kotzé, P., and Ricaldi, E. (2009). New geomagnetic field observations in the south atlantic anomaly region. *Annals of Geophysics*, 52:65–81.

Kotzé, P. B. (2001). Spherical cap modelling of Ørsted magnetic field vectors over southern Africa. *Earth, Planets, and Space*, 53:357–361.

Kotzé, P. B. (2003). The time-varying geomagnetic field of Southern Africa. *Earth, Planets, and Space*, 55:111–116.

Kotzé, P. B., Mandea, M., and Korte, M. (2007). Modelling the southern African geomagnetic field secular variation using ground survey data for 2005. *South African Journal of Geology*, 110(2-3):187–192.

Kring Lauridsen, E. (1985). Experiences with the Declination-Inclination (DI) fluxgate magnetometer including theory of the instrument and comparison with other methods. *Danish Meteorological Institute Geophysical Papers*.

Kuvshinov, A. and Olsen, N. (2006). A global model of mantle conductivity derived from 5 years of champ, ørsted, and sac-c magnetic data. 33, L18301.

Langel, R., Ousley, G., Berbert, J., Murphy, J., and Settle, M. (1982). The MAGSAT mission. *Geophysical Research Letters*, 9:243–245.

Langel, R. A. (1967). Processing of total field magnetometer data from OGO-2 satellite. Technical report, Goddard Space Flight Center.

Langel, R. A. (1987). The Main Field. In Jacobs, J. (editor), *Geomagnetism, Volume 1*, pages 249 –512. Academic Press.

Langel, R. A. (1990). Global magnetic anomaly maps derived from POGO spacecraft data. *Physics of the Earth and Planetary Interiors*, 62:208–230.

Lesur, V. (2006). Introducing localized constraints in global geomagnetic field modelling. *Earth, Planets, and Space*, 58:477–483.

Lesur, V., Wardinski, I., Hamoudi, M., and Rother, M. (2010). The second generation of the GFZ reference internal magnetic field model: GRIMM-2. submitted to *Earth Planets and Space*.

Lesur, V., Wardinski, I., Rother, M., and Mandea, M. (2008). GRIMM - The GFZ Reference Internal Magnetic Model based on vector satellite and observatory data. *Geophysical Journal International*, 173:382–394.

Lowes, F. J. (1966). Mean-square values on sphere of spherical harmonic vector fields. *Journal of Geophysical Research*, 71:2179.

Lühr, H., Korte, M., and Mandea, M. (2009). The Recent Geomagnetic Field and its Variations. In Glaßmeier, K.-H., Soffel, H., and Negendank, J. F. W. (editors), *Geomagnetic Field Variations*, pages 25–64. Springer.

MagNetE (2003). Summary of the first workshop on european geomagnetic repeat stations. `http://www.gfz-potsdam.de/portal/gfz/Struktur/Departments/Department+2/sec23/infrastructure/repeat_stations/MagNetE`.

Mandea, M. (2002). ...how many minutes for a reliable hourly mean? In Kotzé, P. B. (editor), *Proceedings of the X IAGA Workshop, Hermanus*, pages 112–120.

Mandea, M., Korte, M., Mozzoni, D., and Kotzé, P. (2007). The magnetic field changing over the southern African continent: a unique behaviour. *South African Journal of Geology*, 110(2-3):193–202.

Mandea, M. and Langlais, B. (2002). Observatory crustal magnetic biases during MAGSAT and Ørsted satellite missions. *Geophysical Research Letters*, 29(15).

Mauersberger, P. (1956). Das Mittel der Energiedichte des geomagnetischen Hauptfeldes an der Erdoberfläche und seine säkulare Änderung. *Gerlands Beitr. Geophys.*, 65:207–215.

Maus, S., Yin, F., Lühr, H., Manoj, C., Rother, M., Rauberg, J., Michaelis, I., Stolle, C., and Müller, R. D. (2008). Resolution of direction of oceanic magnetic lineations by the sixth-generation lithospheric magnetic field model from CHAMP satellite magnetic measurements. *Geochem. Geophys. Geosyst*, 9(7).

Neubert, T., Mandea, M., Hulot, G., von Frese, R., Primdahl, F., Jørgensen, J. L., Friis-Christensen, E., Stauning, P., Olsen, N., and Risbo, T. (2001). Ørsted satellite captures high-precision geomagnetic field data. *EOS Transactions*, 82:81–81.

Nevanlinna, H., Rynö, J., Haines, G. V., and Borg, K. (1988). Spherical cap harmonic analysis applied to the Scandinavian geomagnetic field 1985.0. *Deutsche Hydrographische Zeitschrift*, 41:177–186.

Newitt, J., Barton, C., and Bitterly, J. (1996). *Guide for magnetic repeat station surveys*. International Association of Geomagnetism and Aeronomy.

Olsen, N., Lühr, H., Sabaka, T. J., Mandea, M., Rother, M., Tøffner-Clausen, L., and Choi, S. (2006). CHAOS - a model of the Earth's magnetic field derived from CHAMP, Ørsted, and SAC-C magnetic satellite data. *Geophysical Journal International*, 166:67–75.

Olsen, N. and Mandea, M. (2007). Investigation of a secular variation impulse using satellite data: The 2003 geomagnetic jerk. *Earth and Planetary Science Letters*, 255(1-2):94 – 105.

Olsen, N. and Mandea, M. (2008). Rapidly changing flows in the Earth's core. *Nature Geoscience*, 1(6):390–394.

Olsen, N., Mandea, M., Sabaka, T. J., and Tøffner-Clausen, L. (2009). CHAOS-2 - a geomagnetic field model derived from one decade of continuous satellite data. *Geophysical Journal International*, 179:1477–1487.

Overhauser, A. W. (1953). Polarization of nuclei in metals. *Physical Review*, 92(2):411.

Panet, I., Chambodut, A., Diament, M., Holschneider, M., and Jamet, O. (2006). New insights on intraplate volcanism in french polynesia from wavelet analysis of GRACE, CHAMP and sea-surface data. *Journal of Geophysical Research*, 111:875–899.

Parker, R. (1977). *Geophysical Inverse Theory*. Princeton University Press.

Primdahl, F. (1979). The fluxgate magnetometer. *J. Phys. E: Sci. Instrum.*, 12(4):241–253.

Rasson, J., van Loo, S., and Berrami, N. (2009). Automatic diflux measurements with autodif. In Love, J. (editor), *Proceedings of the XIIIth IAGA Workshop on Geomagnetic Observatory Instruments, Data Acquisition, and Processing*, pages 220–224.

Reda, J. and Neska, M. (2007). Measurement Session During XII IAGA Workshop at Belsk. In Reda, J. (editor), *XII IAGA Workshop on Geomagnetic Observatory Instruments, Data Acquisition and Processing*, volume C-99, pages 7–19. Publications of the Institute of Geophysics Polish Academy of Sciences.

Runcorn, S. (1955). The electrical conductivity of the earth's mantle. *Trans. Am. Geophys. Union*.

Sabaka, T. J., Olsen, N., and Purucker, M. E. (2004). Extending comprehensive models of the Earth's magnetic field with Ørsted and CHAMP data. *Geophysical Journal International*, 159:521–547.

Schmucker, U. (1985). Das Magnetfeld der Erde, in Landolt-Börnstein, Gruppe 5: Geophysik und Weltraumforschung, Bd. 2: Geophysik der festen Erde, des Mondes und der Planeten.

Schott, J. J. and Thébault, E. (2010). Modelling the earth's magnetic field from global to regional scales. In *Geomagnetic Observations and Models, IAGA, Special Sopron Book Series*. in press.

Serson, P. (1962). Method of making an electromagnetic measurement. Canada, Patent No. 654552.

Shure, L., Parker, R. L., and Backus, G. E. (1982). Harmonic splines for geomagnetic modelling. *Physics of the Earth and Planetary Interiors*, 28:215–229.

Shure, L., Parker, R. L., and Langel, R. A. (1985). A preliminary harmonic spline model from Magsat data. *Journal of Geophysical Research*, 90:11505.

Thébault, E. (2008). A proposal for regional modelling at the Earth's surface, R-SCHA2D. *Geophysical Journal International*, 174:118–134.

Thébault, E. and Gaya-Piqué, L. (2008). Applied comparisons between SCHA and R-SCHA regional modeling techniques. *Geochemistry, Geophysics, Geosystems*, 9:7005–7030.

Thébault, E., Schott, J. J., Mandea, M., and Hoffbeck, J. P. (2004). A new proposal for spherical cap harmonic modelling. *Journal*, 159:83–103.

Toh, H., Kanezaki, H., and Ichiki, M. (2007). A regional model of the geomagnetic field over the Pacific Ocean for epoch 2002. *Geophysical Research Letters*, 34.

Velimsky, J., Martinec, Z., and Everett, M. (2006). Electrical conductivity in the Earth's mantle inferred from CHAMP satellite measurements-I. Data processing and 1-D inversion. 166:529 – 542.

Verbanac, G., Korte, M., and Mandea, M. (2007). On long-term trends in European geomagnetic observatory biases. *Earth, Planets, and Space*, 59:685–695.

Wardinski, I. and Holme, R. (2006). A time-dependent model of the Earth's magnetic field and its secular variation for the period 1980-2000. *Journal of Geophysical Research*, 111:12101.

Wardinski, I. and Holme, R. (2010). Signal from noise in the geomagnetic field modelling: De-noising data for secular variation studies. *Geophysical Journal International*. submitted.

Whaler, K. A. (1994). Downward continuation of Magsat lithospheric anomalies to the Earth's surface. *Geophysical Journal International*, 116:267–278.

Wiese, H., Schmidt, H., and Lucke, O. (1960). *Geomagnetismus und Aeronomie, Bd.II: Geomagnetische Instrumente und Messmethoden.* Deutscher Verl. d. Wissenschaften, Berlin.

Acknowledgements

*In ordinary life we hardly realize
that we receive a great deal more than we give,
and that it is only with gratitude that life becomes rich*

Dietrich Bonhoeffer(1943)

A dissertation should show the capability to work independently. Nonetheless, this work would not have been possible without the scientific, organisational and personal support of many people.

First I am grateful to Mioara Mandea, who gave me the chance to continue in studying geomagnetic field instrumentation and modelling after my diploma thesis. She organised the PhD position at GFZ, offered me to travel to South Africa, and was full of help with any queries concerning data acquisition, processing and model interpretation. She also admitted me staying in Braunschweig for most of the time such that I could my familiar environment. In the birth city of Gauss, Karl-Heinz Glaßmeier gave me the opportunity to stay in my office and with the colleagues at the IGEP. Always full of interest and good will, he gave me scientific incitations and self confidence. Both referees of this thesis, I am lucky to call them my *Doktoreltern*.

Big parts of this work covered modelling and programming tasks. Vincent Lesur was of uncomplaining patience when I came bothering him with my little mathematical understanding and FORTRAN disability. I feel grateful to Uli Auster and Eberhard Pulz, who taught me a lot about magnetometers and used every opportunity to fortify me with tea and cake.

Barry Pretorius and Errol Julies from Hermanus Magnetic Observatory took me on field surveys where I could -unprecedented- meet vlakvarks and lions. Baie dankie for your friendship! Also at HMO, Emmanuel Nahayo and Pieter Kotzé provided me with data and were in charge of the overall organisation of the field surveys. In both working in groups in Potsdam and Braunschweig, I felt at home. In section 2.3 at GFZ, I want to thank especially Martina Krüger for administrative tasks, Monika Korte for discussions about observatory and data issues and Ingo Wardinski who provided me with his monthly mean data base. Patricia Ritter cordially shared her office with me and read a first version of this thesis, chapter by chapter. The IGEP was my home base during the last years and during all the coffee breaks, barbecues and sport activities, I felt lucky not to be alone on

my way to PhD.

At the observatory in Niemegk, I was always welcome. I would like to thank especially Hans-Joachim Linthe, Katrin Tornow and Martin Fredow.

A lot more people cheered and encouraged me. My parents and siblings continuously supported me as well as my parents in law who always opened their pension for me during my stays in Potsdam and Berlin. Patricia and Tomasz sweetened the last exhausting months with their post card subscription. But above all, I would not be what I am without Sebastian, who always kept me going.

Curriculum Vitae

Persönliche Daten:

Name:	Geese, geb. Hemshorn
Vorname:	Anne
Geburtstag:	24.05.1981
Geburtsort:	Hamm, Westfalen
Staatsangehörigkeit:	deutsch
Familienstand:	verheiratet, keine Kinder

Schulbildung:

1990 – 2000	Beisenkamp Gymnasium, Hamm
Juni 2000	deutsch-französisches Abitur

Freiwilliges soziales Jahr:

2000 – 2001	Caritas-Kontaktstelle Werl, Arbeit mit Kindern und Jugendlichen im sozialen Brennpunkt

Hochschulbildung:

2001 – 2007	Physikstudium an der Technischen Universität Braunschweig
Januar 2007	Diplom in Physik (Thema der Diplomarbeit: "GAUSS - A Geomagnetic Automated System - Automatisierung einer Absolutwertmessung des Erdmagnetfeldes")

Ausgeübte Tätigkeiten:

2003 – 2005	Tutorin der Veranstaltung Physikdidaktik
2004 – 2006	Tutorin in den Physikpraktika für Pharmazeuten und Physiker
2004 – 2006	wissenschaftliche Hilfskraft am Institut für Geophysik und extraterrestrische Physik
2007 – 2010	wissenschaftliche Mitarbeiterin am GFZ Potsdam, Sektion 2.3: Erdmagnetfeld, und am Institut für Geophysik und extraterrestrische Physik, TU Braunschweig

Veröffentlichungen:

Geese, A., Mandea, M., Lesur, V., and Hayn, M. (2010). Regional modelling of the southern african geomagnetic field using harmonic splines. *Geophysical Journal International*, 181(3):1329–1342.

Korte, M., Mandea, M., Linthe, H.-J., Hemshorn, A., Kotzé, P., Ricaldi, E. (2009): New geomagnetic field observations in the South Atlantic Anomaly region, *Annals of Geophysics*, 52, 65-81.

Hemshorn, A., Auster, H.U.,Fredow. M. (2009). TECHNICAL DESIGN NOTE: DI-Flux measurement of the geomagnetic field using a three-axial fluxgate sensor. *Measurement Science and Technology*, 20(2)

Hemshorn, A., Pulz, E., Mandea, M. (2009): GAUSS: Improvements to the Geomagnetic AUtomated SyStem, *Proceedings of the XIIIth IAGA Workshop on Geomagnetic Observatory Instruments, Data Acquisition, and Processing*, Open-File Report 2009-1226, 100-103

Hemshorn, A., Auster, U., Fredow, M. (2009): DI3: Improving DI-Flux measurements with the Three-Component Sensor, *Proceedings of the XIIIth IAGA Workshop on Geomagnetic Observatory Instruments, Data Acquisition, and Processing*, Open-File Report 2009-1226, 104-107

Auster, H. U., Mandea, M., Hemshorn, A., Pulz, E., Korte, M. (2007): Automation of absolute measurements of the geomagnetic field, *Earth Planets and Space*, 59, 9, 1007-1014.

Tagungsbeiträge:

Geese, A. , Mandea, M., Lesur, V. (2010). SAMS - the South African Magnetic model made of Splines, 28th IUGG Conference on Mathematical Geophysics - CMG 2010, June 7-11 2010, Pisa, Italy

Geese, A., Lesur, V., Wardinski, I., Mandea, M. (2010). SV estimates from monthly means visa predictions from global field models, European Geophysical Union, General Assembly, May 4-9, 2010, Vienna, Austria

Geese, A., Mandea, M., Lesur, V. (2009). Regional Modeling of the Southern African Secular Variation, 11th IAGA Scientific Assembly, August 23-30, 2009, Sopron, Hungary

Hemshorn, A., Pulz, E., Mandea, M., Korte, M., Auster, U. (2008). GAUSS - Improvements to the Geomagnetic AUtomated SyStem, XIIIth IAGA Geomagnetic Observatory Workshop, June 9-18, 2008, Boulder and Golden, CO, USA

Hemshorn, A., Auster, U., Fredow, M. (2008). DI3 - First tests of DI-Flux measurements with a three-axial fluxgate sensor, XIIIth IAGA Geomagnetic Observatory Workshop, June 9-18, 2008, Boulder and Golden, CO, USA